



# HHS Public Access

Author manuscript

*Chem Rev.* Author manuscript; available in PMC 2017 January 13.

Published in final edited form as:

*Chem Rev.* 2016 January 13; 116(1): 215–257. doi:10.1021/acs.chemrev.5b00608.

## Nano-Bioelectronics

Anqi Zhang<sup>†</sup> and Charles M. Lieber<sup>†,‡,\*</sup>

<sup>†</sup>Department of Chemistry and Chemical Biology, Harvard University, Cambridge, Massachusetts, 02138, United States

<sup>‡</sup>Harvard John A. Paulson School of Engineering and Applied Sciences, Harvard University, Cambridge, Massachusetts, 02138, United States

### Abstract

Nano-bioelectronics represents a rapidly expanding interdisciplinary field that combines nanomaterials with biology and electronics, and in so doing, offers the potentials to overcome existing challenges in bioelectronics. In particular, shrinking electronic transducer dimensions to the nanoscale and making their properties appear more biological can yield significant improvements in the sensitivity and biocompatibility, and thereby open up opportunities in fundamental biology and healthcare. This review emphasizes recent advances in nano-bioelectronics enabled with semiconductor nanostructures, including silicon nanowires (SiNWs), carbon nanotubes (CNTs), and graphene. First, the synthesis and electrical properties of these nanomaterials are discussed in the context of bioelectronics. Second, affinity-based nano-bioelectronic sensors for highly sensitive analysis of biomolecules are reviewed. In these studies, semiconductor nanostructures as transistor-based biosensors are discussed from fundamental device behavior through sensing applications and future challenges. Third, the complex interface between nanoelectronics and living biological systems, from single cells to live animals are reviewed. This discussion focuses on representative advances in electrophysiology enabled using semiconductor nanostructures and their nanoelectronic devices for cellular measurements through emerging work where arrays of nanoelectronic devices are incorporated within three-dimensional cell networks that define synthetic and natural tissues. Last, some challenges and exciting future opportunities are discussed.

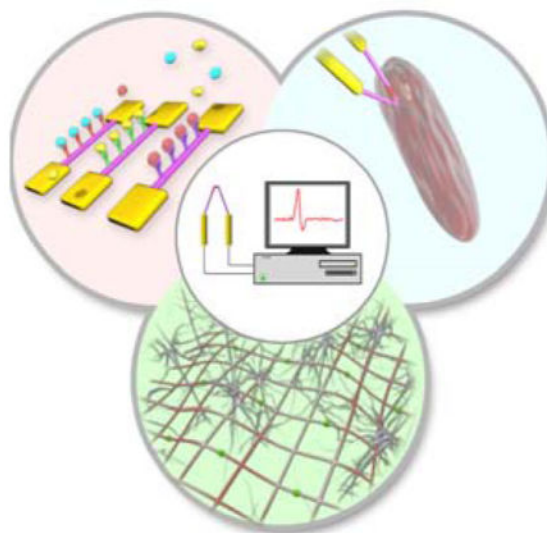
### Graphical abstract

---

\*Corresponding Author: cml@cmliris.harvard.edu.

#### Notes

The authors declare no competing financial interest.



## 1. INTRODUCTION

Bioelectronics can be broadly defined as the merger of electronics with biological systems, where a bioelectronic device transduces signals from the biological system to electrical signals at the bio-electronic interface. The development of bioelectronics has resulted in vital biomedical devices, such as blood glucose sensors,<sup>1–3</sup> cardiac pacemakers, and deep-brain stimulators.<sup>4–5</sup> Despite the success of these devices, it should be recognized that the electronic transducers have had substantial size mismatch with the biological systems to which the electronics were interfaced. Hence, substantially shrinking the electronic transducer dimensions and making their properties appear more biological could lead to significant improvements in the sensitivity and biocompatibility of next generation bioelectronics, and thereby enhance and/or open up new opportunities in fundamental biology and healthcare areas.<sup>6–7</sup>

In this regard, a variety of nanomaterials, including zero-dimensional (0D) nanoparticles, one-dimensional (1D) nanotubes and nanowires, and two-dimensional (2D) nanosheets, have emerged over the past several decades, with substantial progress made on their chemical synthesis, processing, and characterization.<sup>8–12</sup> One motivation underlying these efforts has been to elucidate how the size, structure and composition, for example, of such nanostructures lead to novel electronic, optical and magnetic properties, including quantum confinement regime in one or more dimensions. The enhanced and even unprecedented physical properties of such nanomaterials offer potentially unique opportunities in biology.

In particular, nano-bioelectronics represents a rapidly expanding interdisciplinary field that combines nanomaterials and nanoscience with biology and electronics, and in so doing, offers the potentials to overcome existing challenges in bioelectronics and open up new frontiers. For example, an affinity-based biosensor, such as a protein or DNA sensor, utilizes a surface-immobilized recognition probe to selectively interact with the biological analyte in solution and yields a electrical signal directly proportional to analyte concentration.<sup>13–16</sup> In

Author Manuscript

addition, bioelectronic devices interfaced to electrogenic cells, such as neurons or cardiomyocytes, can record and/or stimulate bioelectrical activities in the cells or corresponding tissues (e.g., brain, heart or muscle), by interconverting ionic and electronic currents at the device/cell interface.<sup>17–20</sup>

Author Manuscript

The central element in a nano-bioelectronic device is the nanostructure that is used to sensitively record or stimulate a biological event of interest. The potential of nanostructures in biology lies inherently in their small sizes and high surface-to-volume ratios. First, their high surface-to-volume ratio offers high sensitivity to surface processes. Only a small number of analyte molecules are needed to produce a measurable electrical signal, which allows both a reduction of sample volumes and the miniaturization of biosensors. In addition, the size scale of nanostructures can be comparable to biological building blocks, such as proteins and nucleic acids, offering new ways to perturb living systems from subcellular to tissue levels. The similar size scale of nanostructures and biological building blocks can also facilitate seamless integration of nanoelectronics with cells and tissues, and enables unique opportunities in synthetic tissues and biomedical prosthetics.<sup>21–24</sup>

Author Manuscript

This review is organized to emphasize recent advances in nano-bioelectronics enabled with semiconductor nanostructures, including silicon nanowires (SiNWs), carbon nanotubes (CNTs), and graphene. We will briefly discuss the relevant synthesis and electrical properties of these nanomaterials in the context of bioelectronics in Section 2. Section 3 discusses affinity-based nanobiosensors for highly sensitive analysis of biomolecules. In these studies, semiconductor nanostructures have been utilized as the central element of transistor-based biosensors. Sections 4 and 5 describe the complex interface between nanoelectronics and biological systems, from single cell to *in vivo* live animal levels. Our discussion will be focused on several representative conceptual advances in electrophysiology enabled by using semiconductor nanostructures and their nanoelectronic devices, rather than trying to comprehensively cover all the work performed in this vibrant field.

## 2. NANOSTRUCTURE BUILDING BLOCKS AND NANOTRANSISTORS

Author Manuscript

Nanostructure building blocks can be synthesized via the bottom-up paradigm, in a manner that mimics how complex biological systems are constructed by proteins and other biological building blocks in nature. Central to the bottom-up approach is the synthesis of building blocks with controlled structure, size and morphologies, as these characteristics determine their chemical and physical properties.<sup>8–10,12,25</sup> Bioelectronic devices based on these building blocks can be rationally designed to exploit the unique properties of different nanomaterials with the goal of providing unique capabilities of interfacing to and studying different biological systems. Thus, we will provide a brief introduction to the structure, preparation and electrical properties of three representative semiconductor nanomaterials being used in bioelectronic devices: silicon nanowires, carbon nanotubes and graphene. We refer the interested reader to more comprehensive reviews focused on the synthesis and properties of semiconductor nanowires,<sup>8–9,26–28</sup> nanotubes<sup>25,29–33</sup> and graphene.<sup>34–38</sup>

## 2.1. Silicon Nanowires

We will focus on SiNWs as a representative example of semiconducting NWs for bioelectronics since key nanostructure properties, including morphology, size, composition and doping, have been widely explored and can now be precisely controlled during synthesis.<sup>26–28</sup> Silicon and other NWs also can be well-aligned into highly ordered arrays,<sup>39–44</sup> which are important for the construction of arrays of bioelectronic devices and integrated circuits. Also, the diameter of NWs can be readily reduced to a few nanometers,<sup>45</sup> and the crystalline structure and smooth surface of chemically synthesized NWs reduce scattering and result in enhanced electrical properties.<sup>46</sup> Thus, semiconductor NWs represent a logical pathway to scaling of semiconductor devices for potentially novel bioelectronic devices.

**2.1.1. Basic Structures and Preparation**—The basic SiNW has a uniform composition, 1D structure with diameter typically in the range between 3–500 nm, and length ranging from several hundreds of nanometers to millimeters.<sup>47</sup> The two paradigms for realizing SiNWs can be categorized as top-down and bottom-up.<sup>26,28,48–53</sup> The top down paradigm, often based on lithography, deposition and etching steps, offers convenient processing of a uniform macroscopic section of material, such as a Si wafer, into different pre-defined structures with nanoscale dimensions. The bottom-up paradigm, on the other hand, is based on synthesizing target architectures from individual atoms and molecules, with key nanometer-scale metrics built-in through synthesis and/or subsequent assembly, thus enabling the potential to go beyond the limits of top-down technologies. The bottom-up approach can lead to entirely new device concepts and functional systems,<sup>54</sup> and thereby create technologies that people have not yet imagined. The bottom-up synthesis of SiNWs has been primarily achieved by vapor phase growth.<sup>51,55–67</sup> Among these, the nanoparticle-catalyzed vapor–liquid–solid (VLS) mechanism<sup>8</sup> is the most widely used because of its simplicity and versatility.

In 1964, Wagner<sup>68</sup> introduced the VLS growth of silicon structures, where the VLS mechanism underpins most of the bottom-up synthetic studies of SiNWs. It is important to recognize, however, that this early work yielded only microscopic Si whiskers or wires. Truly nanoscopic SiNWs were not reported until 1997<sup>69</sup> and 1998,<sup>55–56</sup> when research groups at Harvard University<sup>55,69</sup> and Hong Kong City University<sup>56</sup> reported nanoscale SiNWs. In the former work,<sup>55,69</sup> laser ablation was used to generate nanoscale catalysts and simultaneously silicon or germanium reactant and thereby yield high-quality single crystalline silicon and germanium NWs by the now general and widely used nanocluster-catalyzed VLS growth approach. In the latter study,<sup>56</sup> a distinct oxide catalyzed NW growth mechanism was proposed. These early demonstrations opened up substantial opportunities in this exciting field, and significant progress since has been achieved on length scales ranging from the atomic and up, in controlling the morphology, size, composition and doping of SiNWs.<sup>8–10,26–28</sup>

Key points in the VLS mechanism are illustrated in Figure 1, in which a nanometer scale catalyst is used to promote the material growth constrained along only one direction. In this mechanism, a metal catalyst, such as a gold (Au) nanoparticle, forms a liquid metal-

semiconductor eutectic alloy at an elevated temperature by adsorbing the vapor reactant, such as silane ( $\text{SiH}_4$ ) or silane decomposition products. Continuous incorporation of the semiconductor material in the alloy through the vapor/liquid interface ultimately results in supersaturation of the semiconductor material. It then drives the precipitation of the semiconductor material at the liquid–solid interface to achieve minimum free energy. Accordingly, the 1D crystal growth begins via the transfer of the semiconductor material from the vapor reactant at the vapor/liquid interface into the eutectic, followed by atom (e.g., Si atoms) addition at the liquid/solid interface. In addition, because the gold nanoparticle remains at the tip of the NW during VLS growth, it can define the diameter of the 1D NW as long as all reactant addition is through the liquid/solid interface.

Following the initial laser ablation studies, the nanoparticle-catalyzed VLS process was expanded to exploit more controlled reactant sources such as chemical vapor deposition (CVD).<sup>57,70</sup> In this modification, a volatile gaseous precursor, such as  $\text{SiH}_4$  or  $\text{SiCl}_4$ , was used as the silicon source for the growth of SiNWs. The gaseous precursor is transported by a carrier gas, typically Ar or  $\text{H}_2$ , to the surface of the metal catalyst, where the precursor reacts and is decomposed. Because of the excellent control over many aspects of the synthesis process, CVD-VLS growth has become arguably the most powerful option for NW synthesis.

During VLS growth, SiNWs are formed in near-equilibrium condition, and the growth processes can thus be considered primarily thermodynamically driven. As a result, the preferred growth direction is the one that minimizes the total free energy. Wu et al.<sup>45</sup> and Schmidt et al.<sup>71</sup> found that the growth directions of intrinsic SiNWs can be influenced by the diameter of the NWs. The larger intrinsic SiNWs with diameters above 20 nm exhibit a dominant  $\langle 111 \rangle$  growth direction, whereas NWs with smaller diameters (3–10 nm) tend to grow along the  $\langle 110 \rangle$  direction, and  $\langle 112 \rangle$  NWs are obtained in the transition region. These results can be understood by the increasing contribution of the silicon/vacuum surface energy to the total free energy in smaller NWs. In addition, system pressure during growth and doping level can play an important role in determining NW growth orientations,<sup>27,72–73</sup> and represents an area for further study in the future.

**2.1.2. Advanced Morphologies and Structures**—An important feature of the bottom-up growth paradigm is the capability for tunable synthesis of new materials and architectures on many length scales. In this regard, 1D semiconductor NWs represent one of the most powerful platforms for rational designed and synthetic realization of complex nanostructure building blocks or systems with predictable physical and chemical properties. In addition, assembly of distinct functional SiNW building blocks can enable exploration and applications of multi-component devices and integrated systems. To date, five general structural classes have been demonstrated: homogeneous NWs, axial modulated structures, radial/coaxial modulated structures, branched/tree-like NWs, and kinked structures (Figure 2).<sup>74–120</sup> As discussed below, several of these modulated nanowire structures, which have not been achieved in carbon-based materials, offer unique advantages for creating nano-bioelectronic interfaces.

1. Axial NW heterostructures.<sup>74–75</sup> The controlled synthesis of axial NW superlattices was reported in 2002 by three research groups, representing a significant step in the controlled synthesis of NW heterostructures.<sup>76–79</sup> As an example, Gudiksen et al. successfully synthesized GaAs/GaP, *n*-Si/*p*-Si, and *n*-InP/*p*-InP axial NW heterostructures.<sup>79</sup> The prerequisite for the synthesis of axial NW heterostructures is the continuation of the NW elongation when different vapor phase reactants are introduced, and thus the metal catalyst should be able to promote reactions with all of these reactants under similar growth conditions. This seminal work on axial-modulated NWs was subsequently expanded with the synthesis of metal-semiconductor junctions,<sup>80–81</sup> doping-modulated NWs,<sup>82–83</sup> as well as NWs with ultra-short morphology features<sup>84–85</sup>. In a recent work, the Tian group showed that pressure-dependent formation of etchant-resistant patterns within SiNWs by iterated deposition-diffusion-incorporation of gold (originated from the nanoparticle catalyst) to yield mesostructured SiNWs post-etching.<sup>86</sup>
2. Radial NW heterostructures. Radial core/shell NW structures can be achieved by the deposition of the shell on the surface of the 1D NW core. One of the first reports of core-shell NW heterostructures by Lauhon et al. used a CVD approach to grow homo- and heterostructures from Si and Ge, with different dopant concentrations, including *i*-Si/*p*-Si, Si/Ge and Ge/Si core-shell NWs.<sup>87</sup> Later, the Lieber group reported CVD growth of (InGaN/GaN)<sub>*n*</sub> quantum wells,<sup>88–89</sup> regioselective NW shell synthesis in studies of Ge and Si growth on faceted SiNW surfaces,<sup>90</sup> and facet-selective growth of CdS on SiNWs.<sup>91</sup> Recently, Plateau–Rayleigh crystal growth of periodic shells on NWs has been demonstrated with tunable morphological features, such as diameter-modulation periodicity and amplitude and cross sectional anisotropy.<sup>92</sup>
3. Branched NW heterostructures.<sup>93</sup> A third basic motif involves the synthesis of branched or tree-like NWs. The higher degree of complexity in such structures increases the potential for NW applications, by increasing the number of connection points and by providing a means for parallel connectivity and interconnection of functional elements. Several methods have been reported for the synthesis of branched structures, ranging from sequential catalyst-assisted growth,<sup>94–102</sup> solution growth on existing NWs,<sup>103–106</sup> phase transition induced branching,<sup>107–110</sup> one-step self-catalytic growth<sup>111–114</sup> and screw dislocation driven growth.<sup>115–118</sup> As an example, Jiang et al. reported the synthesis of branched NW structures, including group IV, III–V and II–VI, with metal branches selectively grown on core or core-shell NW backbones.<sup>101</sup> As the branched NWs are obtained by dispersion of catalysts on the backbone and reintroduction of the growth precursors for a second growth stage, each generation of NW branches can have a unique diameter and composition.
4. Kinked NW structures. The VLS growth mechanism can be further extended to the stereo-controlled synthesis of kinked NWs. Tian et al. showed that kinks can be created by introducing a perturbation, such as purging and reintroducing reactants, during the normal NW growth.<sup>73</sup> The kinks consist of two straight single-crystalline arms connected by one fixed 120° joint in a SiNW. In addition,

nanoscale axial *p-n* junctions can be synthetically introduced at the joints of kinked SiNWs.<sup>119</sup> The stereochemistry of adjacent kinks can be controlled,<sup>54,120</sup> which allows the synthesis of increasingly complex 2D and 3D structures with unique capabilities for bioelectronics.

The design and rational synthesis of the complex NWs described above renders them unique building blocks for controlling nano-bio interfaces. For example, kinked NW structures, which will be discussed further below, can improve cell/device junction tightness, and with phospholipid bilayer coatings, these nanoscale transistors can function as point-like, mechanically non-invasive probes capable of entering cells without the need for direct exchange of solution (as occurs with micropipettes).<sup>54</sup> In addition, recent studies of mesostructured SiNWs can enhance bio-nano interface,<sup>86</sup> and thus could contribute to nano-bioelectronic devices in the future as well.

**2.1.3. Large-Scale Assembly of Nanowires**—NWs synthesized by bottom-up approaches often have random alignment and orientations, and thus cannot be used ‘as is’ for fabrication of ordered device arrays. To fulfill the potential of NWs as building blocks for such applications requires effective assembly and integration techniques that transfer NWs from growth substrates onto the device substrates with control of alignment and position.<sup>39–44</sup> Reported methods include flow-assisted alignment,<sup>121–126</sup> Langmuir–Blodgett technique,<sup>127–135</sup> blown bubble method,<sup>136–137</sup> chemical binding/electrostatic interactions,<sup>138–143</sup> interface-induced assembly,<sup>144–145</sup> electric/magnetic field-assisted alignment,<sup>146–154</sup> PDMS transfer,<sup>155–159</sup> contact/roll printing techniques,<sup>160–166</sup> nanocombing,<sup>167</sup> as well as other assembly methods.<sup>168–172</sup>

As an early example, Huang et al. designed a flow-assisted technique by combining fluidic alignment with surface-patterning, whereby the separation and spatial location of NW arrays are readily controlled.<sup>122</sup> In this method, NWs are aligned by passing a suspension of NWs through microfluidic channel structures formed between a polydimethylsiloxane (PDMS) mold and a flat substrate, pre-functionalized to enhance the interaction with NWs (Figure 3a, b). Alternating the flow in orthogonal directions in a two-step assembly process yielded crossbar structures (Figure 3c), while equilateral triangles were assembled in a three-layer deposition sequence using 60° angles between the three flow directions (Figure 3d). In 2007, Javey et al. developed a contact printing method to directly transfer NWs from a growth substrate to a second device substrate.<sup>160</sup> As illustrated in Figure 3e, the NW growth substrate is placed upside down on top of a lithographically patterned substrate, and translated horizontally for several millimeters under normal load to transfer the as grown NWs onto the underlying substrate with an orientation parallel to the sliding direction. This NW transfer process can be repeated multiple times, along with the deposition of a thin SiO<sub>2</sub> insulating layer between adjacent NW layers to yield 3D stacked arrays (Figure 3f).

In 2013, a dry-transfer approach based on an innovative nanoscale “combing” technique was developed.<sup>167</sup> A small anchoring region is opened in the accepting substrate where the tips of the NWs attach due to strong attractive forces. This anchoring allows subsequent substrate translation to comb the NWs over the polymer-protected region of the device substrates. Significantly, large-area arrays of parallel NWs with <1 degree misalignment and

with >98.5% yield are produced. This order of magnitude improvement in alignment has enabled fabrication and demonstration of the largest integrated NW circuit by the bottom-up approach (Figure 4).

These approaches show clearly the capability of realizing post-growth bottom-up assembly of distinct NW materials into single- and multi-layer arrays of NW-based nanoelectronic devices, which are especially important for enabling multiplexed measurements at cell/tissue levels with subcellular resolution.<sup>21–24,173–174</sup> For example and as will be discussed in more detail below, arrays of NW FET devices fabricated on substrates have been used for high-resolution recording from acute brain slices,<sup>173</sup> while arrays incorporated into free-standing macroporous mesh-like structures have opened completed new areas of tissue engineering, where the nanoelectronic mesh serves as a scaffold to electronically-innervate synthetic tissue in 3D,<sup>21–22</sup> as well as novel injectable nanoelectronics capable of *in-vivo* brain mapping.<sup>23–24,174</sup>

**2.1.4. Nanowire Field-Effect Transistors**—The field-effect transistor (FET) is a fundamental building block of high-density integrated circuits. In a standard planar FET (Figure 5a), the semiconductor substrate (e.g., *p*-Si) is connected to the gate (G), the source (S) and the drain (D) electrodes. The source and drain regions, through which current is injected and collected, respectively, have an opposite doping (e.g., *n*-type) to the substrate. The gate electrode is capacitively coupled to the semiconductor channel by an insulating oxide layer. If no gate voltage ( $V_g$ ) is applied (the “Off” state), the FET is equivalent to two *p-n* junctions connected back-to-back with almost no current flows. In the “On” state, when  $V_g$  exceeds a threshold voltage, charge carriers (e.g., holes for *p*-Si and electrons for *n*-Si) are induced at the semiconductor-oxide interface, and the potential barrier of the channel drops, resulting in a significant tunneling current flow. Therefore, the conductance of the semiconductor channel between the source and drain regions can be switched from Off to On and modulated in the On-state by the potential at the gate electrode.

Similar to its planar counterpart, the basic electronic properties of a semiconductor NW can be characterized using electrical transport studies in a FET (NW-FET) configuration (Figure 5b).<sup>175</sup> For example, NWs can be deposited on the surface of a silicon wafer covered with an oxidized layer (Si/SiO<sub>2</sub>), in which the underlying conducting silicon can serve as a global back gate. The naturally grown oxide layer on SiNWs can be used as the gate oxide. Source and drain electrodes are defined by lithography followed by evaporation of metal contacts. The electrostatic potential of the NWs is tuned by  $V_g$ , which modulates the carrier concentration and conductance of the NW. Comprehensive reviews focused on NW-FETs can be consulted for further details.<sup>46,176</sup>

In the case of NWs with homogeneous structure and composition, SiNWs have been extensively studied, due to the dominance of silicon in the semiconductor industry. Nonetheless, the initial transport studies of SiNWs were far from optimal, due to the large sample-to-sample variation and low carrier mobility. Improved control during synthesis, including the NW diameter down to sub-20 nm, fine-tuned doping level and electrical properties, has contributed to important advances and NW devices approaching 1D quantum confinement that are desirable for high-performance FETs<sup>55</sup>, such as *p*- and *n*-channel Si

NW-FETs.<sup>135,177–179</sup> Still, these NW FETs are Schottky barrier devices and their performances are affected by the metal contact (S and D), unlike conventional metal-oxide-semiconductor FET (MOSFETs) with degenerately doped semiconductor source/drain contacts. Annealing is a general method to effectively form ohmic contacts and increase the on-current.

Parallel integration of *p*-SiNW devices was subsequently demonstrated by combination of Langmuir-Blodgett (LB) assembly and photolithography techniques.<sup>135</sup> From the electrical characterization of randomly chosen NW devices within large arrays (Figure 5c), both linear source-drain current ( $I_{sd}$ ) versus source-drain voltage ( $V_{sd}$ ) curves and saturation at larger negative voltages were obtained, as expected for *p*-type FETs. Furthermore, Zheng et al. demonstrated the first example of controlled growth of *n*-type SiNWs with tunable phosphorus doping, and fabrication of high-performance *n*-type NW-FETs.<sup>179</sup> The  $I_{ds}$ - $V_{ds}$  curves recorded with gate voltage ( $V_{gs}$ ) from  $-5$  to  $5$  V are linear from small values of  $V_{ds}$  and saturated at  $V_{ds} \sim 2$  V, and show increases (decreases) in conductance as  $V_{gs}$  becomes more positive (negative), as expected for an *n*-channel FET (Figure 5d). Ohmic-like contacts with lower source contact resistance ( $R_s$ ) were obtained with heavily-doped NWs, while the nonohmic contacts with higher  $R_s$  were observed for lightly-doped NWs, where the dopant concentration dependent  $R_s$  limits the measured transconductance.

Koo et al. also reported the fabrication of dual-gated Si NW-FETs, having both a top metal gate and a backside substrate gate.<sup>180</sup> A conducting channel of either accumulated holes or inversion electrons is formed by the back gate, which also controls the shape of Schottky barrier between the channel and the source/drain electrodes. The top gate then can control ambipolar conduction (either hole or electron conduction occurs depending on the gate bias) in these SiNW-FETs. Enhanced channel conductance modulation could be achieved with these dual-gated SiNW devices.

In addition to homogeneous NWs, axial heterostructures,<sup>80,181</sup> radial heterostructures<sup>182–185</sup> and crossed-NW structures<sup>157,160,186–188</sup> have also been developed to extend the versatility of NW-FETs. For example, Colinge et al. reported junctionless NW-FETs, in which the current flows through the bulk of the channel, rather than just along its surface.<sup>189</sup> Compared to classical transistors, these NW devices exhibit low leakage currents, near-ideal subthreshold slope, and less mobility degradation with gate voltage and temperature.

## 2.2. Carbon Nanotubes

CNTs have large aspect ratios, high mechanical strength, excellent chemical and thermal stability, and rich electronic and optical properties.<sup>29–30,190–192</sup> Applications of CNTs span many fields, including composite materials, nanoelectronics, and energy storage.<sup>193–198</sup> In recent years, efforts have also been devoted to exploring the potential biological applications of CNTs.<sup>199–202</sup>

**2.2.1. Structures, Preparation and Assembly**—CNTs are rolled up seamless cylinders of graphene sheets. CNTs are classed as single-walled nanotubes (SWNTs) or multiwalled nanotubes (MWNTs), depending on the number of their concentric walls.<sup>190,203</sup> The diameters of SWNTs and MWNTs are typically 0.4–2 and 2–100 nm, respectively, and

their lengths range from hundreds of nanometers to centimeters. The chirality of SWNTs, which is the angle the graphene sheets roll up with respect to lattice vectors, determines their electronic properties.<sup>190</sup> The chiral vector ( $n, m$ ) is used to quantify this rolling up angle, where  $n$  and  $m$  are the integer numbers of hexagons traversed in the two unit-vector directions of the graphene lattice. This vector can be directly related to the electronic properties of SWNTs. Specifically, a SWNT will be metallic if  $(n-m)$  is a multiple of 3 and a semiconductor otherwise. Statistically, 1/3 are metallic and 2/3 are semiconducting.<sup>204</sup> For FETs, semiconducting SWNTs are required.

A number of techniques have been used to produce CNTs,<sup>205–208</sup> including high temperature arc-discharge, laser ablation and solar beam-induced vaporization,<sup>209–215</sup> and low temperature<sup>216–224</sup> methods such as CVD. The first reported SWNTs were prepared using a carbon arc-discharge method with metal catalyst mixed in one of the carbon electrodes.<sup>210</sup> Despite its simplicity, this method is capable of producing structurally pristine SWNTs with a relatively high yield. CVD was first used to grow CNTs in 1993 by incorporating nanoparticles on substrates with hydrocarbon gas as the reactant.<sup>216</sup> Substantial efforts have been placed on CVD synthesis of CNTs, and it is now undoubtedly the preferred method for synthesizing SWNTs of highest structural quality and has been extensively reviewed.<sup>31–33</sup>

One big challenge for directly using SWNTs for FET devices is that the as-synthesized SWNTs are always a mixture of semiconducting ( $s$ -) and metallic ( $m$ -) tubes, while the latter  $m$ -SWNTs degrade performance of the devices. Methods to overcome this challenge, including growth control and post-growth separation, have been explored.<sup>225–226</sup> In growth-based separation of SWNTs, introducing a weak oxidative gas<sup>227–230</sup> or applying an external field<sup>231–232</sup> have been reported. For example, Ding et al. demonstrated the growth of SWNT arrays on quartz substrate using ethanol/methanol mixture as the carbon source, and reported > 95% of the nanotubes were semiconducting.<sup>227</sup> The authors found that this selective growth is achieved due to the presence of methanol and a strong affinity between nanotubes and the quartz substrate. In addition, a number of post-growth separation methods of  $s/m$ -SWNTs, including electrical breakdown,<sup>233–234</sup> gas etching,<sup>235–237</sup> electromagnetic radiation,<sup>238–240</sup> interaction with other molecules<sup>35,241</sup> and centrifugation<sup>242</sup> have been studied.

Ultimately, control of diameter and chirality of SWNTs is needed to *a priori* determine electronic properties as is possible with NWs. Reported strategies to control chirality have included growth rate dependence,<sup>243–244</sup> catalyst and gas interactions,<sup>245–248</sup> and cap engineering.<sup>249–253</sup> Recently, the Li group used tungsten-based bimetallic alloy nanoparticles of non-cubic symmetry as the catalysts for CNT growth with reported control of diameter and chirality.<sup>248</sup> The tungsten-based catalysts have high melting points and are able to maintain their crystal structure during the CVD process, and consequently regulate the chirality and diameter of the as grown SWNTs (Figure 6a). Specifically, they found semiconducting (12, 6) SWNTs were synthesized at an abundance of >92% (Figure 6b, c). Experimental evidence and theoretical simulations reveal that the good structural match between the carbon atom arrangement around the nanotube circumference and the arrangement of the atoms in one of the planes of the nanocrystal catalyst facilitates the ( $n$ ,

*m*) preferential growth of SWNTs. Alternatively, Sanchez-Valencia et al. used surface-catalyzed cyclodehydrogenation to convert a molecular precursor into ultrashort, singly capped (6, 6) 'armchair' nanotube seeds on a platinum (111) surface. Single-chirality and essentially defect-free SWNTs were then synthesized by elongation of these seeds, achieving lengths up to a few hundred nanometers (Figure 6d).<sup>253</sup> The ability to directly produce large amounts of nearly identical SWNTs opens new opportunities for CNTs in integrated electronics.

As 1D nanostructures, CNTs, similar to SiNWs, also need to be assembled for many applications. Two major strategies for producing CNT arrays include post-synthesis assembly<sup>254–255</sup> and the aligned growth.<sup>206,256–258</sup> Post synthesis assembly approaches, which are similar to the assembly methods for SiNWs, include flow directed alignment,<sup>259–265</sup> Langmuir–Blodgett assembly,<sup>266–267</sup> electric field<sup>268–270</sup> and magnetic field<sup>271–274</sup> directed alignment, mechanical shearing,<sup>275–280</sup> or blown bubble film techniques.<sup>136,281</sup> On the other hand, *in situ* growth approach produces aligned CNTs during growth using controlled CVD processes, including gas flow directed growth,<sup>282–290</sup> external field directed growth,<sup>232,291–292</sup> and surface-directed growth.<sup>25,293–297</sup> These *in situ* aligned growth methods have the advantage of avoiding defects induced during post-assembly, and can be combined with the standard fabrication of silicon-based devices.

**2.2.2. Carbon Nanotube Field-Effect Transistors**—Semiconducting SWNTs can be used as the channel material for FETs, as first demonstrated by the Dekker group.<sup>298</sup> Many research groups have demonstrated the potential of SWNTs as building blocks in applications such as displays, flexible electronics, and printable electronics.<sup>255,257</sup> Due to their 1D transport and long mean free path, SWNTs can enable ballistic transport in short channel devices.<sup>299</sup> It has been shown that SWNTs can have high mobility and current carrying capacity.<sup>300–301</sup> Due to oxygen doping in air, semiconducting SWNTs show *p*-type behavior. Several approaches have been reported to convert them to *n*-type, including chemical doping,<sup>302–306</sup> annealing<sup>303,307</sup> and metal contact engineering.<sup>308–310</sup> It has been found that the performance of a SWNT FET depends dramatically on the work functions of the contact metals,<sup>298–299,311–314</sup> and the interface between SWNTs and metal contacts depends sensitively on the fabrication quality during contact evaporation and annealing.

Although individual SWNTs can possess very good electronic properties, it has been difficult to integrate these building blocks into large-scale electronics, due in part to their low current output per nanotube, small active areas, and the aforementioned heterogeneous mixtures of metallic and semiconducting as-synthesized tubes. This heterogeneity in electronic properties is one major difference between SWNTs and SiNWs, where the mixture of *s*-/*m*- SWNTs will yield device-to-device performance variations.

### 2.3. Graphene

Graphene is defined as a single 2D layer of *sp*<sup>2</sup>-hybridized carbon atoms joined by covalent bonds to form a flat hexagonal lattice with excellent electrical and mechanical properties. Below we will provide a brief summary of the preparation of graphene and graphene device

properties; readers are referred to reviews of graphene synthesis and properties of graphene FETs for more detailed information.<sup>34,36–38,315–317</sup>

**2.3.1. Exfoliation of Graphite**—Graphite consists of many sheets of graphene stacked together. In a single graphene sheet, carbon atoms are linked by covalent bonds, while adjacent graphene sheets interact by much weaker van der Waals bonds. Therefore, single graphene sheets can be obtained by exfoliating graphite. Reported exfoliation methods include mechanical, liquid, and oxidation/reduction processes.

The experimental isolation of single-layer graphene was firstly demonstrated by Geim and coworkers at Manchester University<sup>318</sup> (Figure 7a). They used mechanical exfoliation technique (i.e., peeling with adhesive tape) to isolate graphene from graphite, and obtained single- and few-layer flakes pinned to the receiver substrate, by van der Waals forces. Graphene flakes prepared by mechanical exfoliation have high crystal quality and can be more than 100  $\mu\text{m}^2$  in size. The pristine graphene prepared by mechanical exfoliation exhibits remarkably high carrier mobility, room temperature Hall effect, and ambipolar field-effect characteristics.<sup>319–321</sup> The high carrier mobility and ambipolar device characteristics are valuable for bioelectronics. However, mechanical exfoliation is of low throughput and not able to produce large graphene sheets. These drawbacks have limited the use of mechanically exfoliated graphene to primarily single device studies.

Another exfoliation process is achieved in liquid assisted by ultrasonication,<sup>322–323</sup> as the solvent–graphene interaction is balanced by the inter-sheet attractive forces after exfoliation. Solvents with surface tension  $\sim 40 \text{ mJ m}^{-2}$  are most suitable for graphene dispersion because they minimize the interfacial tension.<sup>324</sup> For example, Hernandez et al. obtained graphene dispersions with concentrations up to  $\sim 0.01 \text{ mg mL}^{-1}$  in organic solvents such as N-methylpyrrolidone (NMP). In the same year, Blake et al. achieved graphite exfoliation by sonication in dimethylformamide (DMF).<sup>325</sup> Bourlinos et al. proposed perfluorinated aromatic solvents and tested their exfoliating performance.<sup>326</sup> Qian et al. produced monolayer and bilayer graphene by a solvothermal-assisted exfoliation process in acetonitrile, and the yield reached 10 to 12 wt%.<sup>327</sup> Small organic molecules and polymers can further promote the exfoliation of graphite, especially when they have a good adsorption on graphene sheets.<sup>328–337</sup> For instance, Dai and coworkers inserted tetrabutylammonium hydroxide (TBA) into oleum-intercalated graphite and sonicated it in a DMF solution of 1,2-distearoyl-sn-glycero-3-phosphoethanolamine-N-[methoxy(polyethyleneglycol)-5000] (DSPE-mPEG) to form a homogeneous suspension.<sup>333</sup> The resulted graphene sheets are made into conducting films by Langmuir–Blodgett assembly on transparent substrates. The one-, two- and three-layer films on quartz afforded transparencies of  $\sim 93$ , 88 and 83%, respectively (Figure 7b, c). The scalability of liquid-phase exfoliation can be used to deposit graphene on different substrates that are not applicable to mechanical cleavage. Nonetheless, the exfoliated ‘graphene’ obtained from sonication often has a large variety of flakes consisting of different number of layers, and the electronic properties of the graphene can also be affected by the surfactants and/or polymers used in the exfoliation processes.

A third and perhaps the oldest method involves oxidizing graphite to expand its graphitic layers, followed by exfoliation into single layers of graphene oxide (GO), and finally

reduction to remove the oxygen groups. Three approaches have been used to oxidize graphite: the Brodie,<sup>338</sup> Staudenmeier<sup>339</sup> and Hummers<sup>340</sup> methods. In 2010, Marcano et al. improved the Hummers method to obtain a larger fraction of hydrophilic oxidized graphene material.<sup>341</sup> After oxidation, the van der Waals force between the layers is weakened, and the interlayer spacing increases from 0.34 nm in graphite to above 0.6 nm. As a result, single GO flakes can be isolated by ultrasonication. Many methods have been used to remove oxygen groups from the GO structure and restore the desired  $sp^2$  hybridized structure, such as chemical,<sup>342–346</sup> thermal<sup>347–349</sup> and electrochemical<sup>350–351</sup> treatments. Nonetheless, the oxygen functional groups cannot be completely removed by these reduction procedures. Significantly, the residual oxygen functional groups and oxidation-created defects reduce or eliminate most of the unique electronic properties of pristine graphene in reduced GO materials.

**2.3.2. Synthesis of Graphene**—As an alternative to the top-down exfoliation processes is bottom-up CVD synthesis of graphene.<sup>352–354</sup> The CVD method relies on the catalytic and carbon-saturated properties of the specific metals upon exposure to a hydrocarbon gas at high temperatures. At first, graphene grown by CVD was reported using Ni and Cu substrates,<sup>355–359</sup> and subsequently this work was extended to other transition metal substrates.<sup>360–364</sup> For example, heating a Ni substrate in the presence of hydrocarbon leads to decomposition and dissolution of the carbon in Ni. Because carbon atoms have very different solubility in Ni at high and low temperatures, as the substrate is cooled down, carbon atoms diffuse to the Ni surface and form graphene films. It is important to note that graphene grown on Ni is polycrystalline and usually consists of single- and few-to-multilayer regions. On the other hand, Cu allows higher quality single-layer graphene growth. This phenomenon is due to the fact that carbon has a relatively low solubility in Cu, and only a small percentage of carbon atoms are dissolved in the substrate. Single- or double-layered graphene is realized during the cooling process. Bae et al. demonstrated that the monolayer graphene films grown by CVD on Cu substrates can be as large as 30 inches (Figure 7d).<sup>365</sup> For electronic applications of graphene, the catalytic metal substrate needs to be removed and the graphene transferred onto other substrates. One approach involves etching the metal substrate while the graphene is supported by an inert polymer such as poly(methyl methacrylate) (PMMA) or PDMS, followed by transfer of the polymer/graphene onto the desired substrate.<sup>358,366</sup> The physical properties of CVD grown graphene deviate to some extent from those of pristine graphene formed by mechanical exfoliation, due to lattice defects and impurities. Furthermore, the necessity of transferring the as-grown graphene film from the metal growth substrate to an insulating substrate for device fabrication further introduces additional defects, impurities, that can degrade the electrical and mechanical performances of the CVD graphene.

Another method to synthesize uniform, wafer-size graphene layers involves epitaxial growth on single-crystalline silicon carbide (SiC) substrates that are heated in vacuum to high temperatures. As Si sublimes faster than carbon from SiC, the excess carbon atoms remaining behind on the surface can rearrange to form graphene layers (Figure 7e).<sup>367–371</sup> Nonetheless, the high cost of single crystal SiC wafers precludes large-scale growth of

graphene using this approach. Last, coupling of polycyclic aromatic molecules on metal surface represents another route to produce nanoscale graphene (Figure 7f).<sup>372–375</sup>

**2.3.3. Graphene Field-Effect Transistors**—Theoretical predictions have long suggested extremely high carrier mobility in graphene due to the high quality of its 2D crystal lattice. In 2008, the Kim group measured a carrier mobility in excess of 200,000 cm<sup>2</sup> V<sup>-1</sup> s<sup>-1</sup> in suspended graphene with minimized substrate-induced scattering.<sup>376</sup> This high carrier mobility implies that charge transport is essentially ballistic on the micrometer scale even at room temperature. These results have generated significant interest in graphene as a possible material for the next-generation semiconductor devices.

Graphene FETs can exhibit an ambipolar field effect. Due to its ultrahigh mobility, graphene FETs respond quickly to variations of gate-source voltage. However, the absence of a bandgap yields a small On/Off ratio in graphene FETs, which has hindered applications of this material in semiconducting electronics. Several approaches have been proposed to overcome this limitation by creating a bandgap in graphene through (i) application of uniaxial strain,<sup>377–378</sup> (ii) using bilayer graphene under an external field,<sup>379–382</sup> and (iii) employing quantum-confined nanoribbons with well-defined edges.<sup>383–386</sup>

For the application of biosensing, three different structures of graphene FETs have been developed. (1) Back-gated graphene FETs, where the graphene film is transferred or deposited on a dielectric surface (typically a SiO<sub>2</sub> layer) and source/drain electrodes are fabricated on the top. (2) Top-gated graphene FETs, where the gate dielectric is prepared on the graphene surface. This configuration has more flexibility in electronic applications but also suffers from lower carrier mobility because the top gate induces scattering. (3) Dual-gated graphene FETs, where a conducting substrate acts as the back gate, a metal as the top gate, and graphene as the conducting channel between source and drain.

### 3. NANOELECTRONIC BIOSENSORS

Next-generation biomedical diagnostics demand novel biosensors and assays that can fulfill the requirements of ultrasensitivity and high-throughput. Many semiconducting nanomaterials, such as NWs, SWNTs and graphene have been studied for the electronic sensing in an effort to address these needs. Due to their unique structural and chemical characteristics, including diameters similar to biomolecules, high surface-to-volume ratios and tailorable surfaces, these nanomaterials can be fabricated as high-performance FETs suitable for label-free, real-time, sensitive detection of proteins and other biomolecules.<sup>387</sup>

The electrical detection of biomolecules using a nanomaterial-based FET (nanoFET) can be understood as follows. The surface of a nanoFET is functionalized with biomolecule receptors, such as monoclonal antibodies or single-strand DNA (ssDNA) probes, which can selectively bind to biomolecule targets in solution. The binding of charged biomolecules, (the sign and quantities of the charges depend on the isoelectric point of the biomolecules and the solution pH), leads to a variation of charge or electric potential at the nanoFET surface, in a way similar to applying an external potential to gate electrode in a conventional FET device. The charge carrier densities of the nanoFET is thus tuned and leads to an

electrical conductivity change associated with the biomolecular binding events in real time. Due to the similar diameter or thickness to most biomolecules (e.g. proteins and nucleic acids), these binding events can be sensitively detected by the nanoFETs. Furthermore, incorporation of a number of these nanoFETs in a single device array functionalized with different surface receptors can allow for multiplexed electrical detection in the same assay, enabling a unique and powerful platform for chemical/biological recognition.

In this section, we will introduce NW-, SWNT-, and graphene-based FET biosensors, with an emphasis on SiNWs, which represent the first nanoFET biosensors reported.<sup>388</sup> Representative examples in which FET sensors are applied to detect chemical and biomolecule targets, including proteins, nucleic acids, and viruses, are summarized. Furthermore, methods for improving the sensitivity of nanoFET sensors are briefly illustrated.

### 3.1. Nanowire Biosensors

SiNWs have been extensively investigated for nanoelectronic sensing with great success. In 2001, Cui et al. reported the first demonstration of SiNW-based biosensors.<sup>388</sup> Since then, SiNW FET biosensors have been explored for detection of a variety of biological species, including disease marker proteins,<sup>389–391</sup> DNA mismatch identification,<sup>392–394</sup> and single viruses.<sup>395</sup> In addition, SiNW FETs have also been used to study small molecule-protein interactions,<sup>389,391,396</sup> suggesting exciting potentials of drug screening, determination of reaction kinetics, and the inhibition of enzymatic activity. More importantly, the capability of integrating hundreds of SiNW FETs into a same device array, each electrically addressable, has been robustly demonstrated, as a milestone for the biosensing applications from laboratory to clinics.<sup>15,397–398</sup>

**3.1.1. Functional principles of FET sensors**—The use of planar FETs for ion-selective sensors was introduced several decades ago,<sup>399</sup> while their opportunities as chemical and biological sensors have further been advanced in new and significant ways using nanomaterials. The scheme of planar FET has been discussed in Section 2.1.4. Here, we use NWs as an example to show the sensing mechanism of these nanoFETs. Similar to planar FETs, the conductance of a NW FET can be controlled by variations in the charge density or electric potential at the channel region, making FETs ideal candidates for chemical and biological sensing, as the electric field resulted from the binding of a charged molecule to the NW surface is analogous to applying a voltage via a gate electrode. In a *p*-type SiNW functionalized with surface receptors that can specifically capture chemical/biomolecule targets, binding of molecules with negative charges (similar to applying a negative gate voltage) leads to accumulation of charge carriers (holes) and a corresponding increase in conductance (Figure 8). However, binding of molecules with positive charges (similar to applying a positive gate voltage) will deplete holes and subsequently reduce the conductance. Hence, NW FETs enable real-time label-free direct electrical readout of biological events, including binding/unbinding, enzymatic reactions and electron transfer, capabilities that are ideal for developing a platform to analyze biological samples.

Semiconductor NWs composed of Si or other materials (e.g., ZnO and In<sub>2</sub>O<sub>3</sub>) have been used for the development of FET biosensors.<sup>388,400–401</sup> Among them, the molecular-size diameter, high electron or hole mobility, and versatile surface functionalization of SiNWs, as well as the potential of interfacing with existing mature silicon industry processing, have endowed these NWs one of the most widely studied for biomolecular sensing.<sup>387</sup> SiNW FETs are transformed into nanosensors by surface functionalization with probe molecules that enable the specific recognition of chemical/biological molecule targets. Covalent binding to the native silicon oxide (SiO<sub>2</sub>) layer that naturally grows on SiNWs represents one of the most robust approaches for probe attachment and takes advantage of the wealth of knowledge available from studies focused on functionalization of glass (SiO<sub>2</sub>) slides.<sup>402</sup> A detailed SiNW surface functionalization protocol has been described elsewhere.<sup>403</sup> The simplest and earliest established example of this approach is hydrogen-ion concentration detection or pH sensing.<sup>388</sup> In this case, the SiO<sub>2</sub> layer at a *p*-SiNW surface is modified with 3-aminopropyltriethoxysilane (APTES), which yields amino group (–NH<sub>2</sub>) termination on the NW surface (Figure 9a). The amino groups and silanol groups (Si–OH) on the oxide layer undergo protonation and deprotonation as the hydrogen-ion concentration varies, thereby changing the surface charge and the NW conductance. The NW electrical conductance shows a stepwise, discrete and stable increase, in response to pH from 2 to 9 (Figure 9b). More recently, Noy and coworkers demonstrated SiNW FETs modified with lipid bilayers with and without ligand-gated and voltage-gated ion channels to monitor the solution pH. For lipid bilayer containing ion channels, devices responded to changes in solution pH, and when the channels were blocked the device response was strongly diminished.<sup>404</sup> Sensing studies of several distinct classes of biological targets are discussed below.

**3.1.2. Protein Detection**—The sensitive detection of proteins, especially those known as disease markers, offers substantial potential to benefit disease diagnosis and treatment. In 2001, pioneering work demonstrated real-time protein sensing with SiNW FET devices.<sup>388</sup> Specifically, SiNWs functionalized with biotin receptors were used to selectively detect streptavidin at concentrations down to 10 pM, substantially lower than other methods at the time. However, strong binding affinity between biotin and streptavidin leads to irreversible binding and precluded monitoring unbinding and sequential measurements at different streptavidin concentrations. To overcome this limitation, several reversible surface modifications have been explored, including biotin–monoclonal antibiotin binding and calmodulin (CaM)-Ca<sup>2+</sup> interaction, to investigate quantitative concentration-dependent analyses.<sup>388</sup> In a more recent study,<sup>391</sup> CaM-modified SiNWs were used to detect Ca<sup>2+</sup> and CaM-binding proteins through the association/dissociation interaction between glutathione and glutathione S-transferase. In addition, this basic approach has been used to demonstrate successful concentration-dependent detection of cardiac troponin T<sup>390</sup> (a biomarker for myocardial infarction), SARS virus nucleocapsid proteins,<sup>405</sup> and bovine serum albumin<sup>406</sup> in recent literature and thus further validate the efficacy of NW FETs as protein sensors.

In genomics and proteomics research, simultaneous detection of multiple proteins is believed to be especially important for diagnosing complex diseases such as cancers.<sup>407–408</sup> Moreover, the availability of different biomarkers matched with different stages of diseases

could allow for early detection and robust diagnosis. The work described above using SiNW FET devices,<sup>388</sup> although powerful in detecting binding/unbinding of proteins, lacked the capability of selective multiplexed sensing. To address this key issue, Zheng et al. developed integrated NW sensor arrays, in which ~100 individually addressable NW FETs were functionalized with several different receptors in 2005 (Figure 10a), and demonstrated several new sensing capabilities.<sup>389</sup> Specifically, monoclonal antibodies for the cancer marker proteins prostate specific antigen (PSA) carcinoembryonic antigen (CEA) and mucin-1 were used to functionalize SiNW FETs in the same device array (Figure 10b). Upon addition of buffer solutions containing different concentrations of these cancer biomarkers, changes in electrical conductance of the corresponding NW FETs were recorded with femtomolar sensitivity, which is several orders of magnitude better than possible with the standard enzyme-linked immunosorbent assay (ELISA).<sup>389</sup> This work also introduced the new concept of incorporating both *p*-type and *n*-type NWs into the same device array (Figure 10c). In so doing, the binding of a negatively charged biomarker such as PSA on the NW sensor surfaces led to an increase in conductance for *p*-SiNWs and a decrease for the *n*-SiNWs in the same sensor chip. These complementary, opposite electric signals can be used to distinguish false positive signals and enable real-time, highly sensitive and selective detection of multiplexed biomolecule targets. Similarly, Zhou and coworkers reported the complementary sensing of PSA using *n*-type In<sub>2</sub>O<sub>3</sub> NWs and *p*-type SWNTs.<sup>400</sup> The enhanced electrical conductance for the NW sensors and the suppressed electrical signal for the SWNT sensors upon the PSA addition are demonstrated with concentrations down to 5 ng/mL sensitivity at physiological buffer concentrations.

Later, an anisotropic wet-etch fabrication method was reported as an alternative ‘top-down’ NW device fabrication strategy for NW FET sensors.<sup>409</sup> The sensitivity of these top-down fabricated SiNW devices were shown to have sub-100 fM sensitivity for biotin-streptavidin interaction, mouse immunoglobulin G (IgG), and mouse immunoglobulin A (IgA) detection.

**3.1.3. Nucleic Acid Detection**—In addition to sensing protein binding/unbinding, real-time detection of nucleic acids (e.g., DNAs and RNAs) has been successfully carried out by Si and GaN NW FET devices.<sup>392–394,410</sup> The surface functionalization methods and detection schemes are similar to those described above for protein sensing, where nucleic acid concentration is transduced following binding to a probe by changes in device conductance. Multisegment CdTe-Au-CdTe NWs in which Au segments are modified with thiol-terminated DNA probes and binding to these probes induces a conductance change in the overall device structure.<sup>411</sup>

A major difference between nucleic acid and protein detection exists in the fact that the high density of negative charges on the nucleic acid phosphate backbones requires high ionic strength buffers to screen the repulsion and allow for binding when DNA or RNA is used as the probe molecule. However, high ionic strength solutions have short Debye screening lengths (see Section 3.1.5.3), which can make difficult or preclude detection. A solution that overcomes this high ionic strength binding/screening issue involves using neutral charge peptide nucleic acids (PNAs),<sup>412–413</sup> which exhibit excellent binding affinity with DNA at lower ionic strengths. Indeed, modification of SiNWs with PNA probe molecules was shown to exhibit time-dependent conductance changes associated with selective binding of

complimentary target DNA at concentrations as low as 10 fM. Moreover, this work showed that DNA biosensor could be used to distinguish fully complementary (wild type) versus single-base mismatched (mutant) DNA targets associated with Cystic fibrosis.<sup>392</sup> Additional studies using SiNWs functionalized with PNA probes in which the DNA target binding domain distance was changed exhibited a reduction in sensitivity with increasing distance between the hybridization site and the NW surface.<sup>414</sup> This observation is consistent with basic sensing mechanism since the ‘field effect’ is reduced for fixed charge as the separation from the SiNW surface increases.

Alternatively, electrostatic adsorption has also been utilized for surface functionalization of SiNW devices used in DNA detection.<sup>415</sup> Bunimovich et al. reported electrostatic adsorption of primary DNA probe strands onto an amine-terminated SiNW surfaces, where the ~parallel orientation of the DNA probes along the NW surface reduces Debye screening effects and can thereby yield sensitive DNA detection.<sup>415</sup>

More recently, detection of other nucleic acid targets using PNA-modified SiNWs has also been demonstrated. For instance, microRNAs (miRNAs), which are a large class of short, noncoding RNA molecules that regulate animal and plant genomes, have been proposed as biomarkers for cancer diagnosis.<sup>416</sup> PNA-functionalized SiNW devices have shown the capability to detect miRNAs down to a remarkable sensitivity of 1 fM,<sup>417</sup> ca. one order of magnitude better than reported earlier for DNA detection.<sup>414</sup> This phenomenon can be attributed to the higher thermal stability and melting temperature of PNA-RNA complex than that of PNA-DNA complex. The technique enabled identification of fully complementary versus one-base mismatched miRNA sequences, as well as detection of miRNA in total RNA extracted from HeLa cells, and thus offers substantial potential as a new diagnostic tool.

**3.1.4. Virus Detection**—Viruses are the major cause of infectious diseases, which remain as the world’s leading cause of death.<sup>418</sup> Successful treatment of viral diseases often depends upon rapid and accurate identification of viruses at ultralow concentrations. The first demonstration of nanoFET based virus sensor involved the detection of influenza A virus using SiNW devices. By recording the corresponding electrical conductance changes upon binding/unbinding of virus particles to monoclonal antibody-modified SiNWs, the selective detection of influenza A at the single particle level was demonstrated.<sup>395</sup> The binding kinetics between different virus-receptor interactions were also electrically differentiated by SiNW FETs (Figure 11). In addition, simultaneous detection of influenza A and adenovirus using independent SiNW biosensors functionalized with distinct antibodies for these two types of viruses was demonstrated,<sup>395</sup> and more recently, SiNW FET based selective detection of influenza A viruses down to 29 viral particles per micro-liter was achieved for breath condensate samples.<sup>419</sup> Both of these achievements represent important proof-of-concept steps towards powerful viral diagnostic devices.

Another example of virus detection is the diagnosis of Dengue, a commonly prevalent arthropod-borne viral infection.<sup>420</sup> In this latter work, a specific nucleic acid fragment with 69 base pairs derived from Dengue serotype 2 virus genome sequence, was selected as the target DNA and amplified by the reverse transcription polymerase chain reaction (RT-PCR).

The hybridization of the target DNA and PNA-functionalized SiNW FET sensors increases the device resistance, leading to a sensitivity limit down to 10 fM.

### 3.1.5. Methods for Enhancing the Sensitivity of Nanowire Sensors

**3.1.5.1. 3D branched nanowires for enhanced efficiency in analyte capture:** Three dimensional (3D) branched NWs,<sup>93-95,101,108,111</sup> where secondary NW branches are grown in a radial direction from a primary NW backbone, provide the capability of achieving 3D connectivity. By functionally encoding at well-defined branch junctions during synthesis, these rationally designed and synthesized branched NWs provide well-controlled variations in the composition of the NW backbone and branches, and allow for complex electronic and photonic nanodevices. For instance, Jiang et al. developed the general synthesis of branched, single-crystalline semiconductor NW heterostructures, including Si backbones with Au branches.<sup>101</sup> These Au-branched NW devices were investigated as nanoelectronic sensors for biomolecular detection. The Au branches, which can be modified in a highly-specific manner, act as the receptor-functionalized “antennas” for the biomolecule analyte, and provide the potential to achieve enhanced capturing efficiency and sensitivity through the 3D connectivity and interconnection. A sensitivity of 80 pg/mL for PSA detection was obtained from these mAb-modified *p*-Si/Au-branch NW FET sensors, with high selectivity.

**3.1.5.2. Detection in subthreshold regime:** The fundamental characteristics of NW FET devices, such as the transconductance and noise, can have substantial effect on their detection sensitivity. Conventionally, nanoFET-based sensors are operated in the ‘ON’ state (above the threshold voltage), where the transconductance depends linearly on gate-voltage or surface potential. However, in the subthreshold regime it is well-known that the device conductance depends exponentially on gate-voltage,<sup>421</sup> which could in principle lead to much higher analyte binding sensitivity. Indeed, Gao et al. have studied and compared carefully the detection sensitivity of SiNW FET sensors in the linear and subthreshold regimes (Figure 12).<sup>422</sup> In previous literature using SiNW FET sensors,<sup>388</sup> the conductance change ( $\Delta G$ ) or the resistance change ( $\Delta R$ ) of the sensor devices was used to quantify the concentration of the target molecules. However, an absolute signal change, such as  $\Delta G$ , does not reflect the intrinsic device sensitivity, especially when working in the subthreshold regime where device conductance is very small. To better compare sensing in different device regimes Gao et al. used a dimensionless parameter,  $\Delta G/G$ , to characterize and compare device sensitivities. This principle is exemplified in both pH and protein sensing experiments, where the electrolyte gating is used to tune the operational mode of NW FETs (Figure 12b), thus suggesting that significant sensitivity enhancement can be achieved by optimization of the FET operating conditions and understanding the fundamental electrical gating property of NW FETs. One caveat to the success of this work is that the device noise should be dominated by carrier-carrier scattering, such that the noise is also exponentially reduced in the subthreshold regime. If the noise is dominated by other scattering mechanisms, such as contact current injection and/or interface trapping/detrapping, then it may not be possible to exploit the exponential dependence of conductance on gate-voltage/surface potential in the subthreshold regime.

**3.1.5.3. Reducing the Debye screening effect:** Conventional FET sensors detect the concentration of the target species by their intrinsic charge. The charges of solution-based molecules, however, can be screened by dissolved counter ions in the solution. The Debye length, also known as the Debye radius, which is inversely proportional to the square root of the ionic strength of an electrolyte, represents the net or screened electrostatic effect of a charged species in ionic solution. A high ionic strength electrolyte solution leads to a short Debye length, and charges outside of the Debye length are electrically screened. For instance, the Debye length of 1× PBS, ~0.7 nm, can screen most protein antigen charges when they bind to an antibody modified FET surface. In order to reduce the charge screening effect of electrolyte solutions, the Debye length is typically increased by using dilute buffer solutions with low ion concentrations.<sup>405,423</sup>

Recently, several groups have reported approaches based on smaller receptors, such as aptamers<sup>424</sup> and antibody fragments,<sup>425</sup> to reduce the distance between the FET surface and biomolecule analyte being detected. These studies are promising, although further studies are needed to determine how general detection is under the limit of physiological conditions (Debye length <1 nm) as the sizes of the aptamer and antibody fragment receptors are similar to or greater than this critical length scale. Zhong and coworkers also reported a direct high-frequency measurement strategy for standard biological receptors, although those measurement requires significantly more complex device geometry, making difficult or precluding application to cellular and *in vivo* sensing.<sup>426</sup>

Very recently, Lieber and coworkers developed a new and general strategy to overcome this challenge for NW FET sensors that involves incorporating a biomolecule permeable polyethylene glycol (PEG) polymer layer on the FET sensor, where the polymer increases the effective screening length near the NW FET surface to allow for detection in high ionic strength solutions.<sup>427</sup> Using PSA as a model system, they showed that PEG-coated SiNW FETs can detect PSA in phosphate buffer concentrations up to 150 mM, with a detection sensitivity of ~10 nM and linear response range up to 1000 nM. In contrast, similar FETs without PEG functionalization can only detect PSA in buffer salt concentrations lower than 10 mM. This work suggests a new and general device design strategy for the FET sensor applications in physiological environments, important for *in vitro* and *in vivo* biological sensing.

**3.1.5.4. Electrokinetic enhancement:** Preconcentration by electrokinetic manipulation of particles offers advantageous alternative approach for high-sensitivity protein detection.<sup>428</sup> In a nonuniform alternating current (AC) electric field, the dielectrophoresis (DEP) force can induce polarized particles to move in a directed manner leading to the formation of concentration enhancement and depletion regions in a microfluidic flow channel. Compared to the detection limit without AC excitation, NW sensors modified with monoclonal antibodies for PSA in an appropriate AC field exhibit close to a ~10<sup>4</sup> fold increase in sensitivity; that is, the protein concentration at the sensor surface is increased by DEP. In addition, NW devices functionalized with other receptors for capturing cholera toxin subunit B were also demonstrated, suggesting the general applicability of this method for enhanced sensitivity detection.

**3.1.5.5. Frequency domain measurement:** In addition to the conventional electrical measurement in real time, fluctuations in the NW FET electric signal at equilibrium can convey additional information about the dynamics of the biomolecule-NW hybrid system through a coupling to carrier transport in the device. For example, binding and unbinding can affect the intrinsic device noise and characterized through measurements of the device noise spectra (Figure 13a).<sup>429</sup> In a recent study, the noise spectra in frequency domain was used to analyze contributions from different noise sources.<sup>429</sup> The frequency domain spectrum of a two-level fluctuator system has the form of a Lorentzian function similar to that of a  $RC$  circuit (Figure 13b, c). The  $1/f$  noise is well-known in conventional metal-oxide semiconductor FETs (MOSFETs), and arises from electron capture/emission from trap states.<sup>430–431</sup> If biomolecule binding/unbinding contributes substantially to the noise, it can lead to a Lorentzian peak in addition to the  $1/f$  spectrum background. Frequency domain noise spectra of SiNW FETs thus represents a means to study molecular binding kinetics and thermal fluctuations of the molecular layer on NW sensor surfaces.

**3.1.5.6. NW-nanopore sensors:** The integrated NW-nanopore FET sensor has the potential for single-molecule DNA sequencing at low cost and with high throughput.<sup>432</sup> The conventional nanopore DNA sequencing technique records ionic current from nanopores,<sup>433</sup> while the NW-nanopore sensors allow for direct sequencing of DNA molecules with fast translocation rates given the much higher bandwidth of the NW FET.

Studies have shown that nanopores can be introduced adjacent to SiNW FETs using the focused electron beam in a transmission electron microscopy (TEM) (Figure 14a).<sup>432</sup> A sensor device can then be configured by attaching PDMS solution reservoir chambers above and below the silicon nitride membrane on which the SiNW FET nanopore devices are fabricated. When the two chambers are filled with solutions of different ionic strength, FET signals corresponding to DNA translocation events can be recorded (Figure 14b, c). A 10–60 time higher signal is observed from the SiNW FET than that of the corresponding ionic current change. This work demonstrates a new nanopore sequencing device concept with fast sequencing and large-scale integration properties.

**3.1.5.7. Double-gate NW sensors:** In order to achieve high sensitivity of NW FET sensors, extensive efforts have been focused on advanced lithographic tools and size-reduction techniques.<sup>434–435</sup> For example, several groups have fabricated and explored double-gate NW FET biosensor, with two separated gates, G1 (primary) and G2 (secondary), straddling both sidewalls of the SiNW, to enhance device sensitivity.<sup>434–435</sup> This work has shown that by applying the same voltage to G1 and G2, the threshold voltage ( $V_T$ ) in the double gate mode is very sensitive to a small change of  $V_{G2}$  (the G2 voltage). Therefore, compared to a single-gate FET sensor, the sensing window of the double-gated FET is significantly broadened, especially in the subthreshold regime described earlier.

**3.1.5.8. Detection of biomolecules in physiological fluids:** Rapid and accurate molecular analysis in physiological fluids (i.e., blood or serum) is essential for disease diagnosis and management. NW FET sensors, although powerful in ultrasensitive, real-time, multiplexed detection of multiple biomolecular species, exhibit fundamental limitations regarding molecular sensing in complex, physiological solutions. As the discussed above in Section

3.1.5.3, the primary limitation to FETs is related to Debye screening effect<sup>436</sup> in high ionic strength blood/serum samples.

To overcome the limitation of Debye length, researchers have developed methods to detect blood/serum samples in a controlled manner. One immediate method to reduce the ion concentration is to dilute the blood sample with a buffer solution.<sup>437</sup> However, the diluting method has an impact on ligand-protein and protein-protein interactions and also reduces the analyte concentration, which would raise the requirement for the device sensitivity instead. The second approach is to desalt the serum samples before the multiplex detection of biomarkers,<sup>389</sup> although this might lead to a loss of target proteins during the desalting step. A third method involves introduction of a microfluidic purification chip (MPC) system to pre-isolate the target molecules and release them into a pure buffer suitable for sensing, followed by the analysis using SiNW FET arrays<sup>438</sup> in much the same manner as done with desalting approach.<sup>389</sup> The two-stage approach captures the targets from a complex environment such as a whole blood, and reduces sample consumption by effectively pre-concentrating the biomarkers. A fourth method adopts a steady-state measurement instead of a real-time recording.<sup>439</sup> Specifically, the resistance of the SiNW is measured in a low ionic strength buffer solution after antibody functionalization. Then, the SiNW sensor is incubated with undiluted serum and subsequently washed to remove unbound proteins, followed by the measurement of the second resistance value in the buffer solution. The concentration of the target molecules can be calculated according to the resistance change before and after antibody-antigen interaction. This method is independent of the ionic strength of the sample solution, thus circumventing the Debye screening in physiological fluids. A final reported method uses small antibody fragments, which have been proposed to allow antigen binding to the NW surface within the Debye length.<sup>425</sup> In this approach, the sizes of antibody probes are reduced through common bioengineering methods, and thus both the signal transduction efficiency and the detection capability can be improved.

The long-term stability of the SiNW nanoelectronic devices in physiological studies has also been investigated.<sup>440</sup> Coated with a thin layer of  $\text{Al}_2\text{O}_3$ , SiNW FETs yield long-term stability (>4 months) in physiological model solutions at 37°C. When coated with  $\text{HfO}_2$  as the surface protection layer, an even much longer of stability of >1 year has been demonstrated by SiNW FETs in physiological model solutions. These latter results suggest the potential of the SiNW FETs for long-term chronic *in vivo* studies in animals and biomedical implants.

### 3.2. Carbon Nanotube Biosensors

CNTs can be configured as either electrochemical or FET sensors, where the latter are similar to NW-based FET biosensors discussed above. In the former case of electrochemical sensors, the CNTs are used as electrodes where their small diameters can provide advantages versus traditional metal electrodes. For more information on CNT electrochemical sensors we refer readers to other reviews.<sup>441–445</sup> Here, we will focus on SWNT-FET biosensors<sup>446–450</sup> composed of single SWNTs or SWNT networks on  $\text{SiO}_2/\text{Si}$  substrates with S/D electrodes.

There have been a number of studies of SWNT FET biosensors, with four sensing mechanisms reported; these are (1) electrostatic gating,<sup>451–453</sup> (2) charge transfer,<sup>454</sup> (3) scattering potential,<sup>455</sup> and (4) Schottky barrier modification.<sup>456–457</sup> The electrostatic mechanism involves gating of the SWNT by the charged or polar analytes in a manner similar to the sensing mechanism described for SiNWs or FET devices in general. The second effect refers to charge transfer between the analytes and the SWNT, which directly changes carrier concentration and conductance through the transfer (versus indirectly by electrostatic gating). In the third mechanism, bound analytes act as a random scattering centers, which can reduce the carrier mobility and SWNT conductivity. In the fourth mechanism, analytes change the current by modulating the Schottky barrier height between SWNT-metal contacts. This latter mechanism requires nonOhmic contacts and also localizes sensing at the contact versus the SWNT material.

**3.2.1. Surface Chemistry and Functionalization**—Similar to SiNWs, SWNTs can be surface functionalized with different probes that are selective to molecular targets.<sup>458</sup> Noncovalent adsorption and covalent binding are two main approaches for surface modification of SWNTs. Noncovalent functionalization for SWNTs can be carried out by simple absorption of amphiphilic surfactant molecules or polymers. Since the  $sp^2$ -hybridized carbon network is not disrupted by noncovalent functionalization, the electrical properties of SWNTs are preserved.<sup>459</sup> Supramolecular binding of aromatic molecules can be achieved by  $\pi$ - $\pi$  stacking onto the SWNT polyaromatic surface. For example, absorption by  $\pi$ - $\pi$  stacking of pyrene derivatives has been widely utilized for noncovalent functionalization of SWNTs and the pyrene derivatives can be covalently conjugated with antibodies and other biomolecules.<sup>460–461</sup> In addition, ssDNA can form a stable hybrid with SWNTs, where bases in the ssDNA are believed interact with SWNTs by  $\pi$ - $\pi$  stacking.<sup>462–463</sup>

The hydrophobic nature of SWNT surfaces also represents a challenge for biosensors since this hydrophobicity can lead to non-specific adsorption of protein and DNA. Therefore, surface passivation of SWNTs is required to prevent nonspecific protein or DNA adsorption,<sup>464</sup> while at the same time maintaining probe-target affinity and selectivity.

**3.2.2. Detection of Biological Species**—In 2003, Dekker and coworkers reported the first single SWNT FET biosensor.<sup>465</sup> The SWNTs were noncovalently modified with glucose oxidase (GOx), which resulted in a conductance decrease attributed to capacitance change for the SWNT device. The conductance of the GOx-immobilized SWNTs also showed a pH dependence consistent with the GOx protein becoming more negative at higher pH values. Other researchers reported the use of SWNTs to detect biotin–streptavidin binding (Figure 15).<sup>454</sup> In this work, SWNTs were noncovalently modified with a layer of poly(ethylene imine) (PEI) and poly(ethylene glycol) (PEG), which was biotinylated and then used to detect binding of streptavidin to the biotin probes. Almost at the same time, Dai and coworkers reported studies of SWNT devices modified with monoclonal antibodies for detection of human autoantigen U1A.<sup>464</sup> Using biotin–streptavidin as a model, Hu et al. achieved protein detection using SWNT networks modified with nonpolar groups ( $\text{CH}_3$ ) and polar groups ( $\text{NH}_3^+$ ).<sup>451</sup> Later, Star and coworkers reported the use of SWNT FETs noncovalently functionalized with biotin for reversible detection of CaptAvidin, a tyrosine

modified avidin.<sup>466</sup> These devices show the capability of differentiating two different biotin-binding molecules, streptavidin and NeutrAvidin, via the pH-dependent sensor response.

Aside from protein detection, SWNT-FETs have also been applied for the detection of DNA hybridization. In 2006, Star et al. reported that SWNT networks modified with synthetic probe oligonucleotides can specifically recognize target DNA sequences,<sup>467</sup> with a detection range from picomolar to micromolar concentrations. Later, Gui et al. reported that SWNT FETs immobilized with ssDNA can differentiate complementary and single-base mismatched DNA strands.<sup>457</sup> The sensing response is attributed to a combination of charge transfer and Schottky barrier modification, with Schottky barrier modification being the dominant mechanism. To ensure specific adsorption of DNA to SWNTs, Martinez et al. used the polymer poly (methylmethacrylate<sub>0.6</sub>-co-poly(ethyleneglycol)methacrylate<sub>0.15</sub>-co-N-succinimidyl methacrylate<sub>0.25</sub>) to modify SWNT surface via noncovalent bonding, with ssDNA bonded covalently to the polymer.<sup>468</sup> In 2011, the Shepard group covalently attached ssDNA to a point defect on a SWNT FET to study the kinetics and thermodynamics of DNA hybridization.<sup>469</sup> Without the target DNA, a  $1/f$  conductance noise is observed from the FET device. In a solution containing the target DNA, large-amplitude two-level fluctuations appear, with the signal-to-noise ratio better than 3 over the  $1/f$  noise background.

Furthermore, SWNT-FETs have been used to detect small biomolecules<sup>470–473</sup> and dynamics in living cells.<sup>474–477</sup> For example, Chen and coworkers showed that glycosylated SWNT-FETs can directly interface with PC12 cells by supporting cell adhesion and growth, and dynamic secretion of catecholamine resulted in current responses of the SWNT-FETs.

### 3.3. Graphene Biosensors

Graphene FET based biosensors, which are similar to SWNT sensors and SiNW FET sensors described above, have also been extensively studied.<sup>38,478–479</sup> An advantage of graphene FETs in biosensing is that graphene has large surface-to-volume ratio in a single device, although multi-SWNT and multi-NW devices will have similar characteristics..

**3.3.1. Surface Chemistry and Functionalization**—Similar to other nanoFETs sensors, it is necessary to functionalize graphene surface with recognition sites. The functionalization strategies developed for SWNTs have been directly applied to graphene. Similar to SWNTs, direct covalent modification strategies are not favorable for graphene functionalization since they alter the native lattice structure of graphene by converting the carbon bonding from  $sp^2$  to  $sp^3$ , which decreases carrier mobility of graphene.<sup>480</sup> Noncovalent modification based on  $\pi$ - $\pi$  stacking and hydrophobic interactions have been successful and do not degrade substantially device performance<sup>478</sup> as shown previously for related SWNT sensors.

**3.3.2. Detection of Biological Species**—The first graphene-based DNA biosensor were demonstrated by Mohanty et al. in 2008 using GO devices.<sup>481</sup> In this work, GO devices were covalently functionalized with ssDNA probes, and when exposed to the target DNA, the hybridization process was detected through a change in conductivity. Later, Dong et al. reported detection of DNA hybridization with high specificity using CVD-grown multilayer graphene, achieving a sensitivity of 0.01 nM and the capability of identifying single base

mismatches.<sup>482</sup> They suggested that the signal is generated by DNA induced *n*-doping in graphene, instead of a field-effect. In addition, the authors showed that decoration of Au nanoparticles (AuNPs) increases the detection range. One AuNP can be covalently associated with multiple thiolated probe ssDNAs to increase the loading efficiency and capacity. Chen et al. used single-layer graphene FETs to achieve the DNA detection sensitivity down to 1 pM, more sensitive than the multi-layer graphene.<sup>483</sup> To investigate the sensing mechanism of graphene FET DNA sensors, Lin et al. measured the Hall effect, and found that the hole carrier concentration of the graphene FETs increased with complementary and single-base mismatched DNA binding, although the increase was less for mismatched case.<sup>484</sup> Recently, ultrasensitive DNA detection using reduced GO (rGO) was reported.<sup>485</sup> In this report, rGO devices modified with PNA probes exhibited a detection limit as low as 100 fM. This sensitivity is 1 order of magnitude lower than that of the previously reported graphene FET DNA biosensor based on DNA-DNA hybridization. Moreover, the rGO FET biosensor is able to distinguish complementary DNA from one-base mismatched DNA and noncomplementary DNA, in a manner shown much earlier with PNA-probe modified SiNW FET sensors.<sup>392</sup>

Graphene biosensors have also been employed for the detection of proteins. In 2009, Ohno et al. reported bovine serum albumin (BSA) detection using electrolyte-gated graphene FETs.<sup>486</sup> As shown in Figure 16a, the device conductance increases when negatively-charged BSA is bound to the graphene. In another work, the same group demonstrated an aptamer-modified graphene FETs for the detection of immunoglobulin E (IgE).<sup>487</sup> Chen and coworkers reported a graphene–AuNP hybrid sensor for protein detection.<sup>488</sup> Specifically, rGO sheets were modified with AuNPs and conjugated with anti-IgG antibodies (Figure 16b). In this case, the detection limit reaches ~13 pM, among the best of the reported carbon-based protein sensors by that time. In 2011, all-rGO device was fabricated on a transparent and flexible substrate,<sup>489</sup> and shown to detect fibronectin at concentrations as low as 0.5 nM (Figure 16c).

Graphene biosensors have been developed to detect other biologically-relevant species. Chen and coworkers used a graphene sensor to detect glucose and glutamate, with a limit of detection (LOD) of 0.1 mM and 5  $\mu$ M, respectively.<sup>490</sup> The detection is mediated by surface functionalized glucose oxidase and glutamate dehydrogenase. The catalytic reactions by both enzymes produce H<sub>2</sub>O<sub>2</sub> molecules. As a strong electron withdrawing molecule, H<sub>2</sub>O<sub>2</sub> acts as a *p*-dopant and increases the conductance of the *p*-type graphene biosensor. It was also shown that graphene outperforms thin-film network devices made of SWNTs. In 2010, He et al. demonstrated that rGO devices can be applied for the detection of dynamic secretion from living cells.<sup>491</sup> The vesicular release of catecholamines from cultured PC12 cells results in an increase in rGO conductivity. In addition, graphene FETs are also effective in detecting bacteria,<sup>481,492</sup> viruses,<sup>493</sup> and cells.<sup>494</sup>

### 3.4. Prospects for Nanoelectronic Biosensors

More than one decade has passed since the first work reporting nanoFET based biosensors.<sup>388</sup> Remarkable progress has been achieved since this time using all basic classes of nanomaterials, as long as they have met the basic concept of a FET or FET-like device

originally described for these SiNW devices. The now broad range of examples described here show clearly both the robustness of the original concept and the potential of these materials to significantly impact disease diagnosis, genetic screening, and drug discovery, as well as offering powerful new tools for research in many areas of disease diagnosis and life sciences.

Nonetheless, there are several areas of scientific study, which if addressed, could further push the limits of this technology for applications. First, one fundamental challenge to the ultrasensitive detection is to obtain well-defined receptor structures on nanodevice surfaces. In part, this reflects difficulties in characterizing receptor-device structure at the single nanodevice level and correlating such results with sensing results. One approach that could address this structural issue at the single device level would be by exploiting the substantial advances in cryo-EM,<sup>495–496</sup> which could yield high-resolution structural information of the organic/biologic/nanodevice interface. A second direction that could improve this critical device-receptor interface would be through exploration of highly-selective, self-limiting covalent chemistry that precisely defines distance and orientation of the receptors. Second, the real-time and multiplexed detection capabilities of nanoelectronic FET sensors for direct analyses of whole blood/serum detection could yield important advances in clinical monitoring and diagnostics. As discussed in sections 3.1.5.3 and 3.1.5.8, the most critical issue has been overcoming Debye screening in physiological solutions. The new strategy of modifying FET nanodevices with a permeable polymer layer to increase the effective screening length<sup>427</sup> is one promising strategy for achieving real-time detection, although further fundamental studies will be necessary to develop this and/or other approaches to the level of a technology. Third, almost all the nanoFET-based sensors are exclusively surface-bound devices. For many applications, one of the most impactful directions could be the transformation from on-chip signaling to the *in vivo* monitoring as an implant. Recent advances in the development of NW FET arrays embedded in engineered tissue patches,<sup>21</sup> which could be implanted, and incorporation of sensors in injectable electronics,<sup>23</sup> which is directly implanted in specific tissue, could enable the goal of direct *in vivo* monitoring.

#### 4. NANOELECTRONICS-CELL INTERFACES & ELECTROPHYSIOLOGICAL RECORDING

Electrophysiology is an important approach to investigate and understand bioelectrical activities in the body, including but not limited to, the brain, heart, and muscles.<sup>497</sup> For instance, neurons are the elementary processing units in the brain, and are organized and interconnected into complex networks. Information in neural networks is processed by the opening and closing of ion channels on the membrane, producing action potentials (APs) that propagate. Electrophysiological recording and decoding of the functional connectivity in brain is central to basic neuroscience research.

In addition, a variety of imaging techniques have been developed for the purpose of brain mapping, such as magnetic resonance imaging (MRI) and positron emission tomography (PET).<sup>498–500</sup> Although these noninvasive methods offer coarse views, they cannot be used to analyze neuron networks. To this end, many optical methods have emerged for both

recording and stimulating signal propagation in neural circuits.<sup>501–506</sup> However, optical approaches also have limitations, including difficulty of accessing deep brain activity and of obtaining simultaneously high spatial and temporal resolution. Nano-bioelectronics has the potential to allow multiplexed, long-term, and deep-brain detection of neural activity with a high spatiotemporal resolution. More generally, nanotechnology offers a number of opportunities for brain science.<sup>507–511</sup>

#### 4.1. Traditional Extracellular Electrophysiological Recording

**4.1.1. Principles of Extracellular Recording**—An active cellular process in electrogenic cells is accompanied by ionic current flows across the cell membrane, which change both the intracellular and extracellular potentials. A microelectrode positioned near to the outer membrane can in principle detect an extracellular potential change, and is termed extracellular recording. Two common recording paradigms are based on passive metallic microelectrodes and active transistor electrodes. In the former case, the extracellular potential induces an interfacial electric current owing to the electrochemical impedance, while for the latter, the extracellular potential acts as a gate modulating the transistor conductance. In both cases, the output signal is closely related to the interface between cell and device.

**4.1.2. Passive Metallic Microelectrodes and Their Scaling Limits**—In 1972, Thomas et al. described a planar multielectrode array for use in recording from cultured cells.<sup>512</sup> This technique is now referred to as a microelectrode arrays (MEAs) and has been widely applied to record neural activity.<sup>513</sup> In an MEA, each electrode is connected to a recording amplifier for signal processing and has the potential for recording from a single-unit spike activity at the same time. This capability makes MEAs a useful tool for the investigation of fast network dynamics both *in vitro*<sup>514–516</sup> and *in vivo*.<sup>517–518</sup> In addition to recording signals from cells, MEAs are also capable of stimulating them.<sup>519</sup> A limiting feature of conventional MEAs is the relatively large electrode sizes, 10 to 30  $\mu\text{m}$  diameters, similar to or larger than the size of neuron soma. Reduction of the size of metal electrodes could increase their spatial resolution, but also leads to an increase in impedance that results in larger thermal noise and smaller recording amplitudes.<sup>520–521</sup> To overcome this impedance limitation, surface modification methods increasing electrode surface area have been employed.<sup>522–525</sup>

**4.1.3. Active Transistor Electrodes**—In 1991, Fromherz and coworkers reported coupling and extracellular recording from neuron cells using planar Si FETs,<sup>526</sup> including mammalian cells.<sup>527</sup> As an alternative to metallic microelectrodes, electrolyte-oxide-silicon field-effect transistors (EOS-FETs) and their arrays can be fabricated by standard industrial CMOS technology, and have been actively investigated for a further improvement of signal detection capabilities in electrophysiological recording.

**4.1.4. Extracellular Electrode-Cell Interfaces**—The electrode-cell interface for passive and active electrodes plays a central role in extracellular recording since it affects the signal amplitude and shape as well as noise levels. A general goal for improving the electrode-cell interface involves decreasing the their separation in order to increase the

electrode-cell seal resistance.<sup>520</sup> When neurons are cultured on a recording device, a gap or cleft exists between the electrode and cell membrane,<sup>528–530</sup> where this cleft determines the seal resistance. Methods to promote cell adhesion and reduce the cleft/increase seal resistance include surface modification, substrate modulation and electrode shape control. For example, self-assembled monolayer modified MEAs have been reported to significantly improve device performance.<sup>531–533</sup> Surface patterned MEAs have also been employed to immobilize cultured neurons to enhance coupling.<sup>534–535</sup> In addition, studies of electrodes with 3D tips have been shown to promote cell membrane wrapping around the tips, thus resulting in improved seal resistances compared to flat and recessed electrodes.<sup>529,536</sup>

## 4.2. Nanowire Transistors for Extracellular Recording

**4.2.1. Extracellular Recording from Cultured Neurons**—The Lieber group first applied SiNW FETs for extracellular recording from cultured mammalian neurons in 2006.<sup>537</sup> They adopted a “bottom-up” paradigm to fabricate the SiNW FETs and passivated the arrays for cell-culture. For example, they showed that polylysine patterning could promote the patterned growth of neuronal projections (axons and dendrites) over arrays of four SiNW FETs (Figure 17a). At each point where the axon or dendrite crosses a NW device, a highly localized 0.01 to 0.02  $\mu\text{m}^2$  synapse-like junction is formed, which allows for multisite recording with multiple SiNW FET devices from single neurons in contrast to the typical one neuron per electrode achieved with MEA and planar FETs.

This general approach was used to investigate action potential spike propagation in several multiplexed SiNW-FET/neuron configurations. For example, in the above configuration one SiNW was used as a local input to elicit action potential spikes that were recorded from two other SiNW devices with dendrite junctions while the fourth SiNW, which is not interfaced with either an axon or dendrite, served as a control and showed no action potential signal (Figure 17b). In addition, SiNW/neuron configurations were designed to investigate the spike propagation in axons and dendrites. As shown in Figure 17c, multiple SiNWs forming junctions with a single dendrite and axon revealed signal propagation rates of 0.16 m/s for the dendrite and 0.43 m/s for the axon. The potential to extend this approach to highly integrated systems was also shown with a configuration containing 50 independently addressable NW-axon elements for a single neuron (Figure 17d). Overall, these results showed early on the potential for SiNW FET sensors to enable multiplexed recording with subcellular spatial resolution from neurons.

**4.2.2. Extracellular Recording from Cultured Cardiac Cells**—Cardiomyocytes represent another electrogenic cell type that have been extensively studied with bioelectronic devices. The groups of Chen<sup>538</sup> and Lieber<sup>539</sup> carried out extracellular recording for cardiac cells using SiNWs synthesized by top-down and bottom-up approaches, respectively. An advantage of top-down fabricated NWs is the capability to define (during fabrication) their length such that measurements across an entire cell membrane or simultaneous measurement from multiple cells can be made (Figure 18a–c). After culturing cardiomyocytes on NW chips for 1–2 days, rhythmic transient changes were observed in the device conductance, involving an upstroke current spike followed by a down-stroke one. The authors attributed the paired spikes to the onset and end of an AP, although this contrasts most other work in

the literature.<sup>54,173,539–540</sup> Specifically, typical extracellular recordings show only one peak associated with the rapid potential change due to sodium-ion channel opening.

Multiplexed measurements made with ‘bottom-up’ SiNW FET device arrays interfaced with cultured embryonic chicken cardiomyocytes show single biphasic peaks associated with each action potential of the beating cells (Figure 18d–f). To investigate the signal propagation within cardiomyocyte monolayers, an average spacing between adjacent SiNW FETs in the array is set around 300  $\mu\text{m}$ . Multiple SiNW FETs in contact with cardiomyocytes are simultaneously recorded, which show stable field potential spikes with high signal-to-noise ratio ( $>10$ ). The large signal magnitude indicates a good junction, and therefore a large seal resistance, exists between SiNW FETs and cardiomyocytes. Later, the same group<sup>84</sup> synthesized SiNW encoded active FET channel lengths of 50, 80, and 150 nm (Figure 18g). These devices were interfaced to cardiomyocytes and the conductance-time response of action potentials was recorded. Significantly, while the peak-to-peak voltage and signal-to-noise ratio showed little variation versus channel length, the deduced peak-to-peak extracellular action potential width of  $\sim 500 \mu\text{s}$  was found to be comparable to the reported time constant for individual sodium ion channels. In longer or large devices, the extracellular action potential widths are typically  $\sim 1 \text{ ms}$ , presumably due to averaging over a number of channels. These results thus suggest the possibility to monitor ion channel activity using short-channel NW FET devices. In addition, Eschermann et al. evaluated the signal shape recorded from spontaneous activity of cardiac muscle HL-1 cells with SiNW transistors fabricated by top-down process.<sup>540</sup> It is worth mentioning that they also used diamond transistor array for recording HL-1 and HEK293 cells transfected with potassium channels.<sup>541</sup>

**4.2.3. Extracellular Recording from Other Electrogenic Cells—SiNW-FET devices** have also been used to investigate electrophysiological properties of other types of electrogenic cells. For example, Chen and coworkers investigated the electrical activities of rat aortic smooth muscle cells (A7r5) as shown in Figure 19,<sup>538</sup> where each NW was in contact with multiple cells. A series of current spikes was recorded by the NW upon introduction of a solution containing a high concentration of potassium ions with each spike having a biphasic signal with durations of  $\sim 1 \text{ ms}$  similar to recording from cardiomyocytes<sup>539–540</sup> but nearly two orders of magnitude shorter than that of typical intracellular action potential of A7r5 cells.<sup>542–543</sup> As discussed above this is consistent with the NWs recording the initial rapid inward sodium current, which contributes to the initial depolarization of the action potential recorded with the patch-clamp, but not subsequent repolarizing steps.

### 4.3. Graphene Transistors for Extracellular Recording

In comparison with 1D SiNW devices, graphene has a 2D flat structure similar to conventional Si FETs and planar microelectrodes used for cell electrophysiology. In 2010, mechanically-exfoliated graphene FETs were interfaced to cultured cardiomyocytes and showed well-defined extracellular signals with signal-to-noise ratios  $>4$  (Figure 20a–c).<sup>544</sup> An advantage of graphene FET devices is that the unique particle-hole symmetry of graphene enables both *n*- and *p*-type recording with the same device simply tuning the gate

potential. This characteristic allows the origin of recorded spikes to be quickly confirmed (if real versus artifact) by the spike phase flip across the Dirac point as shown in Figure 20b. Quantitative measurements (Figure 20c) showed a constant calibrated extracellular voltage, ~3.6 mV, at different water gate potentials, indicating a robust graphene/cell interface. Comparison of the performances of graphene and NW FETs shows that graphene FET yields averaged action potential signals, while NW FET yield higher resolution signals consistent with their smaller device size.

In addition, Garrido and coworkers explored recording from HL-1 cells using the CVD-grown *p*-type graphene devices (Figure 20 d–f).<sup>545</sup> In contrast to the uniform biphasic signals recorded by exfoliated graphene devices,<sup>544</sup> this work showed a variety of peak shape, which can be attributed to variations in the cell/graphene device junctions (Figure 20 e, f). The multiplexed data (Figure 20f) also yielded signal propagation speeds of 12 to 28  $\mu\text{m}/\text{ms}$ , although the peak shape variation complicates this analysis. More recently, Fang and coworkers demonstrated that suspended graphene FET devices can yield an optimal configuration for cardiac extracellular recordings in terms of sensitivity and cell-device coupling. Moreover, their work showed that the fluctuations of water ultimately set the fundamental sensitivity limit of graphene-based bioelectronics.<sup>546</sup>

#### 4.4. Intracellular & Intracellular-Like Electrophysiological Recording

**4.4.1. Strengths and Constraints of Intracellular Measurements**—In general, noninvasive extracellular recording has the advantages for long-term multiplexed measurements. However, extracellular recording sacrifices the one-to-one correspondence between cells and electrodes, and also suffers from other fundamental limitations such as reduced signal strength and quality, and difficulty in recording sub-threshold events.<sup>547</sup> Intracellular recording can overcome all of these limitations, although not without other challenges. For example, the patch clamp methodology,<sup>548–549</sup> which is the most widely used intracellular recording technique, requires the formation of direct ionic and/or electrical junctions between the probe tip and the cytosol, which has several limitations. First, the probe tip size needs to be within ~0.2 to 5  $\mu\text{m}$ : small enough to ensure penetrating the cell membrane without major damage, but also large enough to produce a low junction impedance for recognizing small cellular signals. Second, irreversible changes occur to the cell when it is directly exposed to external probe surfaces and electrolytes, thus limiting the capability for long-term recording. Third, the relatively large size of the pipettes and associated 3D manipulators limit potential integration for multiplexed measurements. With these limitations in mind, it is possible to define the characteristics of an ideal electronic device for intracellular recording; this device should possess (i) a small size to minimize invasiveness and potentially allow for direct contact with subcellular structures, (ii) high sensitivity and signal fidelity as size is decreased, and (iii) the capability to achieve multiplexed recording at both single cell and cell network levels. Over the past several years, solid-state nanoFET based devices have demonstrated capabilities that may allow for accurate, fast, and multiplexed intracellular recording.<sup>17,19,550</sup>

**4.4.2. Intracellular-Like Recording with Protruding Metal Electrodes**—The existence of an extracellular cleft between the living cell membranes and the planar substrate

used to support recording devices can reduce electrical coupling and corresponding signal levels. As discussed above in Section 4.1.4, a number of approaches have focused on decreasing the cleft size and consequently increasing the seal resistance as a means to enhance signals. Spira and coworkers significantly increased the seal resistance by functionalizing micrometre-size mushroom-shaped gold protrusions, thereby forming tight coupling with the cell membrane.<sup>536,551–553</sup> This approach was further confirmed by Offenhäusser and coworkers.<sup>554</sup> Systematic investigations of the cleft width between the plasma membrane and protruding gold electrode surfaces reveal that these structures significantly enhance the contact, in particular at the protruding head region. As an example, studies of an *Aplysia* neuron cultured on a chemically functionalized gold-spine electrode (FGSE) and simultaneously interrogated with a patch-clamp microelectrode (Figure 21) showed several key points. First, injection of a hyperpolarizing current with the patch-clamp electrode yielded a 10 and 5 mV recorded polarizations using the patch-clamp and FGSE (Figure 21c). In addition, injection of depolarizing currents led to the observation of intracellular action potentials that were temporally correlated between the patch-clamp and FGSE (Figure 21d–f), although the amplitudes were approximately 2-fold smaller for the FGSE (25 mV) versus the patch clamp (50 mV). These observations demonstrate that functionalized FGSEs can record intracellular-like responses from electrogenic cells and thus provide significant information beyond that obtained from conventional planar metallic microelectrodes and MEAs.

**4.4.3. Intracellular 3D Nanowire Transistors**—The nanoscale dimensions of SiNW FETs make them potentially ideal as intracellular probes because (i) their small size should allow for minimally-invasive insertion and (ii) the FET device holds the promise for the true intracellular recording since it is nearly independent of interfacial impedance in contrast to passive electrode techniques. Nevertheless, the overall size of all conventional nanoFETs, which have a linear device geometry, is much larger than active FET component due to the source and drain electrical contacts. The necessity of having two contacts makes minimally-invasive insertion of a nanoFET into cells difficult if not impossible.

A break-through that first overcame this geometry-size constraint was achieved with synthesis on nonlinear kinked NWs.<sup>73</sup> The kinked structure allows for localization of a point like FET detector at the kinked NW tip, metal contacts geometrically-removed from this probe tip (Figure 22a) thereby allowing for the realization of bioprobes capable of facile intracellular recordings.<sup>54</sup> An interesting feature of these nanoFET probes was modification with phospholipid bilayers to promote spontaneous cellular internalization without external forces. Indeed, contact of cultured cardiomyocyte cells to a 3D kinked SiNW bioprobe showed three distinguishable recording stages during internalization (Figure 22b). Initially, only an extracellular action potential was observed, and then after ca. 40 s, the extracellular signal gradually disappeared with concomitant increase in a new signal consistent with the intracellular action potential. Finally, at steady state an intracellular action potential with average peak amplitude of ~80 mV and duration of ~200 ms was recorded, which is consistent with true intracellular recording.

Following this pioneering work, 3D FET-based NW-nanotube and kinked *p-n* junctions nano-bioprobes were also investigated for intracellular recordings.<sup>120,555–559</sup> For example,

recording using branched nanotube-NWs was reported in 2012.<sup>556</sup> In this work, a branched SiO<sub>2</sub> nanotube was synthetically integrated on a SiNW transistor (Figure 22c), modified with a phospholipid bilayer, which allowed penetration through cardiomyocyte cell membranes, followed by intracellular action potential recording by the SiNW FET. The intracellular potential functions as an electrolyte gate through the nanotube, thereby modulating the conductance of the nanoFET. Significantly, by using multiple branched SiNW FETs, the authors demonstrated multiplexed intracellular electrical recordings from both single cells and cell networks.

A limitation of these chip-based 3D nano-bioprobes has been a difficulty in exploiting the nanometer-scale probe resolution in a deterministic manner to record from specific cell regions and/or subcellular structures. To overcome this limitation, Qing et al. fabricated free-standing probes with a kinked SiNW nanoFET sensors.<sup>558</sup> Under a standard microscope, these probes were manipulated in 3D space to target specific regions and obtain stable, full-amplitude intracellular action potential spikes. Compared to the signal measured from patch-clamp probes on the same cell, the free-standing NW probe showed the same amplitude and temporal properties (Figure 22d), thus demonstrating the capability to record true intracellular (vs. intracellular-like) properties.

The substantial progress in intracellular recording described above was made possible by the availability of nanostructures with similar characteristic length scales to natural biological functional substructures. Semiconductor NW building blocks excel among nanomaterials in their capabilities to be rationally designed and synthesized with complex motifs with near molecular-scale precision. It is worth noting that applications of semiconductor NWs in biology are still at an early stage with future research needed to better understand and ultimately exploit the biochemical mechanisms yield nanoFET-cell interfaces.

**4.4.4. Intracellular MEA-based Nanopillars**—Substantial effort has been placed on the development of vertical NW electrode arrays. In 2012, Park and coworkers demonstrated parallel electrical interfacing to mammalian neurons using vertical NW electrode arrays (Figure 23a–c).<sup>560</sup> The NWs in the arrays were 150 nm in diameter and 3 μm in height with Ti/Au metallic tips, where each addressable electrode consisted of 9 NWs. To achieve recording it was necessary to apply voltage/current pulses, which can electroporate the cell membrane, although the spike amplitudes was much smaller than true intracellular signals (Figure 23d). In parallel, Cui and coworkers reported using vertical Pt NWs electrodes (150 nm in diameter and 1–2 μm in height) to record extracellular and intracellular action potentials from cultured cardiomyocytes, although the peak amplitudes were less than full-amplitude intracellular action potential.<sup>561</sup> This work also used electroporation to assist short-term penetration of the NWs across the cell membrane. In these two vertical metallic NW studies, the intracellular-like access gained by electroporation was transient, in contrast to the long-term access of lipid-coated SiNW FETs reported by the Lieber group. Notably, Melosh and coworkers have also shown that proper surface functionalization can help electrodes similar to the Park and Cui studies to gain intracellular access.<sup>562–565</sup>

More recently, Cui and coworkers have reported MEA-based nanoelectrodes consisting of iridium oxide (IrO<sub>2</sub>) nanotubes.<sup>566</sup> When these IrO<sub>2</sub> nanotube-based chips were used as a

substrate for cardiomyocytes culture, they reported that the cell membrane wrapped around the vertical nanotubes and protruded into the hollow spacing between adjacent nanotubes, thus suggesting that the nanotube array geometry could be beneficial for creating tight cell-electrode junctions similar to that achieved with FGSEs. Consistent with this structural observation, the authors observed larger and more stable intracellular action potentials from the beating cardiomyocytes with amplitudes closer to expected full amplitude measured with patch-clamp micropipettes.

The above results show that vertical NWs can bridge microelectrode-cell interfaces and allow direct access to intracellular information like FGSEs. However, the current vertical NW MEAs have several limitations, including (i) high electrochemical impedance due to the small contact area, which has generally been overcome by using multiple NWs as a single electrode, and (ii) recorded intracellular potentials that are about ten times lower than the patch-clamp signals. Future research on the effects of NW surface modification should be investigated to improve the internalization of these NW-based MEA electrodes as well as cell sealing, which could improve the stability and signal-to-noise ratio of the observed signals.

## 5. NANOELECTRONICS-TISSUE INTERFACES & ELECTROPHYSIOLOGICAL RECORDING

Making effective electrode-tissue interfaces requires consideration of the interfacial contact between electrodes and the 3D cell networks comprising functional tissues. In this regard, the position, shape, and size of an electrode with respect to the target tissue are all critical factors determining this contact or coupling. Moreover, given the intrinsic 3D interconnectivity of cells in tissues, consideration of the mechanical properties and connectivity of the nanoelectronic devices will also be critical. These latter factors are typically not considered in recording from single cells for 2D in-vitro cell cultures. Previously, several different types of micro- and nanostructures based electrodes have been used as tools for interfacing to tissues,<sup>567-570</sup> although they are outside the scope of this review. Below we will introduce cutting-edge studies that have exploited SiNW and graphene transistors for interfacing to brain and heart tissues, and additionally, will review how their integration into flexible electronics can open up new opportunities in bioelectronics.

### 5.1. Acute Brain Slice Studies with Nanowire Transistors

In 2009, Qing et al. reported studies SiNW FET arrays fabricated on transparent substrates were interfaced to acute brain slices to yield sub-millisecond temporal resolution and better than 10  $\mu\text{m}$  spatial resolution.<sup>173</sup> The transparent device chip allowed for imaging of individual cell bodies and identifying areas of healthy neurons on both upper and lower tissue surfaces. The small active device area (0.06  $\mu\text{m}^2$ ) and array spacing (3  $\mu\text{m}$ ) enable highly localized multiplexed measurements of neuronal activities and, for example, provided information addressing signal propagation in the lateral olfactory tract and functional neural connectivity in the olfactory cortex. Figure 24a shows a NW FET array under an acute brain slice that was stimulated at different locations. Based on the time and distance difference for

stimulation, it was possible to estimate a propagation rate 1.6–2 m/s in the lateral olfactory tract. To demonstrate the capability to probe the activity patterns, eight devices within a four-by-four array were simultaneously monitored while stimulating at eight different locations in the lateral olfactory tract (Figure 24b). Similar responses are obtained by each device irrespective to the stimulation positions after a strong stimulation that can activate all axons fibers, as revealed in Figure 24c. Reducing the stimulation intensity, such that only a limited number of axon are activated, yielded data (Figure 24d) that unambiguously revealed device specific features. In this weak stimulation regime, 2D activity maps from all eight devices (Figure 24e) demonstrated clearly heterogeneous activity and unique pairwise activity correlations for different stimulation spots. For example, the signals from devices 1 and 8 showed close correlation for 5/8 stimulation spots while those from devices 3 and 4 show close correlation for only 3/8 stimulation spots. These studies provided the first example of how highly localized direct electrical recording from intact neural networks using nanoelectronic devices could serve as a powerful approach to visualize the dynamic, functional neural networks and thus provide key information necessary to understand circuits and plasticity.

## 5.2. Cardiac Tissue Studies with Nanowire Transistors

Spontaneous beating embryonic chicken hearts were also studied using bottom-up SiNW FETs on planar substrates (Figure 25a, b).<sup>571</sup> The fabrication process yields protruding NW FET channels from the underlying chip, and thus could enhance coupling to heart tissue. Simultaneous recordings from a beating heart using a NW FET and a conventional glass pipette (Figure 25c) showed close temporal correlation except for a ~100 ms delay in the NW FET peak consistent with the separation of electrodes. Individual signals recorded from FET devices exhibited two characteristic components; that is, initial fast and subsequent slower ones. Further measurement made with and without blebbistatin, which prevents contraction while maintaining ion channels excitability, demonstrated that the fast component was associated with ion-channel current. Studies of the fast transient peak mad as a function of water-gate potential showed a conductance change from ca. 55 to 11 nS while the voltage-calibrated signals were constant,  $5.1 \pm 0.4$  mV (Figure 25d). The relatively constant recorded junction voltage confirmed the robust nanoFET/heart interface.

Last, the authors also fabricated NW FET devices on a flexible polymer substrate (Figure 25e) which enabled simultaneous recording from an isolated beating heart from multiple devices (Figure 25f). Notably, the calibrated voltages associated with the fast transient for three NW FET devices,  $5.3 \pm 0.2$ ,  $4.6 \pm 0.1$ , and  $5.3 \pm 0.2$  mV, further highlight the reproducibility of the nanoFET/heart interfaces. Moreover, the significantly larger signal-to-noise ratio for the fast transient implies a tighter interface contact due to the flexible substrate.

## 5.3. Cardiac Tissue Studies with Graphene Transistors

More recently, graphene FETs have also been used to record from newborn rat hearts.<sup>546</sup> Graphene FET devices with channel widths ranging from 10  $\mu\text{m}$  to 200 nm, were interfaced to the spontaneously beating hearts, and the local field potential was recorded as a current change in the FET (Figure 26a). Interestingly, measured signals recorded from both planar

and suspended graphene devices (Figure 26b) show regularly spaced spikes with a fast biphasic peak that lasts for milliseconds and consistent with extracellular recording from fast sodium ion channels that open at the start of each AP/heartbeat. In addition, the suspended devices yield an increased (>3-fold) signal amplitude and decreased (~2-fold) noise, thus allowing the much weaker ionic currents of calcium-ion channels to be resolved.

#### 5.4. 3D Nano-bioelectronic Hybrids

An important goal in tissue engineering is to construct culture systems as close as possible to the biological, physical and chemical environment of the natural extracellular matrix (ECM).<sup>572</sup> 2D bioelectronics have been used in studies of engineered tissues,<sup>573</sup> although the recording devices are not capable of mapping the critical 3D behavior of the tissue as a whole. To overcome this basic limitation requires the development of nanoelectronic recording devices in a 3D architecture, which necessitates the following features: (i) macroporous structures to allow for cell interpenetration during culture; (ii) nanometer to micrometer scale structural features consistent with the ECM or tissue scaffolds; and (iii) mechanical properties similar to ECM for tissue development.<sup>7,19</sup>

Tian et al. demonstrated the first example of using macroporous NW nanoelectronic scaffolds (nanoES) to develop innervated synthetic tissues.<sup>21</sup> In this new paradigm, SiNW transistors were fabricated into network structures, where the network, which contains electrical interconnects needed to address the nanoFETs, was designed to have feature sizes and porosities similar to conventional passive tissue scaffold. Second, the nanoES was released from the underlying substrate and configured as a 3D macroporous scaffold by either stress-induced self-organization or external forces. The porosity of nanoES can exceed 99%, which renders the scaffold high flexibility (Figure 27a, b). Last, the nanoES was combined with biodegradable ECMs, seeded with cells and then the assembly was cultured to produce synthetic tissues innervated in 3D with nanoFETs.

The structure of a representative nanoES/cardiac hybrid characterized by confocal fluorescence microscopy and epifluorescence microscopy (Figure 27c, d) highlights the high density of cardiomyocytes in close contact with nanoES components. Clear striations of cardiac tissue, indicative of mature tissue, were also observed. The monitoring capability of 3D nanoES/cardiac hybrid was demonstrated by recording from a single-NW FET located below the construct surface as shown in Figure 27e. The data revealed regularly spaced spikes with a frequency of ~1 Hz, calibrated potential change of ~2–3 mV, signal-to-noise ratio of 3 and ~2 ms width, all of which agree well with expectations for extracellular recordings from cardiomyocytes. Moreover, addition of norepinephrine, a drug that stimulates cardiac contraction, showed a twofold increase of the contraction frequency. Given the capability to resolve action potentials with single-shot submillisecond time resolution in 3D (Figure 27f), this work suggests substantial potential for the nanoES/cardiac hybrids and other tissue hybrids as a new paradigm for 3D monitoring and screening of drugs.

Further development of the nanoES paradigm has been achieved in the seamless incorporation of active nanoelectronic networks within 3D materials, where active monitoring and control of host systems have been exhibited by multifunctional NW

electronics. For example, Liu et al. reported the conversion of ordered 2D NW nanoelectronics precursors into ordered, 3D interconnected and addressable macroporous nanoelectronic networks.<sup>22</sup> Hundreds of addressable NW devices, with feature sizes from 10-nm scale (for device elements) to 10- $\mu$ m scale (for electrical and structural interconnections), were incorporated in these 3D networks (Figure 28). Significantly, simultaneous NW photocurrent and confocal microscopy imaging studies demonstrated that it was possible to localize NW positions inside 3D hybrid materials with  $\sim$ 14-nm resolution. This method should prove particularly useful in future for mapping the positions of the nanodevices to high-resolution with respect to cells. The success of integrating 3D multifunctional nanoelectronics with biological hosts indicates the capability of fabricating truly 3D nanoelectronic circuits and subsequent 3D incorporation of these multifunctional circuits into living systems for smart materials and even “cyborg” tissues, although additional work will be needed before the nanoES-based hybrids can be used as implants *in vivo*. Last, it should be noted that basic nanoES paradigm is amenable to incorporation of additional types of functional devices, including photonic devices as well as strain and biochemical sensors, and these could further broaden the capabilities and opportunities for *in vitro* and *in vivo* studies of the brain and heart in the future.

### 5.5.Injectable Electronics

The mismatch of mechanical properties represents an essential challenge at the tissue/electrode interface. Tissues are soft and flexible, also with interior cell migration while the implanted electronics made, for example, of metal or silicon, have rigid nonporous structures. This difference results in two disadvantages. First, rigidity can yield incomplete and/or ineffective contacts that lead to weak signals that may be overwhelmed by noise.<sup>574–576</sup> Second and perhaps more important, these rigid probes are known to illicit a chronic immune response that results in the build-up of glial scar tissue around the probe, where the biologically inactive scar tissue can diminish or eliminate recorded and/or stimulation signals.<sup>577–578</sup> To overcome these longstanding limitations of existing implantable electrode probes requires greater attention to the importance of the electrode/tissue interfaces and matching of overall probe/tissue mechanical properties.

Significantly, the Lieber group recently proposed and demonstrated a new paradigm that overcomes these long-standing challenges through syringe injection of centimeter-scale macroporous electronic networks.<sup>23,174</sup> In this new approach (Figure 29a), the syringe is loaded with the ultra-flexible mesh, inserted into tissue or cavity, and then the mesh is injected while simultaneously retracting the needle. The mesh structure is critical for controlling the bending stiffness and allowing loading/injection. Specifically, the angle  $\alpha$  (Figure 29b) determines the bending stiffness of the unit cell. The authors found that when  $\alpha = 45^\circ$ , the mesh electronics can be smoothly delivered through a needles with inner diameters that were  $>30$  times smaller than the original mesh width ( $W$ ).

Notably, studies of the chronic tissue response following injection of the macroporous mesh into live rodent brains (Figure 29c) demonstrated several new and exciting features, including (i) filling-in of neural tissue through the macroporous network, (ii) minimal or absence of astrocyte proliferation in the vicinity of the injected probe, and correspondingly, (iii)

attractive interactions between the neurons and the macroporous mesh, which lead to the formation of tight electronics/cell junctions that are ideal for recording. Indeed, the mesh electronics have proved to be able to record well-defined neural activity from live mice brains (Figure 29d). In this case, the rigid shell of the syringe allowed placement of the mesh in specific brain regions. In parallel, they also developed another method to implant the ultraflexible 3D macroporous electronic device into rodent brains by rapid freezing in liquid nitrogen and inserting the probe in frozen state.<sup>24</sup> Significantly, the chronic histology studies, which revealed filling-in of neural tissue through the macroporous network and attractive neuron probe interactions, contrast results from other solid and more rigid probe designs and are consistent with a unique long-term stability and biocompatibility of the ultra-flexible mesh probe/tissue interface. Although it will be important in future studies to develop these probes further, for example by extending the chronic histology studies to shorter and longer times, and increasing the number of sensor elements available for multiplexed recording and/or introducing stimulation capabilities, the new paradigm of syringe injectable macroporous mesh electronics promises to be transformative in capabilities for stable chronic brain activity mapping through the development of implants for next-generation brain machine interfaces.

## 6. CONCLUSIONS

In this review, two general classes of nano-bioelectronic sensor devices were discussed. First, we introduced nanoFET sensors for label-free, real-time detection of chemical and biomolecular species. The synthesis of the crucial building blocks for these sensors, including SiNWs, SWNTs and graphene, was overviewed in addition to discussing basic characteristics of FET devices and nanoFET sensors configured from these nanomaterials. Representative sensing studies of key biomolecular targets were then reviewed, including detection of proteins, nucleic acids, viruses, and small molecules. These studies have demonstrated clearly the success of the nanoFET biosensor concept<sup>388</sup> across nanomaterials building blocks, where the ability to diversify sensing targets through surface-functionalization with conjugate probe molecules/receptors. This latter functionalization point was further highlighted through review of multiplexed electrical detection studies where multiple nanoFET devices in the same array were modified with different probe molecules to allow for simultaneous electrical recording of different disease marker proteins and viruses. In addition, we discussed investigations focused on addressing and improving the ultimate sensitivity of nanoFET biosensors, including (i) the use of 3D branched NWs, (ii) detection in the FET subthreshold regime, (iii) reduction of the effect of Debye screening, (iv) the use of electrokinetic effects to enhance local target concentration, and (v) measurements in the frequency domain. The sum of these diverse and important studies has now defined a relatively comprehensive understanding of the original nanoFET concept<sup>388</sup> for chemical/biological detection. In addition, in section 3.4 we discussed several basic challenges as well as potential research future directions that could improve further the capabilities of nanoFET biosensors. Beyond these suggested directions and given the increasingly well-defined characteristics of nanodevice/receptor interfaces, we believe it would also be timely to consider modeling and simulation studies since these could provide

both deeper understanding and feedback required for further improvements in, for example, the sensitivity in physiological environments.

In addition, we believe there are important opportunities to impact both applications and fundamental research in the life sciences and health-care with nanoFET biosensors. For example, the existing state of the nanoFET technology is now suitable as a general multiplexed detection platform when either external or on-chip sample preparation is employed to lower ionic strength of physiological samples. Developing large nanoFET sensor arrays could also move beyond current technologies and take advantage of information emerging from genomics and proteomics to improve the diagnosis and treatment of cancer and other complex diseases, where real-time data acquisition possible with the nanoFETs would serve as unique capability compared to optical methodologies. Moreover, we suggest that further development of methods that enable direct nanoFET detection in physiological fluids will be especially impactful in near-term development of *in-vitro* clinical/healthcare diagnostics, as well as opening up unique opportunities associated with real-time detection of proteins/protein expression, nucleic acids and small molecule 'drugs' using nanoFETs directly implanted into cells and tissues.

The second part of the review focused on studies extending the use of nano-bioelectronic devices to extracellular and intracellular electrophysiological recording/stimulation from live cells, including neurons and cardiomyocytes. The results obtained using emerging nano-bioelectronic tools have demonstrated the capability to obtain higher spatial and temporal resolution data than possible using more established MEA and patch-clamp technologies. Nevertheless, the fact that many of the nanoelectronic devices have been constrained to planar substrates has made it difficult to demonstrate these unique resolution capabilities in a compelling biological problem. We believe that the more recent efforts incorporating nanoelectronics into three-dimensional synthetic or *in vivo* tissues offers perhaps the greatest opportunities for revolutionary advances.<sup>21–24</sup> In this direction, one can envision building many nanoelectronic devices into cellular circuitry and merging this circuitry in a seamless manner with biological information processing systems such as the brain. Extending such concepts to rational design and fabrication of multifunctional nano-bioelectronic device networks and circuits could further inspire and lead new understanding of the interplay between nanostructures and biosystems. In particular, we suggest strongly that the frontier of the nanoelectronics-brain interface focused on *in vivo* brain activity mapping and modulation with high spatial and temporal resolution represents a truly unique opportunity to impact fundamental research and ultimately healthcare with a substantial benefit to society worldwide. More generally, as we take advantage of the uniquely small sizes of nanoelectronic devices organized into arrays and circuits that have similar connectivity, feature sizes and mechanical properties as the cell networks comprising living tissues of interest (e.g., the brain), we begin to blur the distinction between the nonliving electronic and living biological systems, and we suggest that this will lead to major and sometimes unexpected opportunities in understanding complex biological systems, diseases and potential new therapeutic directions.

## Acknowledgments

We thank Ying Fang (National Center for Nanoscience and Technology) for helpful discussion and Teng Gao (Harvard University) for help with preparing the table of contents graphic. C.M.L. thanks the Air Force Office of Scientific Research, Fidelity Biosciences Fund, McKnight Foundation Technological Innovations in Neurosciences Award, NIH Director's Pioneer Award, National Security Science and Engineering Faculty Fellow Award, and Star Family Fund for generous support of the studies from the authors' laboratory that contributed to this review.

## References

1. Wang J. Glucose biosensors: 40 years of advances and challenges. *Electroanal.* 2001; 13:983–988.
2. Wang J. Electrochemical glucose biosensors. *Chem Rev.* 2008; 108:814–825. [PubMed: 18154363]
3. Chen C, Xie Q, Yang D, Xiao H, Fu Y, Tan Y, Yao S. Recent Advances in Electrochemical Glucose Biosensors: A Review. *RSC Adv.* 2013; 3:4473–4491.
4. Benabid AL. Deep Brain Stimulation for Parkinson's Disease. *Curr Opin Neurobiol.* 2003; 13:696–706. [PubMed: 14662371]
5. Kringelbach ML, Jenkinson N, Owen SL, Aziz TZ. Translational principles of deep brain stimulation. *Nat Rev Neurosci.* 2007; 8:623–635. [PubMed: 17637800]
6. Lieber CM. Semiconductor nanowires: A platform for nanoscience and nanotechnology. *MRS Bull.* 2011; 36:1052–1063. [PubMed: 22707850]
7. Duan X, Lieber CM. Nanoelectronics meets biology: from new nanoscale devices for live-cell recording to 3D innervated tissues. *Chem Asian J.* 2013; 8:2304–2314. [PubMed: 23946279]
8. Hu J, Odom TW, Lieber CM. Chemistry and physics in one dimension: synthesis and properties of nanowires and nanotubes. *Acc Chem Res.* 1999; 32:435–445.
9. Lieber CM. Nanoscale science and technology: building a big future from small things. *MRS Bull.* 2003; 28:486–491.
10. Dasgupta NP, Sun J, Liu C, Brittan S, Andrews SC, Lim J, Gao H, Yan R, Yang P. Semiconductor Nanowires—Synthesis, Characterization, and Applications. *Adv Mater.* 2014; 26:2137–2184. [PubMed: 24604701]
11. Zhu Y, Murali S, Cai W, Li X, Suk JW, Potts JR, Ruoff RS. Graphene and graphene oxide: synthesis, properties, and applications. *Adv Mater.* 2010; 22:3906–3924. [PubMed: 20706983]
12. Gupta AK, Gupta M. Synthesis and surface engineering of iron oxide nanoparticles for biomedical applications. *Biomaterials.* 2005; 26:3995–4021. [PubMed: 15626447]
13. Patolsky F, Lieber CM. Nanowire nanosensors. *Mater Today.* 2005; 8:20–28.
14. Patolsky F, Zheng GF, Lieber CM. Nanowire-based biosensors. *Anal Chem.* 2006; 78:4260–4269. [PubMed: 16856252]
15. Patolsky F, Timko BP, Zheng G, Lieber CM. Nanowire-based nanoelectronic devices in the life sciences. *MRS Bull.* 2007; 32:142–149.
16. Chen KI, Li BR, Chen YT. Silicon Nanowire Field-Effect Transistor-Based Biosensors for Biomedical Diagnosis and Cellular Recording Investigation. *Nano Today.* 2011; 6:131–154.
17. Tian B, Lieber CM. Design, synthesis, and characterization of novel nanowire structures for photovoltaics and intracellular probes. *Pure Appl Chem.* 2011; 83:2153–2169. [PubMed: 22707797]
18. Yang L, Li Y, Fang Y. Nanodevices for Cellular Interfaces and Electrophysiological Recording. *Adv Mater.* 2013; 25:3881–3887. [PubMed: 24048974]
19. Tian B, Lieber CM. Synthetic nanoelectronic probes for biological cells and tissues. *Annu Rev Anal Chem.* 2013; 6:31–51.
20. Cohen-Karni T, Lieber CM. Nanowire Nanoelectronics: Building Interfaces with Tissue and Cells at the Natural Scale of Biology. *Pure Appl Chem.* 2013; 85:883–901.
21. Tian B, Liu J, Dvir T, Jin L, Tsui JH, Qing Q, Suo Z, Langer R, Kohane DS, Lieber CM. Macroporous nanowire nanoelectronic scaffolds for synthetic tissues. *Nat Mater.* 2012; 11:986–994. [PubMed: 22922448]

22. Liu J, Xie C, Dai X, Jin L, Zhou W, Lieber CM. Multifunctional three-dimensional macroporous nanoelectronic networks for smart materials. *Proc Natl Acad Sci USA*. 2013; 110:6694–6699. [PubMed: 23569270]
23. Liu J, Fu TM, Cheng Z, Hong G, Zhou T, Jin L, Duvvuri M, Jiang Z, Kruskal P, Xie C, et al. Syringe-injectable electronics. *Nat Nanotechnol*. 2015; 10:629–636. [PubMed: 26053995]
24. Xie C, Liu J, Fu TM, Dai X, Zhou W, Lieber CM. Three-dimensional macroporous nanoelectronic networks as minimally invasive brain probes. *Nat Mater*. 2015; 14:1286–1292. [PubMed: 26436341]
25. Zhou X, Boey F, Zhang H. Controlled growth of single-walled carbon nanotubes on patterned substrates. *Chem Soc Rev*. 2011; 40:5221–5231. [PubMed: 21713267]
26. Schmidt V, Wittemann JV, Senz S, Gösele U. Silicon nanowires: a review on aspects of their growth and their electrical properties. *Adv Mater*. 2009; 21:2681–2702.
27. Schmidt V, Wittemann JV, Gösele U. Growth, Thermodynamics, and Electrical Properties of Silicon Nanowires. *Chem Rev*. 2010; 110:361–388. [PubMed: 20070117]
28. Shao M, Ma DDD, Lee ST. Silicon nanowires—synthesis, properties, and applications. *Eur J Inorg Chem*. 2010; 2010:4264–4278.
29. Dai H. Carbon nanotubes: synthesis, integration, and properties. *Acc Chem Res*. 2002; 35:1035–1044. [PubMed: 12484791]
30. Terrones M. Science and technology of the twenty-first century: synthesis, properties, and applications of carbon nanotubes. *Annu Rev Mater Res*. 2003; 33:419–501.
31. Kumar M, Ando Y. Chemical vapor deposition of carbon nanotubes: a review on growth mechanism and mass production. *J Nanosci Nanotechnol*. 2010; 10:3739–3758. [PubMed: 20355365]
32. Jourdain V, Bichara C. Current understanding of the growth of carbon nanotubes in catalytic chemical vapour deposition. *Carbon*. 2013; 58:2–39.
33. Nessim GD. Properties, synthesis, and growth mechanisms of carbon nanotubes with special focus on thermal chemical vapor deposition. *Nanoscale*. 2010; 2:1306–1323. [PubMed: 20820718]
34. Edwards RS, Coleman KS. Graphene synthesis: relationship to applications. *Nanoscale*. 2013; 5:38–51. [PubMed: 23160190]
35. Hong G, Zhou M, Zhang R, Hou S, Choi W, Woo YS, Choi JY, Liu Z, Zhang J. Separation of Metallic and Semiconducting Single-Walled Carbon Nanotube Arrays by “Scotch Tape”. *Angew Chem Int Ed*. 2011; 50:6819–6823.
36. Schwierz F. Graphene transistors. *Nat Nanotechnol*. 2010; 5:487–496. [PubMed: 20512128]
37. Sharma BK, Ahn JH. Graphene based field effect transistors: Efforts made towards flexible electronics. *Solid State Electron*. 2013; 89:177–188.
38. Zhan B, Li C, Yang J, Jenkins G, Huang W, Dong X. Graphene Field-Effect Transistor and Its Application for Electronic Sensing. *Small*. 2014; 10:4042–4065. [PubMed: 25044546]
39. Long YZ, Yu M, Sun B, Gu CZ, Fan Z. Recent advances in large-scale assembly of semiconducting inorganic nanowires and nanofibers for electronics, sensors and photovoltaics. *Chem Soc Rev*. 2012; 41:4560–4580. [PubMed: 22573265]
40. Liu X, Long YZ, Liao L, Duan X, Fan Z. Large-scale integration of semiconductor nanowires for high-performance flexible electronics. *ACS Nano*. 2012; 6:1888–1900. [PubMed: 22364279]
41. Liu JW, Liang HW, Yu SH. Macroscopic-Scale Assembled Nanowire Thin Films and Their Functionalities. *Chem Rev*. 2012; 112:4770–4799. [PubMed: 22708842]
42. Su B, Wu Y, Jiang L. The art of aligning one-dimensional (1D) nanostructures. *Chem Soc Rev*. 2012; 41:7832–7856. [PubMed: 22990498]
43. Wang MC, Gates BD. Directed assembly of nanowires. *Mater Today*. 2009; 12:34–43.
44. Kwiat M, Cohen S, Pevzner A, Patolsky F. Large-scale ordered 1D-nanomaterials arrays: Assembly or not? *Nano Today*. 2013; 8:677–694.
45. Wu Y, Cui Y, Huynh L, Barrelet CJ, Bell DC, Lieber CM. Controlled growth and structures of molecular-scale silicon nanowires. *Nano Lett*. 2004; 4:433–436.
46. Lu W, Xie P, Lieber CM. Nanowire Transistor Performance Limits and Applications. *IEEE T Electron Dev*. 2008; 55:2859–2876.

47. Park WI, Zheng G, Jiang X, Tian B, Lieber CM. Controlled synthesis of millimeter-long silicon nanowires with uniform electronic properties. *Nano Lett.* 2008; 8:3004–3009. [PubMed: 18710294]
48. Hobbs RG, Petkov N, Holmes JD. Semiconductor nanowire fabrication by bottom-up and top-down paradigms. *Chem Mat.* 2012; 24:1975–1991.
49. Wang N, Cai Y, Zhang R. Growth of nanowires. *Mater Sci Eng, R.* 2008; 60:1–51.
50. Schmidt V, Wittemann J, Gosele U. Growth, thermodynamics, and electrical properties of silicon nanowires. *Chem Rev.* 2010; 110:361–388. [PubMed: 20070117]
51. Zhang RQ, Lifshitz Y, Lee ST. Oxide-Assisted Growth of Semiconducting Nanowires. *Adv Mater.* 2003; 15:635–640.
52. Ramanujam J, Shiri D, Verma A. Silicon nanowire growth and properties: A review. *Mater Express.* 2011; 1:105–126.
53. Teo BK, Sun X. Silicon-based low-dimensional nanomaterials and nanodevices. *Chem Rev.* 2007; 107:1454–1532. [PubMed: 17488056]
54. Tian B, Cohen-Karni T, Qing Q, Duan X, Xie P, Lieber CM. Three-Dimensional, Flexible Nanoscale Field-Effect Transistors as Localized Bioprobes. *Science.* 2010; 329:830–834. [PubMed: 20705858]
55. Morales AM, Lieber CM. A Laser Ablation Method for the Synthesis of Crystalline Semiconductor Nanowires. *Science.* 1998; 279:208–211. [PubMed: 9422689]
56. Zhang Y, Tang Y, Wang N, Yu D, Lee C, Bello I, Lee S. Silicon nanowires prepared by laser ablation at high temperature. *Appl Phys Lett.* 1998; 72:1835–1837.
57. Cui Y, Lauhon LJ, Gudixsen MS, Wang JF, Lieber CM. Diameter-Controlled Synthesis of Single-Crystal Silicon Nanowires. *Appl Phys Lett.* 2001; 78:2214–2216.
58. Kodambaka S, Tersoff J, Reuter M, Ross F. Diameter-independent kinetics in the vapor-liquid-solid growth of Si nanowires. *Phys Rev Lett.* 2006; 96:096105. [PubMed: 16606284]
59. Schubert L, Werner P, Zakharov N, Gerth G, Kolb F, Long L, Gösele U, Tan T. Silicon nanowhiskers grown on <111> Si substrates by molecular-beam epitaxy. *Appl Phys Lett.* 2004; 84:4968–4970.
60. Zakharov N, Werner P, Gerth G, Schubert L, Sokolov L, Gösele U. Growth phenomena of Si and Si/Ge nanowires on Si (111) by molecular beam epitaxy. *J Cryst Growth.* 2006; 290:6–10.
61. Kanungo PD, Zakharov N, Bauer J, Breitenstein O, Werner P, Gosele U. Controlled in situ boron doping of short silicon nanowires grown by molecular beam epitaxy. *Appl Phys Lett.* 2008; 92:263107–263109.
62. Wen CY, Reuter M, Tersoff J, Stach E, Ross F. Structure, Growth Kinetics, and Ledge Flow during Vapor–Solid–Solid Growth of Copper-Catalyzed Silicon Nanowires. *Nano Lett.* 2009; 10:514–519. [PubMed: 20041666]
63. Wang N, Tang Y, Zhang Y, Lee C, Lee S. Nucleation and growth of Si nanowires from silicon oxide. *Phys Rev B.* 1998; 58:R16024.
64. Wang N, Tang Y, Zhang Y, Lee C, Bello I, Lee S. Si nanowires grown from silicon oxide. *Chem Phys Lett.* 1999; 299:237–242.
65. Shi WS, Peng HY, Zheng YF, Wang N, Shang NG, Pan ZW, Lee CS, Lee ST. Synthesis of large areas of highly oriented, very long silicon nanowires. *Adv Mater.* 2000; 12:1343–1345.
66. Pan Z, Dai Z, Xu L, Lee S, Wang Z. Temperature-controlled growth of silicon-based nanostructures by thermal evaporation of SiO powders. *J Phys Chem B.* 2001; 105:2507–2514.
67. Ma D, Lee C, Au F, Tong S, Lee S. Small-diameter silicon nanowire surfaces. *Science.* 2003; 299:1874–1877. [PubMed: 12595610]
68. Wagner R, Ellis W. Vapor-liquid-solid mechanism of single crystal growth. *Appl Phys Lett.* 1964:89–90.
69. Lieber, C.; Morales, A.; Sheehan, P.; Wong, E.; Yang, P. Proceedings of the Robert A. Welch Foundation 40th Conference on Chemical Research: Chemistry on the Nanometer Scale; 1997; p. 165-187.
70. Wu Y, Yang P. Direct observation of vapor-liquid-solid nanowire growth. *J Am Chem Soc.* 2001; 123:3165–3166.

71. Schmidt V, Senz S, Gösele U. Diameter-dependent growth direction of epitaxial silicon nanowires. *Nano Lett.* 2005; 5:931–935. [PubMed: 15884897]
72. Lugstein A, Steinmair M, Hyun Y, Hauer G, Pongratz P, Bertagnolli E. Pressure- induced orientation control of the growth of epitaxial silicon nanowires. *Nano Lett.* 2008; 8:2310–2314. [PubMed: 18624392]
73. Tian B, Xie P, Kempa TJ, Bell DC, Lieber CM. Single-crystalline kinked semiconductor nanowire superstructures. *Nat Nanotechnol.* 2009; 4:824–829. [PubMed: 19893521]
74. Lauhon L, Gudiksen MS, Lieber CM. Semiconductor nanowire heterostructures. *Phil Trans R Soc A.* 2004; 362:1247–1260. [PubMed: 15306476]
75. Agarwal R. Heterointerfaces in Semiconductor Nanowires. *Small.* 2008; 4:1872–1893. [PubMed: 18932190]
76. Wu Y, Fan R, Yang P. Block-by-block growth of single-crystalline Si/SiGe superlattice nanowires. *Nano Lett.* 2002; 2:83–86.
77. Björk M, Ohlsson B, Sass T, Persson A, Thelander C, Magnusson M, Deppert K, Wallenberg L, Samuelson L. One-Dimensional Steeplechase for Electrons Realized. *Nano Lett.* 2002; 2:87–89.
78. Björk M, Ohlsson B, Sass T, Persson A, Thelander C, Magnusson M, Deppert K, Wallenberg L, Samuelson L. One-Dimensional Heterostructures in Semiconductor Nanowhiskers. *Appl Phys Lett.* 2002; 80:1058–1060.
79. Gudiksen MS, Lauhon LJ, Wang J, Smith DC, Lieber CM. Growth of nanowire superlattice structures for nanoscale photonics and electronics. *Nature.* 2002; 415:617–620. [PubMed: 11832939]
80. Wu Y, Xiang J, Yang C, Lu W, Lieber CM. Single-crystal metallic nanowires and metal/ semiconductor nanowire heterostructures. *Nature.* 2004; 430:61–65. [PubMed: 15229596]
81. Lin YC, Lu KC, Wu WW, Bai J, Chen LJ, Tu K, Huang Y. Single crystalline PtSi nanowires, PtSi/Si/PtSi nanowire heterostructures, and nanodevices. *Nano Lett.* 2008; 8:913–918. [PubMed: 18266331]
82. Yang C, Zhong ZH, Lieber CM. Encoding electronic properties by synthesis of axial modulation-doped silicon nanowires. *Science.* 2005; 310:1304–1307. [PubMed: 16311329]
83. Kempa TJ, Tian B, Kim DR, Hu J, Zheng X, Lieber CM. Single and tandem axial p-i-n nanowire photovoltaic devices. *Nano Lett.* 2008; 8:3456–3460. [PubMed: 18763836]
84. Cohen-Karni T, Casanova D, Cahoon JF, Qing Q, Bell DC, Lieber CM. Synthetically Encoded Ultrashort-Channel Nanowire Transistors for Fast, Pointlike Cellular Signal Detection. *Nano Lett.* 2012; 12:2639–2644. [PubMed: 22468846]
85. Christesen JD, Pinion CW, Grumstrup EM, Papanikolas JM, Cahoon JF. Synthetically Encoding 10 nm Morphology in Silicon Nanowires. *Nano Lett.* 2013; 13:6281–6286. [PubMed: 24274858]
86. Luo Z, Jiang Y, Myers BD, Isheim D, Wu J, Zimmerman JF, Wang Z, Li Q, Wang Y, Chen X. Atomic gold-enabled three-dimensional lithography for silicon mesostructures. *Science.* 2015; 348:1451–1455. [PubMed: 26113718]
87. Lauhon LJ, Gudiksen MS, Wang D, Lieber CM. Epitaxial core-shell and core-multishell nanowire heterostructures. *Nature.* 2002; 420:57–61. [PubMed: 12422212]
88. Qian F, Gradecak S, Li Y, Wen CY, Lieber CM. Core/multishell nanowire heterostructures as multicolor, high-efficiency light-emitting diodes. *Nano Lett.* 2005; 5:2287–2291. [PubMed: 16277469]
89. Qian F, Li Y, Gradecak S, Park HG, Dong Y, Ding Y, Wang ZL, Lieber CM. Multi-quantum-well nanowire heterostructures for wavelength-controlled lasers. *Nat Mater.* 2008; 7:701–706. [PubMed: 18711385]
90. Kempa TJ, Kim SK, Day RW, Park HG, Nocera DG, Lieber CM. Facet-selective growth on nanowires yields multi-component nanostructures and photonic devices. *J Am Chem Soc.* 2013; 135:18354–18357. [PubMed: 24279423]
91. Mankin MN, Day RW, Gao R, No YS, Kim SK, McClelland AA, Bell DC, Park HG, Lieber CM. Facet-Selective Epitaxy of Compound Semiconductors on Faceted Silicon Nanowires. *Nano Lett.* 2015; 15:4776–4782. [PubMed: 26057208]

92. Day RW, Mankin MN, Gao R, No YS, Kim SK, Bell DC, Park HG, Lieber CM. Plateau–Rayleigh Crystal Growth of Periodic Shells on One-Dimensional Substrates. *Nat Nanotechnol.* 2015; 10:345–352. [PubMed: 25751303]
93. Cheng C, Fan HJ. Branched Nanowires: Synthesis and Energy Applications. *Nano Today.* 2012; 7:327–343.
94. Wang D, Qian F, Yang C, Zhong ZH, Lieber CM. Rational growth of branched and hyperbranched nanowire structures. *Nano Lett.* 2004; 4:871–874.
95. Dick KA, Deppert K, Larsson MW, Mårtensson T, Seifert W, Wallenberg LR, Samuelson L. Synthesis of branched ‘nanotrees’ by controlled seeding of multiple branching events. *Nat Mater.* 2004; 3:380–384. [PubMed: 15122221]
96. Wan Q, Huang J, Xie Z, Wang T, Dattoli EN, Lu W. Branched SnO<sub>2</sub> nanowires on metallic nanowire backbones for ethanol sensors application. *Appl Phys Lett.* 2008; 92:102101.
97. Wan Q, Dattoli EN, Fung WY, Guo W, Chen Y, Pan X, Lu W. High-performance transparent conducting oxide nanowires. *Nano Lett.* 2006; 6:2909–2915. [PubMed: 17163729]
98. Dick KA, Deppert K, Karlsson LS, Larsson MW, Seifert W, Wallenberg L, Samuelson L. Directed growth of branched nanowire structures. *MRS Bull.* 2007; 32:127–133.
99. Jung Y, Ko DK, Agarwal R. Synthesis and structural characterization of single-crystalline branched nanowire heterostructures. *Nano Lett.* 2007; 7:264–268. [PubMed: 17297988]
100. Zhou W, Pan A, Li Y, Dai G, Wan Q, Zhang Q, Zou B. Controllable fabrication of high-quality 6-fold symmetry-branched CdS nanostructures with ZnS nanowires as templates. *J Phys Chem C.* 2008; 112:9253–9260.
101. Jiang X, Tian B, Xiang J, Qian F, Zheng G, Wang H, Mai L, Lieber CM. Rational growth of branched nanowire heterostructures with synthetically encoded properties and function. *Proc Natl Acad Sci USA.* 2011; 108:12212–12216. [PubMed: 21730174]
102. Dong A, Tang R, Buhro WE. Solution-based growth and structural characterization of homo- and heterobranched semiconductor nanowires. *J Am Chem Soc.* 2007; 129:12254–12262. [PubMed: 17880075]
103. Cheng C, Liu B, Yang H, Zhou W, Sun L, Chen R, Yu SF, Zhang J, Gong H, Sun H. Hierarchical Assembly of ZnO Nanostructures on SnO<sub>2</sub> Backbone Nanowires: Low-Temperature Hydrothermal Preparation and Optical Properties. *ACS Nano.* 2009; 3:3069–3076. [PubMed: 19772329]
104. Zhou W, Cheng C, Liu J, Tay YY, Jiang J, Jia X, Zhang J, Gong H, Hng HH, Yu T. Epitaxial Growth of Branched  $\alpha$ -Fe<sub>2</sub>O<sub>3</sub>/SnO<sub>2</sub> Nano-Heterostructures with Improved Lithium-Ion Battery Performance. *Adv Funct Mater.* 2011; 21:2439–2445.
105. Liu J, Jiang J, Cheng C, Li H, Zhang J, Gong H, Fan HJ. Co<sub>3</sub>O<sub>4</sub> Nanowire@ MnO<sub>2</sub> Ultrathin Nanosheet Core/Shell Arrays: A New Class of High-Performance Pseudocapacitive Materials. *Adv Mater.* 2011; 23:2076–2081. [PubMed: 21413085]
106. Cheng C, Yan B, Wong SM, Li X, Zhou W, Yu T, Shen Z, Yu H, Fan HJ. Fabrication and SERS Performance of Silver-Nanoparticle-Decorated Si/ZnO Nanotrees in Ordered Arrays. *ACS Appl Mater Interfaces.* 2010; 2:1824–1828. [PubMed: 20515071]
107. Manna L, Scher EC, Alivisatos AP. Synthesis of soluble and processable rod-, arrow-, teardrop-, and tetrapod-shaped CdSe nanocrystals. *J Am Chem Soc.* 2000; 122:12700–12706.
108. Manna L, Milliron DJ, Meisel A, Scher EC, Alivisatos AP. Controlled growth of tetrapod-branched inorganic nanocrystals. *Nat Mater.* 2003; 2:382–385. [PubMed: 12764357]
109. Milliron DJ, Hughes SM, Cui Y, Manna L, Li J, Wang LW, Alivisatos AP. Colloidal nanocrystal heterostructures with linear and branched topology. *Nature.* 2004; 430:190–195. [PubMed: 15241410]
110. Wang D, Lieber CM. Inorganic materials: nanocrystals branch out. *Nat Mater.* 2003; 2:355–356. [PubMed: 12764360]
111. Yan H, He R, Johnson J, Law M, Saykally RJ, Yang P. Dendritic nanowire ultraviolet laser array. *J Am Chem Soc.* 2003; 125:4728–4729. [PubMed: 12696889]
112. Fardy M, Hochbaum AI, Goldberger J, Zhang MM, Yang P. Synthesis and thermoelectrical characterization of lead chalcogenide nanowires. *Adv Mater.* 2007; 19:3047–3051.

113. Bierman MJ, Lau YA, Jin S. Hyperbranched PbS and PbSe Nanowires and the Effect of Hydrogen Gas on Their Synthesis. *Nano Lett.* 2007; 7:2907–2912. [PubMed: 17672508]
114. Liu R, Li ZA, Zhang C, Wang X, Kamran MA, Farle M, Zou B. Single-Step Synthesis of Monolithic Comb-like CdS Nanostructures with Tunable Waveguide Properties. *Nano Lett.* 2013; 13:2997–3001. [PubMed: 23701186]
115. Bierman MJ, Lau YA, Kvit AV, Schmitt AL, Jin S. Dislocation-Driven Nanowire Growth and Eshelby Twist. *Science.* 2008; 320:1060–1063. [PubMed: 18451264]
116. Zhu J, Peng H, Marshall A, Barnett D, Nix W, Cui Y. Formation of chiral branched nanowires by the Eshelby Twist. *Nat Nanotechnol.* 2008; 3:477–481. [PubMed: 18685634]
117. Morin SA, Bierman MJ, Tong J, Jin S. Mechanism and kinetics of spontaneous nanotube growth driven by screw dislocations. *Science.* 2010; 328:476–480. [PubMed: 20413496]
118. Jin S, Bierman MJ, Morin SA. A new twist on nanowire formation: Screw-dislocation-driven growth of nanowires and nanotubes. *J Phys Chem Lett.* 2010; 1:1472–1480.
119. Jiang Z, Qing Q, Xie P, Gao R, Lieber CM. Kinked p-n Junction Nanowire Probes for High Spatial Resolution Sensing and Intracellular Recording. *Nano Lett.* 2012; 12:1711–1716. [PubMed: 22309132]
120. Xu L, Jiang Z, Qing Q, Mai L, Zhang Q, Lieber CM. Design and synthesis of diverse functional kinked nanowire structures for nanoelectronic bioprobes. *Nano Lett.* 2013; 13:746–751. [PubMed: 23273386]
121. Messer B, Song JH, Yang P. Microchannel networks for nanowire patterning. *J Am Chem Soc.* 2000; 122:10232–10233.
122. Huang Y, Duan X, Wei Q, Lieber CM. Directed assembly of one-dimensional nanostructures into functional networks. *Science.* 2001; 291:630–633. [PubMed: 11158671]
123. Huang Y, Lieber CM. Integrated nanoscale electronics and optoelectronics: Exploring nanoscale science and technology through semiconductor nanowires. *Pure Appl Chem.* 2004; 76:2051–2068.
124. Yan S, Lu L, Meng H, Huang N, Xiao Z. Scalable alignment and transfer of nanowires based on oriented polymer nanofibers. *Nanotechnology.* 2010; 21:095303. [PubMed: 20124660]
125. Li WZ, Wei W, Chen JY, He JX, Xue SN, Zhang J, Liu X, Li X, Fu Y, Jiao YH. Stirring-assisted assembly of nanowires at liquid–solid interfaces. *Nanotechnology.* 2013; 24:105302. [PubMed: 23416634]
126. Zhou X, Zhou Y, Ku JC, Zhang C, Mirkin CA. Capillary force-driven, large-area alignment of multi-segmented nanowires. *ACS Nano.* 2014; 8:1511–1516. [PubMed: 24450422]
127. Kim F, Kwan S, Akana J, Yang P. Langmuir-Blodgett nanorod assembly. *J Am Chem Soc.* 2001; 123:4360–4361. [PubMed: 11457213]
128. Kwan S, Kim F, Akana J, Yang P. Synthesis and assembly of BaWO<sub>4</sub> nanorods. *Chem Commun.* 2001:447–448.
129. Tao A, Kim F, Hess C, Goldberger J, He R, Sun Y, Xia Y, Yang P. Langmuir-Blodgett silver nanowire monolayers for molecular sensing using surface-enhanced Raman spectroscopy. *Nano Lett.* 2003; 3:1229–1233.
130. Whang D, Jin S, Wu Y, Lieber CM. Large-scale hierarchical organization of nanowire arrays for integrated nanosystems. *Nano Lett.* 2003; 3:1255–1259.
131. Acharya S, Panda AB, Belman N, Efrima S, Golan Y. A Semiconductor-Nanowire Assembly of Ultrahigh Junction Density by the Langmuir–Blodgett Technique. *Adv Mater.* 2006; 18:210–213.
132. Park J, Shin G, Ha JS. Controlling orientation of V<sub>2</sub>O<sub>5</sub> nanowires within micropatterns via microcontact printing combined with the gluing Langmuir–Blodgett technique. *Nanotechnology.* 2008; 19:395303. [PubMed: 21832592]
133. Liu JW, Zhu JH, Zhang CL, Liang HW, Yu SH. Mesostructured assemblies of ultrathin superlong tellurium nanowires and their photoconductivity. *J Am Chem Soc.* 2010; 132:8945–8952. [PubMed: 20545345]
134. Whang D, Jin S, Lieber CM. Nanolithography using hierarchically assembled nanowire masks. *Nano Lett.* 2003; 3:951–954.

135. Jin S, Whang D, McAlpine MC, Friedman RS, Wu Y, Lieber CM. Scalable interconnection and integration of nanowire devices without registration. *Nano Lett.* 2004; 4:915–919.
136. Yu G, Cao A, Lieber CM. Large-area blown bubble films of aligned nanowires and carbon nanotubes. *Nat Nanotechnol.* 2007; 2:372–377. [PubMed: 18654310]
137. Yu G, Li X, Lieber CM, Cao A. Nanomaterial-incorporated blown bubble films for large-area, aligned nanostructures. *J Mater Chem.* 2008; 18:728–734.
138. Myung S, Lee M, Kim GT, Ha JS, Hong S. Large-Scale “Surface-Programmed Assembly” of Pristine Vanadium Oxide Nanowire-Based Devices. *Adv Mater.* 2005; 17:2361–2364.
139. Kang J, Myung S, Kim B, Oh D, Kim GT, Hong S. Massive assembly of ZnO nanowire-based integrated devices. *Nanotechnology.* 2008; 19:095303. [PubMed: 21817667]
140. Lee M, Im J, Lee B, Myung S, Kang J, Huang L, Kwon YK, Hong S. Linker-free directed assembly of high-performance integrated devices based on nanotubes and nanowires. *Nat Nanotechnol.* 2006; 1:66–71. [PubMed: 18654144]
141. Salem AK, Chao J, Leong KW, Searson PC. Receptor-mediated self-assembly of multi-component magnetic nanowires. *Adv Mater.* 2004; 16:268–271.
142. Chen M, Searson PC. The Dynamics of Nanowire Self-Assembly. *Adv Mater.* 2005; 17:2765–2768.
143. Lee J, Wang AA, Rheem Y, Yoo B, Mulchandani A, Chen W, Myung NV. DNA assisted assembly of multisegmented nanowires. *Electroanal.* 2007; 19:2287–2293.
144. Shi HY, Hu B, Yu XC, Zhao RL, Ren XF, Liu SL, Liu JW, Feng M, Xu AW, Yu SH. Ordering of disordered nanowires: spontaneous formation of highly aligned, ultralong Ag nanowire films at oil–water–air interface. *Adv Funct Mater.* 2010; 20:958–964.
145. Liu JW, Zhang SY, Qi H, Wen WC, Yu SH. A General Strategy for Self-Assembly of Nanosized Building Blocks on Liquid/Liquid Interfaces. *Small.* 2012; 8:2412–2420. [PubMed: 22544810]
146. Duan X, Huang Y, Cui Y, Wang J, Lieber CM. Indium phosphide nanowires as building blocks for nanoscale electronic and optoelectronic devices. *Nature.* 2001; 409:66–69. [PubMed: 11343112]
147. Freer EM, Grachev O, Duan X, Martin S, Stumbo DP. High-yield self-limiting single-nanowire assembly with dielectrophoresis. *Nat Nanotechnol.* 2010; 5:525–530. [PubMed: 20526324]
148. Li M, Bhiladvala RB, Morrow TJ, Siooss JA, Lew KK, Redwing JM, Keating CD, Mayer TS. Bottom-up assembly of large-area nanowire resonator arrays. *Nat Nanotechnol.* 2008; 3:88–92. [PubMed: 18654467]
149. Tanase M, Bauer LA, Hultgren A, Silevitch DM, Sun L, Reich DH, Searson PC, Meyer GJ. Magnetic alignment of fluorescent nanowires. *Nano Lett.* 2001; 1:155–158.
150. Hangarter CM, Rheem Y, Yoo B, Yang EH, Myung NV. Hierarchical magnetic assembly of nanowires. *Nanotechnology.* 2007; 18:205305.
151. Liu M, Lagdani J, Imrane H, Pettiford C, Lou J, Yoon S, Harris VG, Vittoria C, Sun NX. Self-assembled magnetic nanowire arrays. *Appl Phys Lett.* 2007; 90:3105.
152. Hangarter CM, Myung NV. Magnetic alignment of nanowires. *Chem Mat.* 2005; 17:1320–1324.
153. Lee SW, Jeong MC, Myoung JM, Chae GS, Chung IJ. Magnetic alignment of ZnO nanowires for optoelectronic device applications. *Appl Phys Lett.* 2007; 90:3115.
154. Bangar MA, Hangarter CM, Yoo B, Rheem Y, Chen W, Mulchandani A, Myung NV. Magnetically Assembled Multisegmented Nanowires and Their Applications. *Electroanal.* 2009; 21:61–67.
155. Sun Y, Rogers JA. Fabricating semiconductor nano/microwires and transfer printing ordered arrays of them onto plastic substrates. *Nano Lett.* 2004; 4:1953–1959.
156. Sun Y, Kim S, Adesida I, Rogers JA. Bendable GaAs metal-semiconductor field-effect transistors formed with printed GaAs wire arrays on plastic substrates. *Appl Phys Lett.* 2005; 87:083501.
157. Ahn JH, Kim HS, Lee KJ, Jeon S, Kang SJ, Sun Y, Nuzzo RG, Rogers JA. Heterogeneous Three-Dimensional Electronics by Use of Printed Semiconductor Nanomaterials. *Science.* 2006; 314:1754–1757. [PubMed: 17170298]
158. McAlpine MC, Ahmad H, Wang D, Heath JR. Highly ordered nanowire arrays on plastic substrates for ultrasensitive flexible chemical sensors. *Nat Mater.* 2007; 6:379–384. [PubMed: 17450146]

159. Lee CH, Kim DR, Zheng X. Fabricating nanowire devices on diverse substrates by simple transfer-printing methods. *Proc Natl Acad Sci USA*. 2010; 107:9950–9955. [PubMed: 20479263]
160. Javey A, Nam S, Friedman RS, Yan H, Lieber CM. Layer-by-layer assembly of nanowires for three-dimensional, multifunctional electronics. *Nano Lett*. 2007; 7:773–777. [PubMed: 17266383]
161. Fan Z, Ho JC, Jacobson ZA, Yerushalmi R, Alley RL, Razavi H, Javey A. Wafer-scale assembly of highly ordered semiconductor nanowire arrays by contact printing. *Nano Lett*. 2008; 8:20–25. [PubMed: 17696563]
162. Takahashi T, Takei K, Ho JC, Chueh YL, Fan Z, Javey A. Monolayer resist for patterned contact printing of aligned nanowire arrays. *J Am Chem Soc*. 2009; 131:2102–2103. [PubMed: 19173560]
163. Zhu G, Yang R, Wang S, Wang ZL. Flexible high-output nanogenerator based on lateral ZnO nanowire array. *Nano Lett*. 2010; 10:3151–3155. [PubMed: 20698630]
164. Yerushalmi R, Jacobson ZA, Ho JC, Fan Z, Javey A. Large scale, highly ordered assembly of nanowire parallel arrays by differential roll printing. *Appl Phys Lett*. 2007; 91:203104.
165. Fan Z, Ho JC, Takahashi T, Yerushalmi R, Takei K, Ford AC, Chueh YL, Javey A. Toward the development of printable nanowire electronics and sensors. *Adv Mater*. 2009; 21:3730–3743.
166. Chang YK, Hong FCN. The Fabrication of ZnO Nanowire Field-Effect Transistors by Roll-Transfer Printing. *Nanotechnology*. 2009; 20:195302. [PubMed: 19420638]
167. Yao J, Yan H, Lieber CM. A nanoscale combing technique for the large-scale assembly of highly aligned nanowires. *Nat Nanotechnol*. 2013; 8:329–335. [PubMed: 23603986]
168. Pevzner A, Engel Y, Elnathan R, Ducobni T, Ben-Ishai M, Reddy K, Shpaisman N, Tsukernik A, Oksman M, Patolsky F. Knocking down highly-ordered large-scale nanowire arrays. *Nano Lett*. 2010; 10:1202–1208. [PubMed: 20199032]
169. Song H, Lee MH. Combing non-epitaxially grown nanowires for large-area electronic devices. *Nanotechnology*. 2013; 24:285302. [PubMed: 23787876]
170. Xu F, Durham JW III, Wiley BJ, Zhu Y. Strain-release assembly of nanowires on stretchable substrates. *ACS Nano*. 2011; 5:1556–1563. [PubMed: 21288046]
171. Li Y, Wu Y. Coassembly of graphene oxide and nanowires for large-area nanowire alignment. *J Am Chem Soc*. 2009; 131:5851–5857. [PubMed: 19348420]
172. Yang W, Qu L, Zheng R, Liu Z, Ratinac KR, Shen L, Yu D, Yang L, Barrow JC, Ringer SP. Self-assembly of gold nanowires along carbon nanotubes for ultrahigh-aspect-ratio hybrids. *Chem Mat*. 2011; 23:2760–2765.
173. Qing Q, Pal SK, Tian B, Duan X, Timko BP, Cohen-Karni T, Murthy VN, Lieber CM. Nanowire transistor arrays for mapping neural circuits in acute brain slices. *Proc Natl Acad Sci USA*. 2010; 107:1882–1887. [PubMed: 20133836]
174. Hong G, Fu TM, Zhou T, Schuhmann TG, Huang J, Lieber CM. Syringe Injectable Electronics: Precise Targeted Delivery with Quantitative Input/Output Connectivity. *Nano Lett*. 2015; 15:6979–6984. [PubMed: 26317328]
175. Huang Y, Duan X, Cui Y, Lieber CM. Gallium nitride nanowire nanodevices. *Nano Lett*. 2002; 2:101–104.
176. Duan X. Nanowire thin-film transistors: a new avenue to high-performance macroelectronics. *IEEE T Electron Dev*. 2008; 55:3056–3062.
177. Cui Y, Zhong Z, Wang D, Wang WU, Lieber CM. High Performance Silicon Nanowire Field Effect Transistors. *Nano Lett*. 2003; 3:149–152.
178. Duan X, Niu C, Sahi V, Chen J, Parce JW, Empedocles S, Goldman JL. High-performance thin-film transistors using semiconductor nanowires and nanoribbons. *Nature*. 2003; 425:274–278. [PubMed: 13679911]
179. Zheng G, Lu W, Jin S, Lieber CM. Synthesis and Fabrication of High-Performance n-Type Silicon Nanowire Transistors. *Adv Mater*. 2004; 16:1890–1893.
180. Koo SM, Li Q, Edelstein MD, Richter CA, Vogel EM. Enhanced channel modulation in dual-gated silicon nanowire transistors. *Nano Lett*. 2005; 5:2519–2523. [PubMed: 16351207]

181. Ho, T-t; Wang, Y.; Eichfeld, S.; Lew, KK.; Liu, B.; Mohny, SE.; Redwing, JM.; Mayer, TS. In situ axially doped n-channel silicon nanowire field-effect transistors. *Nano Lett.* 2008; 8:4359–4364. [PubMed: 19367848]
182. Lu W, Xiang J, Timko BP, Wu Y, Lieber CM. One-dimensional hole gas in germanium/silicon nanowire heterostructures. *Proc Natl Acad Sci USA.* 2005; 102:10046–10051. [PubMed: 16006507]
183. Xiang J, Lu W, Hu YJ, Wu Y, Yan H, Lieber CM. Ge/Si nanowire heterostructures as high-performance field-effect transistors. *Nature.* 2006; 441:489–493. [PubMed: 16724062]
184. Hu Y, Xiang J, Liang G, Yan H, Lieber CM. Sub-100 nanometer channel length Ge/Si nanowire transistors with potential for 2 THz switching speed. *Nano Lett.* 2008; 8:925–930. [PubMed: 18251518]
185. Dillen DC, Kim K, Liu ES, Tutuc E. Radial modulation doping in core-shell nanowires. *Nat Nanotechnol.* 2014; 9:116–120. [PubMed: 24441982]
186. Yu JY, Chung SW, Heath JR. Silicon nanowires: preparation, device fabrication, and transport properties. *J Phys Chem B.* 2000; 104:11864–11870.
187. Huang Y, Duan X, Cui Y, Lathon LJ, Kim KH, Lieber CM. Logic gates and computation from assembled nanowire building blocks. *Science.* 2001; 294:1313–1317. [PubMed: 11701922]
188. Nam S, Jiang X, Xiong Q, Ham D, Lieber CM. Vertically integrated, three-dimensional nanowire complementary metal-oxide-semiconductor circuits. *Proc Natl Acad Sci USA.* 2009; 106:21035–21038. [PubMed: 19940239]
189. Colinge JP, Lee CW, Afzalain A, Akhavan ND, Yan R, Ferain I, Razavi P, O'Neill B, Blake A, White M. Nanowire Transistors without Junctions. *Nat Nanotechnol.* 2010; 5:225–229. [PubMed: 20173755]
190. Ouyang M, Huang JL, Lieber CM. Fundamental electronic properties and applications of single-walled carbon nanotubes. *Acc Chem Res.* 2002; 35:1018–1025. [PubMed: 12484789]
191. McEuen PL, Park JY. Electron transport in single-walled carbon nanotubes. *MRS Bull.* 2004; 29:272–275.
192. Popov VN. Carbon nanotubes: properties and application. *Mater Sci Eng, R.* 2004; 43:61–102.
193. Thostenson ET, Ren Z, Chou TW. Advances in the science and technology of carbon nanotubes and their composites: a review. *Compos Sci Technol.* 2001; 61:1899–1912.
194. Avouris P. Molecular electronics with carbon nanotubes. *Acc Chem Res.* 2002; 35:1026–1034. [PubMed: 12484790]
195. Coleman JN, Khan U, Blau WJ, Gun'ko YK. Small but strong: a review of the mechanical properties of carbon nanotube-polymer composites. *Carbon.* 2006; 44:1624–1652.
196. Cao Q, Rogers JA. Ultrathin Films of Single-Walled Carbon Nanotubes for Electronics and Sensors: A Review of Fundamental and Applied Aspects. *Adv Mater.* 2009; 21:29–53.
197. Tan CW, Tan KH, Ong YT, Mohamed AR, Zein SHS, Tan SH. Energy and environmental applications of carbon nanotubes. *Environ Chem Lett.* 2012; 10:265–273.
198. De Volder MF, Tawfick SH, Baughman RH, Hart AJ. Carbon nanotubes: present and future commercial applications. *Science.* 2013; 339:535–539. [PubMed: 23372006]
199. Yang W, Thordarson P, Gooding JJ, Ringer SP, Braet F. Carbon nanotubes for biological and biomedical applications. *Nanotechnology.* 2007; 18
200. Saito N, Usui Y, Aoki K, Narita N, Shimizu M, Hara K, Ogiwara N, Nakamura K, Ishigaki N, Kato H, et al. Carbon nanotubes: biomaterial applications. *Chem Soc Rev.* 2009; 38:1897–1903. [PubMed: 19551170]
201. Liu Z, Tabakman S, Welsher K, Dai H. Carbon Nanotubes in Biology and Medicine: In vitro and in vivo Detection, Imaging and Drug Delivery. *Nano Res.* 2009; 2:85–120. [PubMed: 20174481]
202. Lu F, Gu L, Mezzani MJ, Wang X, Luo PG, Veca LM, Cao L, Sun YP. Advances in Bioapplications of Carbon Nanotubes. *Adv Mater.* 2009; 21:139–152.
203. Andrews R, Jacques D, Qian D, Rantell T. Multiwall carbon nanotubes: synthesis and application. *Acc Chem Res.* 2002; 35:1008–1017. [PubMed: 12484788]
204. Saito R, Fujita M, Dresselhaus G, Dresselhaus MS. Electronic structure of graphene tubules based on C 60. *Phys Rev B.* 1992; 46:1804.

205. Journet C, Picher M, Jourdain V. Carbon nanotube synthesis: from large-scale production to atom-by-atom growth. *Nanotechnology*. 2012; 23:142001. [PubMed: 22433510]
206. Chen Y, Zhang Y, Hu Y, Kang L, Zhang S, Xie H, Liu D, Zhao Q, Li Q, Zhang J. State of the Art of Single-Walled Carbon Nanotube Synthesis on Surfaces. *Adv Mater*. 2014; 26:5898–5922. [PubMed: 25042346]
207. Chen Y, Zhang J. Chemical Vapor Deposition Growth of Single-Walled Carbon Nanotubes with Controlled Structures for Nanodevice Applications. *Acc Chem Res*. 2014; 47:2273–2281. [PubMed: 24926610]
208. Meyyappan M. A review of plasma enhanced chemical vapour deposition of carbon nanotubes. *J Phys D: Appl Phys*. 2009; 42:213001.
209. Iijima S. Helical microtubules of graphitic carbon. *Nature*. 1991; 354:56–58.
210. Iijima S, Ichihashi T. Single-shell carbon nanotubes of 1-nm diameter. *Nature*. 1993; 363:603–605.
211. Bethune D, Klang C, De Vries M, Gorman G, Savoy R, Vazquez J, Beyers R. Cobalt-Catalysed Growth of Carbon Nanotubes with Single-Atomic-Layer Walls. *Nature*. 1993; 363:605–607.
212. Journet C, Maser W, Bernier P, Loiseau A, Lamy de la Chapelle M, Lefrant S, Deniard P, Lee R, Fischer J. Large-scale production of single-walled carbon nanotubes by the electric-arc technique. *Nature*. 1997; 388:756–758.
213. Poretzky AA, Schittenhelm H, Fan X, Lance MJ, Allard LF Jr, Geohegan DB. Investigations of single-wall carbon nanotube growth by time-restricted laser vaporization. *Phys Rev B*. 2002; 65:245425.
214. Poretzky A, Geohegan D, Fan X, Pennycook S. In situ imaging and spectroscopy of single-wall carbon nanotube synthesis by laser vaporization. *Appl Phys Lett*. 2000; 76:182–184.
215. Poretzky A, Geohegan D, Fan X, Pennycook S. Dynamics of single-wall carbon nanotube synthesis by laser vaporization. *Appl Phys A*. 2000; 70:153–160.
216. Jose-Yacaman M, Miki-Yoshida M, Rendon L, Santiesteban J. Catalytic growth of carbon microtubules with fullerene structure. *Appl Phys Lett*. 1993; 62:202–204.
217. Nikolaev P, Bronikowski MJ, Bradley RK, Rohmund F, Colbert DT, Smith K, Smalley RE. Gas-phase catalytic growth of single-walled carbon nanotubes from carbon monoxide. *Chem Phys Lett*. 1999; 313:91–97.
218. Takagi D, Homma Y, Hibino H, Suzuki S, Kobayashi Y. Single-walled carbon nanotube growth from highly activated metal nanoparticles. *Nano Lett*. 2006; 6:2642–2645. [PubMed: 17163681]
219. Huang S, Cai Q, Chen J, Qian Y, Zhang L. Metal-catalyst-free growth of single-walled carbon nanotubes on substrates. *J Am Chem Soc*. 2009; 131:2094–2095. [PubMed: 19159295]
220. Liu B, Ren W, Gao L, Li S, Pei S, Liu C, Jiang C, Cheng HM. Metal-catalyst-free growth of single-walled carbon nanotubes. *J Am Chem Soc*. 2009; 131:2082–2083. [PubMed: 19170494]
221. Cheung CL, Kurtz A, Park H, Lieber CM. Diameter-Controlled Synthesis of Carbon Nanotubes. *J Phys Chem B*. 2002; 106:2429–2433.
222. Hata K, Futaba DN, Mizuno K, Namai T, Yumura M, Iijima S. Water-assisted highly efficient synthesis of impurity-free single-walled carbon nanotubes. *Science*. 2004; 306:1362–1364. [PubMed: 15550668]
223. Wang X, Li Q, Xie J, Jin Z, Wang J, Li Y, Jiang K, Fan S. Fabrication of ultralong and electrically uniform single-walled carbon nanotubes on clean substrates. *Nano Lett*. 2009; 9:3137–3141. [PubMed: 19650638]
224. Hofmann S, Ducati C, Robertson J, Kleinsorge B. Low-temperature growth of carbon nanotubes by plasma-enhanced chemical vapor deposition. *Appl Phys Lett*. 2003; 83:135–137.
225. Rao C, Voggu R, Govindaraj A. Selective generation of single-walled carbon nanotubes with metallic, semiconducting and other unique electronic properties. *Nanoscale*. 2009; 1:96–105. [PubMed: 20644865]
226. Zhang Y, Zheng L. Towards chirality-pure carbon nanotubes. *Nanoscale*. 2010; 2:1919–1929. [PubMed: 20835436]

227. Ding L, Tselev A, Wang J, Yuan D, Chu H, McNicholas TP, Li Y, Liu J. Selective growth of well-aligned semiconducting single-walled carbon nanotubes. *Nano Lett.* 2009; 9:800–805. [PubMed: 19159186]
228. Lu J, Lai L, Luo G, Zhou J, Qin R, Wang D, Wang L, Mei WN, Li G, Gao Z. Why Semiconducting Single-Walled Carbon Nanotubes are Separated from their Metallic Counterparts. *Small.* 2007; 3:1566–1576. [PubMed: 17705313]
229. Zhou W, Zhan S, Ding L, Liu J. General rules for selective growth of enriched semiconducting single walled carbon nanotubes with water vapor as in situ etchant. *J Am Chem Soc.* 2012; 134:14019–14026. [PubMed: 22873685]
230. Li J, Liu K, Liang S, Zhou W, Pierce M, Wang F, Peng L, Liu J. Growth of high-density-aligned and semiconducting-enriched single-walled carbon nanotubes: Decoupling the conflict between density and selectivity. *ACS Nano.* 2014; 8:554–562. [PubMed: 24295396]
231. Hong G, Zhang B, Peng B, Zhang J, Choi WM, Choi JY, Kim JM, Liu Z. Direct growth of semiconducting single-walled carbon nanotube array. *J Am Chem Soc.* 2009; 131:14642–14643. [PubMed: 19778018]
232. Peng B, Jiang S, Zhang Y, Zhang J. Enrichment of metallic carbon nanotubes by electric field-assisted chemical vapor deposition. *Carbon.* 2011; 49:2555–2560.
233. Collins PG, Arnold MS, Avouris P. Engineering Carbon Nanotubes and Nanotube Circuits Using Electrical Breakdown. *Science.* 2001; 292:706–709. [PubMed: 11326094]
234. Jin SH, Dunham SN, Song J, Xie X, Kim J-h, Lu C, Islam A, Du F, Kim J, Felts J. Using nanoscale thermocapillary flows to create arrays of purely semiconducting single-walled carbon nanotubes. *Nat Nanotechnol.* 2013; 8:347–355. [PubMed: 23624697]
235. Seo K, Kim C, Choi YS, Park KA, Lee YH, Kim B. Tuning chirality of single-wall carbon nanotubes by selective etching with carbon dioxide. *J Am Chem Soc.* 2003; 125:13946–13947. [PubMed: 14611216]
236. Zhang G, Qi P, Wang X, Lu Y, Li X, Tu R, Bangsaruntip S, Mann D, Zhang L, Dai H. Selective etching of metallic carbon nanotubes by gas-phase reaction. *Science.* 2006; 314:974–977. [PubMed: 17095698]
237. Zhang H, Liu Y, Cao L, Wei D, Wang Y, Kajiura H, Li Y, Noda K, Luo G, Wang L. A Facile, Low-Cost, and Scalable Method of Selective Etching of Semiconducting Single-Walled Carbon Nanotubes by a Gas Reaction. *Adv Mater.* 2009; 21:813–816.
238. Maehashi K, Ohno Y, Inoue K, Matsumoto K. Chirality selection of single-walled carbon nanotubes by laser resonance chirality selection method. *Appl Phys Lett.* 2004; 85:858–860.
239. Song J, Seo H, Park J, Kim J, Choi D, Han C. Selective removal of metallic SWNTs using microwave radiation. *Curr Appl Phys.* 2008; 8:725–728.
240. Zhang Y, Zhang Y, Xian X, Zhang J, Liu Z. Sorting out semiconducting single-walled carbon nanotube arrays by preferential destruction of metallic tubes using xenon-lamp irradiation. *J Phys Chem C.* 2008; 112:3849–3856.
241. Hu Y, Chen Y, Li P, Zhang J. Sorting out Semiconducting Single-Walled Carbon Nanotube Arrays by Washing off Metallic Tubes Using SDS Aqueous Solution. *Small.* 2013; 9:1306–1311. [PubMed: 23505123]
242. Hersam MC. Progress towards monodisperse single-walled carbon nanotubes. *Nat Nanotechnol.* 2008; 3:387–394. [PubMed: 18654561]
243. Bandow S, Asaka S, Saito Y, Rao A, Grigorian L, Richter E, Eklund P. Effect of the Growth Temperature on the Diameter Distribution and Chirality of Single-Wall Carbon Nanotubes. *Phys Rev Lett.* 1998; 80:3779.
244. Rao R, Liptak D, Cherukuri T, Yakobson BI, Maruyama B. In situ evidence for chirality-dependent growth rates of individual carbon nanotubes. *Nat Mater.* 2012; 11:213–216. [PubMed: 22286334]
245. Bachilo SM, Balzano L, Herrera JE, Pompeo F, Resasco DE, Weisman RB. Narrow (n, m)-Distribution of Single-Walled Carbon Nanotubes Grown using a Solid Supported Catalyst. *J Am Chem Soc.* 2003; 125:11186–11187. [PubMed: 16220926]

246. Chiang WH, Sankaran RM. Linking Catalyst Composition to Chirality Distributions of As-Grown Single-Walled Carbon Nanotubes by Tuning NixFe1-x Nanoparticles. *Nat Mater.* 2009; 8:882–886. [PubMed: 19767738]
247. He M, Jiang H, Kauppinen EI, Lehtonen J. Diameter and chiral angle distribution dependencies on the carbon precursors in surface-grown single-walled carbon nanotubes. *Nanoscale.* 2012; 4:7394–7398. [PubMed: 23085735]
248. Yang F, Wang X, Zhang D, Yang J, Luo D, Xu Z, Wei J, Wang JQ, Xu Z, Peng F. Chirality-specific growth of single-walled carbon nanotubes on solid alloy catalysts. *Nature.* 2014; 510:522–524. [PubMed: 24965654]
249. Yu X, Zhang J, Choi W, Choi JY, Kim JM, Gan L, Liu Z. Cap formation engineering: from opened C60 to single-walled carbon nanotubes. *Nano Lett.* 2010; 10:3343–3349. [PubMed: 20681626]
250. Smalley RE, Li Y, Moore VC, Price BK, Colorado R, Schmidt HK, Hauge RH, Barron AR, Tour JM. Single wall carbon nanotube amplification: En route to a type-specific growth mechanism. *J Am Chem Soc.* 2006; 128:15824–15829. [PubMed: 17147393]
251. Yao Y, Feng C, Zhang J, Liu Z. “Cloning” of single-walled carbon nanotubes via open-end growth mechanism. *Nano Lett.* 2009; 9:1673–1677. [PubMed: 19284730]
252. Liu J, Wang C, Tu X, Liu B, Chen L, Zheng M, Zhou C. Chirality-controlled synthesis of single-wall carbon nanotubes using vapour-phase epitaxy. *Nat Commun.* 2012; 3:1199.
253. Sanchez-Valencia JR, Dienel T, Gröning O, Shorubalko I, Mueller A, Jansen M, Amsharov K, Ruffieux P, Fasel R. Controlled synthesis of single-chirality carbon nanotubes. *Nature.* 2014; 512:61–64. [PubMed: 25100481]
254. Druzhinina T, Hoepfener S, Schubert US. Strategies for Post-Synthesis Alignment and Immobilization of Carbon Nanotubes. *Adv Mater.* 2011; 23:953–970. [PubMed: 21181769]
255. Wang C, Takei K, Takahashi T, Javey A. Carbon nanotube electronics—moving forward. *Chem Soc Rev.* 2013; 42:2592–2609. [PubMed: 23229523]
256. Ma Y, Wang B, Wu Y, Huang Y, Chen Y. The production of horizontally aligned single-walled carbon nanotubes. *Carbon.* 2011; 49:4098–4110.
257. Liu Z, Jiao L, Yao Y, Xian X, Zhang J. Aligned, Ultralong Single-Walled Carbon Nanotubes: From Synthesis, Sorting, to Electronic Devices. *Adv Mater.* 2010; 22:2285–2310. [PubMed: 20358529]
258. Ibrahim I, Bachmatiuk A, Warner JH, Büchner B, Cuniberti G, Rummeli MH. CVD-Grown Horizontally Aligned Single-Walled Carbon Nanotubes: Synthesis Routes and Growth Mechanisms. *Small.* 2012; 8:1973–1992. [PubMed: 22619167]
259. Hedberg J, Dong L, Jiao J. Air flow technique for large scale dispersion and alignment of carbon nanotubes on various substrates. *Appl Phys Lett.* 2005; 86:143111.
260. Vichchulada P, Zhang Q, Duncan A, Lay MD. Macroscopic electrical properties of ordered single-walled carbon nanotube networks. *ACS Appl Mater Interfaces.* 2010; 2:467–473. [PubMed: 20356193]
261. Kim P, Baik S, Suh KY. Capillarity-Driven Fluidic Alignment of Single-Walled Carbon Nanotubes in Reversibly Bonded Nanochannels. *Small.* 2008; 4:92–95. [PubMed: 18098240]
262. Zhang S, Li Q, Kinloch IA, Windle AH. Ordering in a droplet of an aqueous suspension of single-wall carbon nanotubes on a solid substrate. *Langmuir.* 2009; 26:2107–2112.
263. Ko H, Peleshanko S, Tsukruk VV. Combing and bending of carbon nanotube arrays with confined microfluidic flow on patterned surfaces. *J Phys Chem B.* 2004; 108:4385–4393.
264. Ko H, Tsukruk VV. Liquid-crystalline processing of highly oriented carbon nanotube arrays for thin-film transistors. *Nano Lett.* 2006; 6:1443–1448. [PubMed: 16834426]
265. Engel M, Small JP, Steiner M, Freitag M, Green AA, Hersam MC, Avouris P. Thin film nanotube transistors based on self-assembled, aligned, semiconducting carbon nanotube arrays. *ACS Nano.* 2008; 2:2445–2452. [PubMed: 19206278]
266. Li X, Zhang L, Wang X, Shimoyama I, Sun X, Seo WS, Dai H. Langmuir-Blodgett assembly of densely aligned single-walled carbon nanotubes from bulk materials. *J Am Chem Soc.* 2007; 129:4890–4891. [PubMed: 17394327]

267. Choi SW, Kang WS, Lee JH, Najeeb CK, Chun HS, Kim JH. Patterning of Hierarchically Aligned Single-Walled Carbon Nanotube Langmuir–Blodgett Films by Microcontact Printing. *Langmuir*. 2010; 26:15680–15685. [PubMed: 20825154]
268. Chen X, Saito T, Yamada H, Matsushige K. Aligning Single-Wall Carbon Nanotubes with an Alternating-Current Electric Field. *Appl Phys Lett*. 2001; 78:3714–3716.
269. Kamat PV, Thomas KG, Barazzouk S, Girishkumar G, Vinodgopal K, Meisel D. Self-assembled linear bundles of single wall carbon nanotubes and their alignment and deposition as a film in a dc field. *J Am Chem Soc*. 2004; 126:10757–10762. [PubMed: 15327336]
270. Zhu YF, Ma C, Zhang W, Zhang RP, Koratkar N, Liang J. Alignment of multiwalled carbon nanotubes in bulk epoxy composites via electric field. *J Appl Phys*. 2009; 105:054319.
271. Walters D, Casavant M, Qin X, Huffman C, Boul P, Ericson L, Haroz E, O'connell M, Smith K, Colbert D. In-plane-aligned membranes of carbon nanotubes. *Chem Phys Lett*. 2001; 338:14–20.
272. Choi E, Brooks J, Eaton D, Al-Haik M, Hussaini M, Garmestani H, Li D, Dahmen K. Enhancement of Thermal and Electrical Properties of Carbon Nanotube Polymer Composites by Magnetic Field Processing. *J Appl Phys*. 2003; 94:6034–6039.
273. Kimura T, Ago H, Tobita M, Ohshima S, Kyotani M, Yumura M. Polymer composites of carbon nanotubes aligned by a magnetic field. *Adv Mater*. 2002; 14:1380–1383.
274. Correa-Duarte MA, Grzelczak M, Salgueirino-Maceira V, Giersig M, Liz-Marzan LM, Farle M, Sieradzki K, Diaz R. Alignment of Carbon Nanotubes under Low Magnetic Fields through Attachment of Magnetic Nanoparticles. *J Phys Chem B*. 2005; 109:19060–19063. [PubMed: 16853457]
275. Camponeschi E, Florkowski B, Vance R, Garrett G, Garmestani H, Tannenbaum R. Uniform Directional Alignment of Single-Walled Carbon Nanotubes in Viscous Polymer Flow. *Langmuir*. 2006; 22:1858–1862. [PubMed: 16460118]
276. Zamora-Ledezma C, Blanc C, Maugey M, Zakri C, Poulin P, Anglaret E. Anisotropic thin films of single-wall carbon nanotubes from aligned lyotropic nematic suspensions. *Nano Lett*. 2008; 8:4103–4107. [PubMed: 19367925]
277. Lu L, Chen W. Large-scale aligned carbon nanotubes from their purified, highly concentrated suspension. *ACS Nano*. 2010; 4:1042–1048. [PubMed: 20088601]
278. LeMieux MC, Roberts M, Barman S, Jin YW, Kim JM, Bao Z. Self-sorted, aligned nanotube networks for thin-film transistors. *Science*. 2008; 321:101–104. [PubMed: 18599781]
279. LeMieux MC, Sok S, Roberts ME, Opatkiewicz JP, Liu D, Barman SN, Patil N, Mitra S, Bao Z. Solution assembly of organized carbon nanotube networks for thin-film transistors. *ACS Nano*. 2009; 3:4089–4097. [PubMed: 19924882]
280. Liu H, Takagi D, Chiashi S, Homma Y. Transfer and alignment of random single-walled carbon nanotube films by contact printing. *ACS Nano*. 2010; 4:933–938. [PubMed: 20104866]
281. Tang G, Zhang X, Yang S, Derycke V, Benattar JJ. New Confinement Method for the Formation of Highly Aligned and Densely Packed Single-Walled Carbon Nanotube Monolayers. *Small*. 2010; 6:1488–1491. [PubMed: 20578113]
282. Huang S, Woodson M, Smalley R, Liu J. Growth mechanism of oriented long single walled carbon nanotubes using “fast-heating” chemical vapor deposition process. *Nano Lett*. 2004; 4:1025–1028.
283. Huang S, Maynor B, Cai X, Liu J. Ultralong, well-aligned single-walled carbon nanotube architectures on surfaces. *Adv Mater*. 2003; 15:1651–1655.
284. Huang S, Cai X, Liu J. Growth of millimeter-long and horizontally aligned single-walled carbon nanotubes on flat substrates. *J Am Chem Soc*. 2003; 125:5636–5637. [PubMed: 12733894]
285. Huang S, Cai X, Du C, Liu J. Oriented long single walled carbon nanotubes on substrates from floating catalysts. *J Phys Chem B*. 2003; 107:13251–13254.
286. Huang L, Cui X, White B, O'Brien SP. Long and oriented single-walled carbon nanotubes grown by ethanol chemical vapor deposition. *J Phys Chem B*. 2004; 108:16451–16456.
287. Hofmann M, Nezhich D, Kong J. In-situ sample rotation as a tool to understand chemical vapor deposition growth of long aligned carbon nanotubes. *Nano Lett*. 2008; 8:4122–4127. [PubMed: 19367958]

288. Hong BH, Lee JY, Beetz T, Zhu Y, Kim P, Kim KS. Quasi-continuous growth of ultralong carbon nanotube arrays. *J Am Chem Soc.* 2005; 127:15336–15337. [PubMed: 16262374]
289. Zheng L, O'connell M, Doorn S, Liao X, Zhao Y, Akhadov E, Hoffbauer M, Roop B, Jia Q, Dye R. Ultralong single-wall carbon nanotubes. *Nat Mater.* 2004; 3:673–676. [PubMed: 15359345]
290. Wen Q, Zhang R, Qian W, Wang Y, Tan P, Nie J, Wei F. Growing 20 cm long DWNTs/TWNTs at a rapid growth rate of 80–90  $\mu\text{m/s}$ . *Chem Mat.* 2010; 22:1294–1296.
291. Zhang Y, Chang A, Cao J, Wang Q, Kim W, Li Y, Morris N, Yenilmez E, Kong J, Dai H. Electric-field-directed growth of aligned single-walled carbon nanotubes. *Appl Phys Lett.* 2001; 79:3155–3157.
292. Wang B, Ma Y, Li N, Wu Y, Li F, Chen Y. Facile and Scalable Fabrication of Well-Aligned and Closely Packed Single-Walled Carbon Nanotube Films on Various Substrates. *Adv Mater.* 2010; 22:3067–3070. [PubMed: 20432225]
293. Han S, Liu X, Zhou C. Template-free directional growth of single-walled carbon nanotubes on a- and r-plane sapphire. *J Am Chem Soc.* 2005; 127:5294–5295. [PubMed: 15826147]
294. Ago H, Nakamura K, Ikeda K-i, Uehara N, Ishigami N, Tsuji M. Aligned Growth of Isolated Single-Walled Carbon Nanotubes Programmed by Atomic Arrangement of Substrate Surface. *Chem Phys Lett.* 2005; 408:433–438.
295. Ismach A, Kantorovich D, Joselevich E. Carbon nanotube graphoepitaxy: Highly oriented growth by faceted nanosteps. *J Am Chem Soc.* 2005; 127:11554–11555. [PubMed: 16104703]
296. Ishigami N, Ago H, Imamoto K, Tsuji M, Iakoubovskii K, Minami N. Crystal plane dependent growth of aligned single-walled carbon nanotubes on sapphire. *J Am Chem Soc.* 2008; 130:9918–9924. [PubMed: 18597459]
297. Joselevich E. Self-organized growth of complex nanotube patterns on crystal surfaces. *Nano Res.* 2009; 2:743–754.
298. Tans SJ, Verschueren AR, Dekker C. Room-temperature transistor based on a single carbon nanotube. *Nature.* 1998; 393:49–52.
299. Javey A, Guo J, Wang Q, Lundstrom M, Dai H. Ballistic carbon nanotube field-effect transistors. *Nature.* 2003; 424:654–657. [PubMed: 12904787]
300. Dürkop T, Getty S, Cobas E, Fuhrer M. Extraordinary mobility in semiconducting carbon nanotubes. *Nano Lett.* 2004; 4:35–39.
301. Zhou X, Park JY, Huang S, Liu J, McEuen PL. Band structure, phonon scattering, and the performance limit of single-walled carbon nanotube transistors. *Phys Rev Lett.* 2005; 95:146805. [PubMed: 16241684]
302. Radosavljevic M, Appenzeller J, Avouris P, Knoch J. High performance of potassium n-doped carbon nanotube field-effect transistors. *Appl Phys Lett.* 2004; 84:3693–3695.
303. Derycke V, Martel R, Appenzeller J, Avouris P. Carbon nanotube inter-and intramolecular logic gates. *Nano Lett.* 2001; 1:453–456.
304. Liu X, Lee C, Zhou C, Han J. Carbon nanotube field-effect inverters. *Appl Phys Lett.* 2001; 79:3329–3331.
305. Shim M, Javey A, Shi Kam NW, Dai H. Polymer functionalization for air-stable n-type carbon nanotube field-effect transistors. *J Am Chem Soc.* 2001; 123:11512–11513. [PubMed: 11707143]
306. Klinke C, Chen J, Afzali A, Avouris P. Charge transfer induced polarity switching in carbon nanotube transistors. *Nano Lett.* 2005; 5:555–558. [PubMed: 15755113]
307. Javey A, Kim H, Brink M, Wang Q, Ural A, Guo J, McIntyre P, McEuen P, Lundstrom M, Dai H. High- $\kappa$  dielectrics for advanced carbon-nanotube transistors and logic gates. *Nat Mater.* 2002; 1:241–246. [PubMed: 12618786]
308. Zhang Z, Liang X, Wang S, Yao K, Hu Y, Zhu Y, Chen Q, Zhou W, Li Y, Yao Y. Doping-free fabrication of carbon nanotube based ballistic CMOS devices and circuits. *Nano Lett.* 2007; 7:3603–3607.
309. Ding L, Wang S, Zhang Z, Zeng Q, Wang Z, Pei T, Yang L, Liang X, Shen J, Chen Q. Y-contacted high-performance n-type single-walled carbon nanotube field-effect transistors: scaling and comparison with Sc-contacted devices. *Nano Lett.* 2009; 9:4209–4214. [PubMed: 19995085]

310. Wang C, Ryu K, Badmaev A, Zhang J, Zhou C. Metal contact engineering and registration-free fabrication of complementary metal-oxide semiconductor integrated circuits using aligned carbon nanotubes. *ACS Nano*. 2011; 5:1147–1153. [PubMed: 21271709]
311. Martel R, Schmidt T, Shea H, Hertel T, Avouris P. Single- and multi-wall carbon nanotube field-effect transistors. *Appl Phys Lett*. 1998; 73:2447–2449.
312. Zhang Z, Wang S, Ding L, Liang X, Pei T, Shen J, Xu H, Chen Q, Cui R, Li Y. Self-aligned ballistic n-type single-walled carbon nanotube field-effect transistors with adjustable threshold voltage. *Nano Lett*. 2008; 8:3696–3701. [PubMed: 18947214]
313. Nosho Y, Ohno Y, Kishimoto S, Mizutani T. n-type carbon nanotube field-effect transistors fabricated by using Ca contact electrodes. *Appl Phys Lett*. 2005; 86:073105.
314. Wind S, Appenzeller J, Martel R, Derycke V, Avouris P. Vertical scaling of carbon nanotube field-effect transistors using top gate electrodes. *Appl Phys Lett*. 2002; 80:3817–3819.
315. Ambrosi A, Chua CK, Bonanni A, Pumera M. Electrochemistry of Graphene and Related Materials. *Chem Rev*. 2014; 114:7150–7188. [PubMed: 24895834]
316. Guo S, Dong S. Graphene nanosheet: synthesis, molecular engineering, thin film, hybrids, and energy and analytical applications. *Chem Soc Rev*. 2011; 40:2644–2672. [PubMed: 21283849]
317. Chen D, Tang L, Li J. Graphene-Based Materials in Electrochemistry. *Chem Soc Rev*. 2010; 39:3157–3180. [PubMed: 20589275]
318. Novoselov KS, Geim AK, Morozov S, Jiang D, Zhang Y, Dubonos Sa, Grigorieva I, Firsov A. Electric field effect in atomically thin carbon films. *Science*. 2004; 306:666–669. [PubMed: 15499015]
319. Novoselov K, Jiang D, Schedin F, Booth T, Khotkevich V, Morozov S, Geim A. Two-dimensional atomic crystals. *Proc Natl Acad Sci USA*. 2005; 102:10451–10453. [PubMed: 16027370]
320. Wu J, Pisula W, Müllen K. Graphenes as potential material for electronics. *Chem Rev*. 2007; 107:718–747. [PubMed: 17291049]
321. Guinea F, Katsnelson M, Geim A. Energy gaps and a zero-field quantum Hall effect in graphene by strain engineering. *Nat Phys*. 2010; 6:30–33.
322. Coleman JN. Liquid Exfoliation of Defect-Free Graphene. *Acc Chem Res*. 2013; 46:14–22. [PubMed: 22433117]
323. Ciesielski A, Samorì P. Graphene via Sonication Assisted Liquid-Phase Exfoliation. *Chem Soc Rev*. 2014; 43:381–398. [PubMed: 24002478]
324. Hernandez Y, Nicolosi V, Lotya M, Blighe FM, Sun Z, De S, McGovern I, Holland B, Byrne M, Gun'ko YK. High-yield production of graphene by liquid-phase exfoliation of graphite. *Nat Nanotechnol*. 2008; 3:563–568. [PubMed: 18772919]
325. Blake P, Brimicombe PD, Nair RR, Booth TJ, Jiang D, Schedin F, Ponomarenko LA, Morozov SV, Gleeson HF, Hill EW. Graphene-Based Liquid Crystal Device. *Nano Lett*. 2008; 8:1704–1708. [PubMed: 18444691]
326. Bourlinos AB, Georgakilas V, Zboril R, Steriotis TA, Stubos AK. Liquid-Phase Exfoliation of Graphite Towards Solubilized Graphenes. *Small*. 2009; 5:1841–1845. [PubMed: 19408256]
327. Qian W, Hao R, Hou Y, Tian Y, Shen C, Gao H, Liang X. Solvothermal-assisted exfoliation process to produce graphene with high yield and high quality. *Nano Res*. 2009; 2:706–712.
328. Lotya M, Hernandez Y, King PJ, Smith RJ, Nicolosi V, Karlsson LS, Blighe FM, De S, Wang Z, McGovern I. Liquid phase production of graphene by exfoliation of graphite in surfactant/water solutions. *J Am Chem Soc*. 2009; 131:3611–3620. [PubMed: 19227978]
329. Englert JM, Röhr J, Schmidt CD, Graupner R, Hundhausen M, Hauke F, Hirsch A. Soluble graphene: generation of aqueous graphene solutions aided by a perylenebisimide-based bolaamphiphile. *Adv Mater*. 2009; 21:4265–4269.
330. Ghosh A, Rao KV, George SJ, Rao C. Noncovalent functionalization, exfoliation, and solubilization of graphene in water by employing a fluorescent coronene carboxylate. *Chem-Eur J*. 2010; 16:2700–2704. [PubMed: 20108284]
331. Lotya M, King PJ, Khan U, De S, Coleman JN. High-concentration, surfactant-stabilized graphene dispersions. *ACS Nano*. 2010; 4:3155–3162. [PubMed: 20455583]

332. Parviz D, Das S, Ahmed HT, Irin F, Bhattacharia S, Green MJ. Dispersions of non-covalently functionalized graphene with minimal stabilizer. *ACS Nano*. 2012; 6:8857–8867. [PubMed: 23002781]
333. Li X, Zhang G, Bai X, Sun X, Wang X, Wang E, Dai H. Highly conducting graphene sheets and Langmuir–Blodgett films. *Nat Nanotechnol*. 2008; 3:538–542. [PubMed: 18772914]
334. Vadukumpully S, Paul J, Valiyaveetil S. Cationic surfactant mediated exfoliation of graphite into graphene flakes. *Carbon*. 2009; 47:3288–3294.
335. Skaltsas T, Karousis N, Yan HJ, Wang CR, Pispas S, Tagmatarchis N. Graphene exfoliation in organic solvents and switching solubility in aqueous media with the aid of amphiphilic block copolymers. *J Mater Chem*. 2012; 22:21507–21512.
336. Liang YT, Hersam MC. Highly concentrated graphene solutions via polymer enhanced solvent exfoliation and iterative solvent exchange. *J Am Chem Soc*. 2010; 132:17661–17663. [PubMed: 21114312]
337. May P, Khan U, Hughes JM, Coleman JN. Role of solubility parameters in understanding the steric stabilization of exfoliated two-dimensional nanosheets by adsorbed polymers. *J Phys Chem C*. 2012; 116:11393–11400.
338. Brodie BC. On the Atomic Weight of Graphite. *Philos Trans R Soc Lond*. 1859:249–259.
339. Staudenmaier L. Method for the preparation of graphitic acid. *Ber Dtsch Chem Ges*. 1898; 31:1481–1487.
340. Hummers WS Jr, Offeman RE. Preparation of graphitic oxide. *J Am Chem Soc*. 1958; 80:1339–1339.
341. Marcano DC, Kosynkin DV, Berlin JM, Sinitskii A, Sun Z, Slesarev A, Alemany LB, Lu W, Tour JM. Improved synthesis of graphene oxide. *ACS Nano*. 2010; 4:4806–4814. [PubMed: 20731455]
342. Si Y, Samulski ET. Synthesis of water soluble graphene. *Nano Lett*. 2008; 8:1679–1682. [PubMed: 18498200]
343. Park S, An J, Jung I, Piner RD, An SJ, Li X, Velamakanni A, Ruoff RS. Colloidal suspensions of highly reduced graphene oxide in a wide variety of organic solvents. *Nano Lett*. 2009; 9:1593–1597. [PubMed: 19265429]
344. Wang G, Yang J, Park J, Gou X, Wang B, Liu H, Yao J. Facile synthesis and characterization of graphene nanosheets. *J Phys Chem C*. 2008; 112:8192–8195.
345. Li D, Mueller MB, Gilje S, Kaner RB, Wallace GG. Processable aqueous dispersions of graphene nanosheets. *Nat Nanotechnol*. 2008; 3:101–105. [PubMed: 18654470]
346. Tung VC, Allen MJ, Yang Y, Kaner RB. High-throughput solution processing of large-scale graphene. *Nat Nanotechnol*. 2009; 4:25–29. [PubMed: 19119278]
347. Rafiee MA, Rafiee J, Wang Z, Song H, Yu ZZ, Koratkar N. Enhanced mechanical properties of nanocomposites at low graphene content. *ACS Nano*. 2009; 3:3884–3890. [PubMed: 19957928]
348. Fan X, Peng W, Li Y, Li X, Wang S, Zhang G, Zhang F. Deoxygenation of exfoliated graphite oxide under alkaline conditions: a green route to graphene preparation. *Adv Mater*. 2008; 20:4490–4493.
349. Chen W, Yan L, Bangal PR. Preparation of Graphene by the Rapid and Mild Thermal Reduction of Graphene Oxide Induced by Microwaves. *Carbon*. 2010; 48:1146–1152.
350. Shao Y, Wang J, Engelhard M, Wang C, Lin Y. Facile and controllable electrochemical reduction of graphene oxide and its applications. *J Mater Chem*. 2010; 20:743–748.
351. Guo HL, Wang XF, Qian QY, Wang FB, Xia XH. A green approach to the synthesis of graphene nanosheets. *ACS Nano*. 2009; 3:2653–2659. [PubMed: 19691285]
352. Mattevi C, Kim H, Chhowalla M. A review of chemical vapour deposition of graphene on copper. *J Mater Chem*. 2011; 21:3324–3334.
353. Yan K, Fu L, Peng H, Liu Z. Designed CVD growth of graphene via process engineering. *Acc Chem Res*. 2013; 46:2263–2274. [PubMed: 23869401]
354. Zhang Y, Zhang L, Zhou C. Review of chemical vapor deposition of graphene and related applications. *Acc Chem Res*. 2013; 46:2329–2339. [PubMed: 23480816]

355. Yu Q, Lian J, Siriponglert S, Li H, Chen YP, Pei SS. Graphene segregated on Ni surfaces and transferred to insulators. *Appl Phys Lett*. 2008; 93:113103.
356. Arco D, Gomez L, Zhang Y, Kumar A, Zhou C. Synthesis, Transfer, and Devices of Single- and Few-Layer Graphene by Chemical Vapor Deposition. *IEEE T Nanotechnol*. 2009; 8:135–138.
357. Reina A, Jia X, Ho J, Nezich D, Son H, Bulovic V, Dresselhaus MS, Kong J. Large area, few-layer graphene films on arbitrary substrates by chemical vapor deposition. *Nano Lett*. 2008; 9:30–35. [PubMed: 19046078]
358. Kim KS, Zhao Y, Jang H, Lee SY, Kim JM, Kim KS, Ahn JH, Kim P, Choi JY, Hong BH. Large-scale pattern growth of graphene films for stretchable transparent electrodes. *Nature*. 2009; 457:706–710. [PubMed: 19145232]
359. Li X, Cai W, An J, Kim S, Nah J, Yang D, Piner R, Velamakanni A, Jung I, Tutuc E. Large-area synthesis of high-quality and uniform graphene films on copper foils. *Science*. 2009; 324:1312–1314. [PubMed: 19423775]
360. Sutter PW, Flege JI, Sutter EA. Epitaxial graphene on ruthenium. *Nat Mater*. 2008; 7:406–411. [PubMed: 18391956]
361. Coraux J, N'Diaye AT, Busse C, Michely T. Structural Coherency of Graphene on Ir (111). *Nano Lett*. 2008; 8:565–570. [PubMed: 18189442]
362. Sutter P, Sadowski JT, Sutter E. Graphene on Pt (111): Growth and substrate interaction. *Phys Rev B*. 2009; 80:245411.
363. Varykhalov A, Rader O. Graphene grown on Co (0001) films and islands: Electronic structure and its precise magnetization dependence. *Phys Rev B*. 2009; 80:035437.
364. Kwon SY, Ciobanu CV, Petrova V, Shenoy VB, Bareno J, Gambin V, Petrov I, Kodambaka S. Growth of semiconducting graphene on palladium. *Nano Lett*. 2009; 9:3985–3990. [PubMed: 19995079]
365. Bae S, Kim H, Lee Y, Xu X, Park JS, Zheng Y, Balakrishnan J, Lei T, Kim HR, Song YI. Roll-to-Roll Production of 30-Inch Graphene Films for Transparent Electrodes. *Nat Nanotechnol*. 2010; 5:574–578. [PubMed: 20562870]
366. Li X, Zhu Y, Cai W, Borysiak M, Han B, Chen D, Piner RD, Colombo L, Ruoff RS. Transfer of large-area graphene films for high-performance transparent conductive electrodes. *Nano Lett*. 2009; 9:4359–4363. [PubMed: 19845330]
367. Berger C, Song Z, Li T, Li X, Ogbazghi AY, Feng R, Dai Z, Marchenkov AN, Conrad EH, First PN. Ultrathin Epitaxial Graphite: 2D Electron Gas Properties and a Route toward Graphene-Based Nanoelectronics. *J Phys Chem B*. 2004; 108:19912–19916.
368. Shivaraman S, Barton RA, Yu X, Alden J, Herman L, Chandrashekhar M, Park J, McEuen PL, Parpia JM, Craighead HG. Free-standing epitaxial graphene. *Nano Lett*. 2009; 9:3100–3105. [PubMed: 19663456]
369. Aristov VY, Urbanik G, Kummer K, Vyalikh DV, Molodtsova OV, Preobrajenski AB, Zakharov AA, Hess C, Hänke T, Buchner B. Graphene Synthesis on Cubic SiC/Si Wafers. Perspectives for Mass Production of Graphene-Based Electronic Devices. *Nano Lett*. 2010; 10:992–995. [PubMed: 20141155]
370. Emtsev KV, Bostwick A, Horn K, Jobst J, Kellogg GL, Ley L, McChesney JL, Ohta T, Reshanov SA, Röhr J. Towards wafer-size graphene layers by atmospheric pressure graphitization of silicon carbide. *Nat Mater*. 2009; 8:203–207. [PubMed: 19202545]
371. Deng D, Pan X, Zhang H, Fu Q, Tan D, Bao X. Freestanding graphene by thermal splitting of silicon carbide granules. *Adv Mater*. 2010; 22:2168–2171. [PubMed: 20352631]
372. Yang X, Dou X, Rouhanipour A, Zhi L, Räder HJ, Müllen K. Two-dimensional graphene nanoribbons. *J Am Chem Soc*. 2008; 130:4216–4217. [PubMed: 18324813]
373. Cai J, Ruffieux P, Jaafar R, Bieri M, Braun T, Blankenburg S, Muoth M, Seitsonen AP, Saleh M, Feng X. Atomically Precise Bottom-Up Fabrication of Graphene Nanoribbons. *Nature*. 2010; 466:470–473. [PubMed: 20651687]
374. Yan X, Cui X, Li L-s. Synthesis of large, stable colloidal graphene quantum dots with tunable size. *J Am Chem Soc*. 2010; 132:5944–5945. [PubMed: 20377260]
375. Yan X, Cui X, Li B, Li L-s. Large, solution-processable graphene quantum dots as light absorbers for photovoltaics. *Nano Lett*. 2010; 10:1869–1873. [PubMed: 20377198]

376. Bolotin KI, Sikes K, Jiang Z, Klima M, Fudenberg G, Hone J, Kim P, Stormer H. Ultrahigh Electron Mobility in Suspended Graphene. *Solid State Commun.* 2008; 146:351–355.
377. Pereira VM, Neto AC, Peres N. Tight-binding approach to uniaxial strain in graphene. *Phys Rev B.* 2009; 80:045401.
378. Ni ZH, Yu T, Lu YH, Wang YY, Feng YP, Shen ZX. Uniaxial strain on graphene: Raman spectroscopy study and band-gap opening. *ACS Nano.* 2008; 2:2301–2305. [PubMed: 19206396]
379. Castro EV, Novoselov K, Morozov S, Peres N, Dos Santos JL, Nilsson J, Guinea F, Geim A, Neto AC. Biased Bilayer Graphene: Semiconductor with a Gap Tunable by the Electric Field Effect. *Phys Rev Lett.* 2007; 99:216802. [PubMed: 18233240]
380. Gava P, Lazzeri M, Saitta AM, Mauri F. Ab initio study of gap opening and screening effects in gated bilayer graphene. *Phys Rev B.* 2009; 79:165431.
381. Ohta T, Bostwick A, Seyller T, Horn K, Rotenberg E. Controlling the electronic structure of bilayer graphene. *Science.* 2006; 313:951–954. [PubMed: 16917057]
382. Zhang Y, Tang TT, Girit C, Hao Z, Martin MC, Zettl A, Crommie MF, Shen YR, Wang F. Direct observation of a widely tunable bandgap in bilayer graphene. *Nature.* 2009; 459:820–823. [PubMed: 19516337]
383. Han MY, Özyilmaz B, Zhang Y, Kim P. Energy band-gap engineering of graphene nanoribbons. *Phys Rev Lett.* 2007; 98:206805. [PubMed: 17677729]
384. Chen Z, Lin YM, Rooks MJ, Avouris P. Graphene Nano-Ribbon Electronics. *Physica E.* 2007; 40:228–232.
385. Yang L, Park CH, Son YW, Cohen ML, Louie SG. Quasiparticle energies and band gaps in graphene nanoribbons. *Phys Rev Lett.* 2007; 99:186801. [PubMed: 17995426]
386. Evaldsson M, Zozoulenko IV, Xu H, Heinzl T. Edge-disorder-induced Anderson localization and conduction gap in graphene nanoribbons. *Phys Rev B.* 2008; 78:161407.
387. Wang Y, Wang T, Da P, Xu M, Wu H, Zheng G. Silicon nanowires for biosensing, energy storage, and conversion. *Adv Mater.* 2013; 25:5177–5195. [PubMed: 23828226]
388. Cui Y, Wei Q, Park H, Lieber CM. Nanowire Nanosensors for Highly Sensitive and Selective Detection of Biological and Chemical Species. *Science.* 2001; 293:1289–1292. [PubMed: 11509722]
389. Zheng G, Patolsky F, Cui Y, Wang WU, Lieber CM. Multiplexed electrical detection of cancer markers with nanowire sensor arrays. *Nat Biotechnol.* 2005; 23:1294–1301. [PubMed: 16170313]
390. Chua JH, Chee RE, Agarwal A, Wong SM, Zhang GJ. Label-Free Electrical Detection of Cardiac Biomarker with Complementary Metal-Oxide Semiconductor-Compatible Silicon Nanowire Sensor Arrays. *Anal Chem.* 2009; 81:6266–6271. [PubMed: 20337397]
391. Lin TW, Hsieh PJ, Lin CL, Fang YY, Yang JX, Tsai CC, Chiang PL, Pan CY, Chen YT. Label-free detection of protein-protein interactions using a calmodulin-modified nanowire transistor. *Proc Natl Acad Sci USA.* 2010; 107:1047–1052. [PubMed: 20080536]
392. Hahn, J-i; Lieber, CM. Direct ultrasensitive electrical detection of DNA and DNA sequence variations using nanowire nanosensors. *Nano Lett.* 2004; 4:51–54.
393. Li Z, Chen Y, Li X, Kamins T, Nauka K, Williams RS. Sequence-specific label-free DNA sensors based on silicon nanowires. *Nano Lett.* 2004; 4:245–247.
394. Ganguly A, Chen CP, Lai YT, Kuo CC, Hsu CW, Chen KH, Chen LC. Functionalized GaN nanowire-based electrode for direct label-free voltammetric detection of DNA hybridization. *J Mater Chem.* 2009; 19:928–933.
395. Patolsky F, Zheng G, Hayden O, Lakadamyali M, Zhuang X, Lieber CM. Electrical detection of single viruses. *Proc Natl Acad Sci USA.* 2004; 101:14017–14022. [PubMed: 15365183]
396. Wang WU, Chen C, Lin K-h, Fang Y, Lieber CM. Label-free detection of small-molecule-protein interactions by using nanowire nanosensors. *Proc Natl Acad Sci USA.* 2005; 102:3208–3212. [PubMed: 15716362]
397. Patolsky F, Zheng G, Lieber CM. Nanowire sensors for medicine and the life sciences. *Nanomedicine.* 2006; 1:51–65. [PubMed: 17716209]

398. Zhang GJ, Ning Y. Silicon nanowire biosensor and its applications in disease diagnostics: a review. *Anal Chim Acta*. 2012; 749:1–15. [PubMed: 23036462]
399. Janata J. Twenty years of ion-selective field-effect transistors. *Analyst*. 1994; 119:2275–2278.
400. Li C, Curreli M, Lin H, Lei B, Ishikawa F, Datar R, Cote RJ, Thompson ME, Zhou C. Complementary detection of prostate-specific antigen using In<sub>2</sub>O<sub>3</sub> nanowires and carbon nanotubes. *J Am Chem Soc*. 2005; 127:12484–12485. [PubMed: 16144384]
401. Yu R, Pan C, Wang ZL. High performance of ZnO nanowire protein sensors enhanced by the piezotronic effect. *Energy Environ Sci*. 2013; 6:494–499.
402. MacBeath G, Schreiber SL. Printing proteins as microarrays for high-throughput function determination. *Science*. 2000; 289:1760–1763. [PubMed: 10976071]
403. Patolsky F, Zheng G, Lieber CM. Fabrication of silicon nanowire devices for ultrasensitive, label-free, real-time detection of biological and chemical species. *Nat Protoc*. 2006; 1:1711–1724. [PubMed: 17487154]
404. Misra N, Martinez JA, Huang SCJ, Wang Y, Stroeve P, Grigoropoulos CP, Noy A. Bioelectronic silicon nanowire devices using functional membrane proteins. *Proc Natl Acad Sci USA*. 2009; 106:13780–13784. [PubMed: 19667177]
405. Ishikawa FN, Curreli M, Chang HK, Chen PC, Zhang R, Cote RJ, Thompson ME, Zhou C. A calibration method for nanowire biosensors to suppress device-to-device variation. *ACS Nano*. 2009; 3:3969–3976. [PubMed: 19921812]
406. Tian R, Regonda S, Gao J, Liu Y, Hu W. Ultrasensitive protein detection using lithographically defined Si multi-nanowire field effect transistors. *Lab Chip*. 2011; 11:1952–1961. [PubMed: 21505681]
407. Srinivas PR, Kramer BS, Srivastava S. Trends in biomarker research for cancer detection. *Lancet Oncol*. 2001; 2:698–704. [PubMed: 11902541]
408. Wulfkuhle JD, Liotta LA, Petricoin EF. Proteomic applications for the early detection of cancer. *Nat Rev Cancer*. 2003; 3:267–275. [PubMed: 12671665]
409. Stern E, Klemic JF, Routenberg DA, Wyrembak PN, Turner-Evans DB, Hamilton AD, LaVan DA, Fahmy TM, Reed MA. Label-free immunodetection with CMOS-compatible semiconducting nanowires. *Nature*. 2007; 445:519–522. [PubMed: 17268465]
410. Lu N, Gao A, Dai P, Song S, Fan C, Wang Y, Li T. CMOS-Compatible Silicon Nanowire Field-Effect Transistors for Ultrasensitive and Label-Free MicroRNAs Sensing. *Small*. 2014; 10:2022–2028. [PubMed: 24574202]
411. Wang X, Ozkan CS. Multisegment nanowire sensors for the detection of DNA molecules. *Nano Lett*. 2008; 8:398–404. [PubMed: 18211112]
412. Nielsen PE, Egholm M, Berg RH, Buchardt O. Sequence-selective recognition of DNA by strand displacement with a thymine-substituted polyamide. *Science*. 1991; 254:1497–1500. [PubMed: 1962210]
413. Jensen KK, Ørum H, Nielsen PE, Nordén B. Kinetics for hybridization of peptide nucleic acids (PNA) with DNA and RNA studied with the BIAcore technique. *Biochem*. 1997; 36:5072–5077. [PubMed: 9125529]
414. Zhang GJ, Zhang G, Chua JH, Chee RE, Wong EH, Agarwal A, Buddharaju KD, Singh N, Gao Z, Balasubramanian N. DNA sensing by silicon nanowire: charge layer distance dependence. *Nano Lett*. 2008; 8:1066–1070. [PubMed: 18311939]
415. Bunimovich YL, Shin YS, Yeo WS, Amori M, Kwong G, Heath JR. Quantitative Real-Time Measurements of DNA Hybridization with Alkylated Nonoxidized Silicon Nanowires in Electrolyte Solution. *J Am Chem Soc*. 2006; 128:16323–16331. [PubMed: 17165787]
416. Cissell KA, Shrestha S, Deo SK. MicroRNA detection: challenges for the analytical chemist. *Anal Chem*. 2007; 79:4754–4761.
417. Zhang GJ, Chua JH, Chee RE, Agarwal A, Wong SM. Label-free direct detection of MiRNAs with silicon nanowire biosensors. *Biosens Bioelectron*. 2009; 24:2504–2508. [PubMed: 19188058]
418. Strauss, EG.; Strauss, JH. *Viruses and human disease*. Academic Press; San Diego: 2007.
419. Shen F, Wang J, Xu Z, Wu Y, Chen Q, Li X, Jie X, Li L, Yao M, Guo X. Rapid flu diagnosis using silicon nanowire sensor. *Nano Lett*. 2012; 12:3722–3730. [PubMed: 22731392]

420. Zhang GJ, Zhang L, Huang MJ, Luo ZHH, Tay GKI, Lim EJA, Kang TG, Chen Y. Silicon nanowire biosensor for highly sensitive and rapid detection of Dengue virus. *Sens Actuators B Chem.* 2010; 146:138–144.
421. Sze, SM.; Ng, KK. *Physics of semiconductor devices.* John Wiley & Sons; 2006.
422. Gao XP, Zheng G, Lieber CM. Subthreshold regime has the optimal sensitivity for nanowire FET biosensors. *Nano Lett.* 2010; 10:547–552. [PubMed: 19908823]
423. Stern E, Wagner R, Sigworth FJ, Breaker R, Fahmy TM, Reed MA. Importance of the Debye screening length on nanowire field effect transistor sensors. *Nano Lett.* 2007; 7:3405–3409. [PubMed: 17914853]
424. Maehashi K, Katsura T, Kerman K, Takamura Y, Matsumoto K, Tamiya E. Label-free protein biosensor based on aptamer-modified carbon nanotube field-effect transistors. *Anal Chem.* 2007; 79:782–787. [PubMed: 17222052]
425. Elnathan R, Kwiat M, Pevzner A, Engel Y, Burstein L, Khatchourints A, Lichtenstein A, Kantaev R, Patolsky F. Biorecognition layer engineering: overcoming screening limitations of nanowire-based FET devices. *Nano Lett.* 2012; 12:5245–5254. [PubMed: 22963381]
426. Kulkarni GS, Zhong Z. Detection beyond the Debye screening length in a high-frequency nanoelectronic biosensor. *Nano Lett.* 2012; 12:719–723. [PubMed: 22214376]
427. Gao N, Zhou W, Jiang X, Hong G, Fu TM, Lieber CM. General strategy for biodetection in high ionic strength solutions using transistor-based nanoelectronic sensors. *Nano Lett.* 2015; 15:2143–2148. [PubMed: 25664395]
428. Gong JR. Label-Free Attomolar Detection of Proteins Using Integrated Nanoelectronic and Electrokinetic Devices. *Small.* 2010; 6:967–973. [PubMed: 20209654]
429. Zheng G, Gao XP, Lieber CM. Frequency domain detection of biomolecules using silicon nanowire biosensors. *Nano Lett.* 2010; 10:3179–3183. [PubMed: 20698634]
430. Weissman M.  $1/f$  noise and other slow, nonexponential kinetics in condensed matter. *Rev Mod Phys.* 1988; 60:537.
431. Simoen E, Claeys C. On the flicker noise in submicron silicon MOSFETs. *Solid State Electron.* 1999; 43:865–882.
432. Xie P, Xiong Q, Fang Y, Qing Q, Lieber CM. Local electrical potential detection of DNA by nanowire-nanopore sensors. *Nat Nanotechnol.* 2012; 7:119–125. [PubMed: 22157724]
433. Branton D, Deamer DW, Marziali A, Bayley H, Benner SA, Butler T, Di Ventra M, Garaj S, Hibbs A, Huang X. The potential and challenges of nanopore sequencing. *Nat Biotechnol.* 2008; 26:1146–1153. [PubMed: 18846088]
434. Ahn JH, Choi SJ, Han JW, Park TJ, Lee SY, Choi YK. Double-Gate Nanowire Field Effect Transistor for a Biosensor. *Nano Lett.* 2010; 10:2934–2938. [PubMed: 20698606]
435. Parihar MS, Kranti A. Enhanced sensitivity of double gate junctionless transistor architecture for biosensing applications. *Nanotechnology.* 2015; 26:145201. [PubMed: 25771821]
436. Makowski MS, Ivanisevic A. Molecular Analysis of Blood with Micro-/Nanoscale Field-Effect-Transistor Biosensors. *Small.* 2011; 7:1863–1875. [PubMed: 21638783]
437. Kim KS, Lee HS, Yang JA, Jo MH, Hahn SK. The fabrication, characterization and application of aptamer-functionalized Si-nanowire FET biosensors. *Nanotechnology.* 2009; 20:235501. [PubMed: 19448297]
438. Stern E, Vacic A, Rajan NK, Criscione JM, Park J, Ilic BR, Mooney DJ, Reed MA, Fahmy TM. Label-free biomarker detection from whole blood. *Nat Nanotechnol.* 2010; 5:138–142. [PubMed: 20010825]
439. Zhang GJ, Chai KTC, Luo HZH, Huang JM, Tay IGK, Lim AEJ, Je M. Multiplexed detection of cardiac biomarkers in serum with nanowire arrays using readout ASIC. *Biosens Bioelectron.* 2012; 35:218–223. [PubMed: 22459581]
440. Zhou W, Dai X, Fu TM, Xie C, Liu J, Lieber CM. Long term stability of nanowire nanoelectronics in physiological environments. *Nano Lett.* 2014; 14:1614–1619. [PubMed: 24479700]
441. Gooding JJ. Nanostructuring electrodes with carbon nanotubes: A review on electrochemistry and applications for sensing. *Electrochim Acta.* 2005; 50:3049–3060.

442. Ahammad A, Lee JJ, Rahman MA. Electrochemical Sensors Based on Carbon Nanotubes. *Sensors*. 2009; 9:2289–2319. [PubMed: 22574013]
443. Jacobs CB, Peairs MJ, Venton BJ. Review: Carbon nanotube based electrochemical sensors for biomolecules. *Anal Chim Acta*. 2010; 662:105–127. [PubMed: 20171310]
444. Vashist SK, Zheng D, Al-Rubeaan K, Luong JH, Sheu FS. Advances in carbon nanotube based electrochemical sensors for bioanalytical applications. *Biotechnol Adv*. 2011; 29:169–188. [PubMed: 21034805]
445. Yáñez-Sedeño P, Pingarrón JM, Riu J, Rius FX. Electrochemical sensing based on carbon nanotubes. *TrAC, Trends Anal Chem*. 2010; 29:939–953.
446. Allen BL, Kichambare PD, Star A. Carbon Nanotube Field-Effect-Transistor-Based Biosensors. *Adv Mater*. 2007; 19:1439–1451.
447. Kauffman DR, Star A. Electronically monitoring biological interactions with carbon nanotube field-effect transistors. *Chem Soc Rev*. 2008; 37:1197–1206. [PubMed: 18497932]
448. Yang N, Chen X, Ren T, Zhang P, Yang D. Carbon nanotube based biosensors. *Sens Actuators B Chem*. 2015; 207:690–715.
449. Liu S, Guo X. Carbon nanomaterials field-effect-transistor-based biosensors. *NPG Asia Mater*. 2012; 4:e23.
450. Wang XN, Hu PA. Carbon nanomaterials: controlled growth and field-effect transistor biosensors. *Front Mater Sci*. 2012; 6:26–46.
451. Hu P, Fasoli A, Park J, Choi Y, Estrela P, Maeng S, Milne W, Ferrari A. Self- assembled nanotube field-effect transistors for label-free protein biosensors. *J Appl Phys*. 2008; 104
452. Artyukhin AB, Stadermann M, Friddle RW, Stroeve P, Bakajin O, Noy A. Controlled Electrostatic Gating of Carbon Nanotube FET Devices. *Nano Lett*. 2006; 6:2080–2085. [PubMed: 16968029]
453. Heller I, Janssens AM, Männik J, Minot ED, Lemay SG, Dekker C. Identifying the mechanism of biosensing with carbon nanotube transistors. *Nano Lett*. 2008; 8:591–595. [PubMed: 18162002]
454. Star A, Gabriel JCP, Bradley K, Grüner G. Electronic detection of specific protein binding using nanotube FET devices. *Nano Lett*. 2003; 3:459–463.
455. Hecht DS, Ramirez RJ, Briman M, Artukovic E, Chichak KS, Stoddart JF, Grüner G. Bioinspired detection of light using a porphyrin-sensitized single-wall nanotube field effect transistor. *Nano Lett*. 2006; 6:2031–2036. [PubMed: 16968021]
456. Chen RJ, Choi HC, Bangsaruntip S, Yenilmez E, Tang X, Wang Q, Chang YL, Dai H. An Investigation of the Mechanisms of Electronic Sensing of Protein Adsorption on Carbon Nanotube Devices. *J Am Chem Soc*. 2004; 126:1563–1568. [PubMed: 14759216]
457. Gui EL, Li LJ, Zhang K, Xu Y, Dong X, Ho X, Lee PS, Kasim J, Shen Z, Rogers JA. DNA sensing by field-effect transistors based on networks of carbon nanotubes. *J Am Chem Soc*. 2007; 129:14427–14432. [PubMed: 17973383]
458. Karousis N, Tagmatarchis N, Tasis D. Current progress on the chemical modification of carbon nanotubes. *Chem Rev*. 2010; 110:5366–5397. [PubMed: 20545303]
459. Zhao YL, Stoddart JF. Noncovalent functionalization of single-walled carbon nanotubes. *Acc Chem Res*. 2009; 42:1161–1171. [PubMed: 19462997]
460. Chen RJ, Zhang Y, Wang D, Dai H. Noncovalent Sidewall Functionalization of Single-Walled Carbon Nanotubes for Protein Immobilization. *J Am Chem Soc*. 2001; 123:3838–3839. [PubMed: 11457124]
461. Peng X, Wong SS. Functional covalent chemistry of carbon nanotube surfaces. *Adv Mater*. 2009; 21:625–642.
462. Ajayan P. Nanotubes from Carbon. *Chem Rev*. 1999; 99:1787–1800. [PubMed: 11849010]
463. Zheng M, Jagota A, Semke ED, Diner BA, McLean RS, Lustig SR, Richardson RE, Tassi NG. DNA-assisted dispersion and separation of carbon nanotubes. *Nat Mater*. 2003; 2:338–342. [PubMed: 12692536]
464. Chen RJ, Bangsaruntip S, Drouvalakis KA, Kam NWS, Shim M, Li Y, Kim W, Utz PJ, Dai H. Noncovalent Functionalization of Carbon Nanotubes for Highly Specific Electronic Biosensors. *Proc Natl Acad Sci USA*. 2003; 100:4984–4989. [PubMed: 12697899]

465. Besteman K, Lee JO, Wiertz FG, Heering HA, Dekker C. Enzyme-Coated Carbon Nanotubes as Single-Molecule Biosensors. *Nano Lett.* 2003; 3:727–730.
466. Münzer AM, Seo W, Morgan GJ, Michael ZP, Zhao Y, Melzer K, Scarpa G, Star A. Sensing reversible protein–ligand interactions with single-walled carbon nanotube field-effect transistors. *J Phys Chem C.* 2014; 118:17193–17199.
467. Star A, Tu E, Niemann J, Gabriel JCP, Joiner CS, Valcke C. Label-free detection of DNA hybridization using carbon nanotube network field-effect transistors. *Proc Natl Acad Sci USA.* 2006; 103:921–926. [PubMed: 16418278]
468. Martínez MT, Tseng YC, Ormategui N, Loinaz I, Eritja R, Bokor J. Label-free DNA biosensors based on functionalized carbon nanotube field effect transistors. *Nano Lett.* 2009; 9:530–536. [PubMed: 19125575]
469. Sorgenfrei S, Chiu C-y, Gonzalez RL Jr, Yu YJ, Kim P, Nuckolls C, Shepard KL. Label-free single-molecule detection of DNA-hybridization kinetics with a carbon nanotube field-effect transistor. *Nat Nanotechnol.* 2011; 6:126–132. [PubMed: 21258331]
470. Li WS, Hou PX, Liu C, Sun DM, Yuan J, Zhao SY, Yin LC, Cong H, Cheng HM. High-quality, highly concentrated semiconducting single-wall carbon nanotubes for use in field effect transistors and biosensors. *ACS Nano.* 2013; 7:6831–6839. [PubMed: 23883135]
471. Lerner MB, Kybert N, Mendoza R, Villechenon R, Lopez MAB, Johnson AC. Scalable, non-invasive glucose sensor based on boronic acid functionalized carbon nanotube transistors. *Appl Phys Lett.* 2013; 102:183113.
472. Barik MA, Dutta JC. Fabrication and Characterization of Junctionless Carbon Nanotube Field Effect Transistor for Cholesterol Detection. *Appl Phys Lett.* 2014; 105:053509.
473. Huang SCJ, Artyukhin AB, Misra N, Martinez JA, Stroeve PA, Grigoropoulos CP, Ju JWW, Noy A. Carbon nanotube transistor controlled by a biological ion pump gate. *Nano Lett.* 2010; 10:1812–1816. [PubMed: 20426455]
474. Wang CW, Pan CY, Wu HC, Shih PY, Tsai CC, Liao KT, Lu LL, Hsieh WH, Chen CD, Chen YT. In Situ Detection of Chromogranin A Released from Living Neurons with a Single-Walled Carbon-Nanotube Field-Effect Transistor. *Small.* 2007; 3:1350–1355. [PubMed: 17576645]
475. Huang Y, Sudibya HG, Fu D, Xue R, Dong X, Li LJ, Chen P. Label-free detection of ATP release from living astrocytes with high temporal resolution using carbon nanotube network. *Biosens Bioelectron.* 2009; 24:2716–2720. [PubMed: 19135355]
476. Heller I, Smaal W, Lemay SG, Dekker C. Probing Macrophage Activity with Carbon-Nanotube Sensors. *Small.* 2009; 5:2528–2532. [PubMed: 19697305]
477. Sudibya HG, Ma J, Dong X, Ng S, Li LJ, Liu XW, Chen P. Interfacing Glycosylated Carbon-Nanotube-Network Devices with Living Cells to Detect Dynamic Secretion of Biomolecules. *Angew Chem Int Ed.* 2009; 48:2723–2726.
478. Liu Y, Dong X, Chen P. Biological and chemical sensors based on graphene materials. *Chem Soc Rev.* 2012; 41:2283–2307. [PubMed: 22143223]
479. Yin PT, Shah S, Chhowalla M, Lee KB. Design, Synthesis, and Characterization of Graphene–Nanoparticle Hybrid Materials for Bioapplications. *Chem Rev.* 2015; 115:2483–2531. [PubMed: 25692385]
480. Georgakilas V, Otyepka M, Bourlino AB, Chandra V, Kim N, Kemp KC, Hobza P, Zboril R, Kim KS. Functionalization of graphene: covalent and non-covalent approaches, derivatives and applications. *Chem Rev.* 2012; 112:6156–6214. [PubMed: 23009634]
481. Mohanty N, Berry V. Graphene-based single-bacterium resolution biodevice and DNA transistor: interfacing graphene derivatives with nanoscale and microscale biocomponents. *Nano Lett.* 2008; 8:4469–4476. [PubMed: 19367973]
482. Dong X, Shi Y, Huang W, Chen P, Li LJ. Electrical Detection of DNA Hybridization with Single-Base Specificity Using Transistors Based on CVD-Grown Graphene Sheets. *Adv Mater.* 2010; 22:1649–1653. [PubMed: 20496398]
483. Chen TY, Loan PTK, Hsu CL, Lee YH, Wang JTW, Wei KH, Lin CT, Li LJ. Label-Free Detection of DNA Hybridization using Transistors Based on CVD Grown Graphene. *Biosens Bioelectron.* 2013; 41:103–109. [PubMed: 22944023]

484. Lin CT, Loan PTK, Chen TY, Liu KK, Chen CH, Wei KH, Li LJ. Label-Free Electrical Detection of DNA Hybridization on Graphene using Hall Effect Measurements: Revisiting the Sensing Mechanism. *Adv Funct Mater.* 2013; 23:2301–2307.
485. Cai B, Wang S, Huang L, Ning Y, Zhang Z, Zhang GJ. Ultrasensitive Label-Free Detection of PNA–DNA Hybridization by Reduced Graphene Oxide Field-Effect Transistor Biosensor. *ACS Nano.* 2014; 8:2632–2638. [PubMed: 24528470]
486. Ohno Y, Maehashi K, Yamashiro Y, Matsumoto K. Electrolyte-gated graphene field-effect transistors for detecting pH and protein adsorption. *Nano Lett.* 2009; 9:3318–3322. [PubMed: 19637913]
487. Ohno Y, Maehashi K, Matsumoto K. Label-free biosensors based on aptamer-modified graphene field-effect transistors. *J Am Chem Soc.* 2010; 132:18012–18013. [PubMed: 21128665]
488. Mao S, Lu G, Yu K, Bo Z, Chen J. Specific Protein Detection Using Thermally Reduced Graphene Oxide Sheet Decorated with Gold Nanoparticle-Antibody Conjugates. *Adv Mater.* 2010; 22:3521–3526. [PubMed: 20665564]
489. He Q, Wu S, Gao S, Cao X, Yin Z, Li H, Chen P, Zhang H. Transparent, flexible, all-reduced graphene oxide thin film transistors. *ACS Nano.* 2011; 5:5038–5044. [PubMed: 21524119]
490. Huang Y, Dong X, Shi Y, Li CM, Li LJ, Chen P. Nanoelectronic biosensors based on CVD grown graphene. *Nanoscale.* 2010; 2:1485–1488. [PubMed: 20820739]
491. He Q, Sudibya HG, Yin Z, Wu S, Li H, Boey F, Huang W, Chen P, Zhang H. Centimeter-long and large-scale micropatterns of reduced graphene oxide films: fabrication and sensing applications. *ACS Nano.* 2010; 4:3201–3208. [PubMed: 20441213]
492. Huang Y, Dong X, Liu Y, Li LJ, Chen P. Graphene-based biosensors for detection of bacteria and their metabolic activities. *J Mater Chem.* 2011; 21:12358–12362.
493. Kwon OS, Lee SH, Park SJ, An JH, Song HS, Kim T, Oh JH, Bae J, Yoon H, Park TH. Large-scale graphene micropattern nano-biohybrids: high-performance transducers for FET-type flexible fluidic HIV immunoassays. *Adv Mater.* 2013; 25:4177–4185. [PubMed: 23744620]
494. Ang PK, Li A, Jaiswal M, Wang Y, Hou HW, Thong JT, Lim CT, Loh KP. Flow Sensing of Single Cell by Graphene Transistor in a Microfluidic Channel. *Nano Lett.* 2011; 11:5240–5246. [PubMed: 22077950]
495. Kühlbrandt W. The resolution revolution. *Science.* 2014; 343:1443–1444. [PubMed: 24675944]
496. Cheng Y. Single-particle cryo-EM at crystallographic resolution. *Cell.* 2015; 161:450–457. [PubMed: 25910205]
497. Luck, SJ. An introduction to the event-related potential technique. MIT press; 2014.
498. Guye M, Bettus G, Bartolomei F, Cozzone PJ. Graph theoretical analysis of structural and functional connectivity MRI in normal and pathological brain networks. *Magnetic Resonance Materials in Physics, Biology and Medicine.* 2010; 23:409–421.
499. Logothetis NK. What we can do and what we cannot do with fMRI. *Nature.* 2008; 453:869–878. [PubMed: 18548064]
500. Buzsaki G, Anastassiou CA, Koch C. The Origin of Extracellular Fields and Currents - EEG, ECoG, LFP and Spikes. *Nat Rev Neurosci.* 2012; 13:407–420. [PubMed: 22595786]
501. Siegel MS, Isacoff EY. A genetically encoded optical probe of membrane voltage. *Neuron.* 1997; 19:735–741. [PubMed: 9354320]
502. Stosiek C, Garaschuk O, Holthoff K, Konnerth A. In vivo two-photon calcium imaging of neuronal networks. *Proc Natl Acad Sci USA.* 2003; 100:7319–7324. [PubMed: 12777621]
503. Mittmann W, Wallace DJ, Czubyko U, Herb JT, Schaefer AT, Looger LL, Denk W, Kerr JN. Two-photon calcium imaging of evoked activity from L5 somatosensory neurons in vivo. *Nat Neurosci.* 2011; 14:1089–1093. [PubMed: 21743473]
504. Scanziani M, Hausser M. Electrophysiology in the age of light. *Nature.* 2009; 461:930–939. [PubMed: 19829373]
505. Warden MR, Cardin JA, Deisseroth K. Optical neural interfaces. *Annu Rev Biomed Eng.* 2014; 16:103–129. [PubMed: 25014785]

506. Kralj JM, Douglass AD, Hochbaum DR, Maclaurin D, Cohen AE. Optical recording of action potentials in mammalian neurons using a microbial rhodopsin. *Nat Methods*. 2012; 9:90–95. [PubMed: 22120467]
507. Silva GA. Neuroscience nanotechnology: Progress, opportunities and challenges. *Nat Rev Neurosci*. 2006; 7:65–74. [PubMed: 16371951]
508. Kotov NA, Winter JO, Clements IP, Jan E, Timko BP, Campidelli S, Pathak S, Mazzatenta A, Lieber CM, Prato M, et al. Nanomaterials for Neural Interfaces. *Adv Mater*. 2009; 21:3970–4004.
509. Alivisatos AP, Chun M, Church GM, Greenspan RJ, Roukes ML, Yuste R. The brain activity map project and the challenge of functional connectomics. *Neuron*. 2012; 74:970–974. [PubMed: 22726828]
510. Alivisatos AP, Andrews AM, Boyden ES, Chun M, Church GM, Deisseroth K, Donoghue JP, Fraser SE, Lippincott-Schwartz J, Looger LL, et al. Nanotools for Neuroscience and Brain Activity Mapping. *ACS Nano*. 2013; 7:1850–1866. [PubMed: 23514423]
511. Angle MR, Cui B, Melosh NA. Nanotechnology and Neurophysiology. *Curr Opin Neurobiol*. 2015; 32:132–140. [PubMed: 25889532]
512. Thomas C, Springer P, Loeb G, Berwald-Netter Y, Okun L. A miniature microelectrode array to monitor the bioelectric activity of cultured cells. *Exp Cell Res*. 1972; 74:61–66. [PubMed: 4672477]
513. Johnstone AF, Gross GW, Weiss DG, Schroeder OHU, Gramowski A, Shafer TJ. Microelectrode arrays: a physiologically based neurotoxicity testing platform for the 21st century. *Neurotoxicology*. 2010; 31:331–350. [PubMed: 20399226]
514. Berdondini L, Imfeld K, Maccione A, Tedesco M, Neukom S, Koudelka-Hep M, Martinoia S. Active Pixel Sensor Array for High Spatio-Temporal Resolution Electrophysiological Recordings from Single Cell to Large Scale Neuronal Networks. *Lab Chip*. 2009; 9:2644–2651. [PubMed: 19704979]
515. Nam Y, Wheeler BC. In Vitro Microelectrode Array Technology and Neural Recordings. *Crit Rev Biomed Eng*. 2011; 39:45–61. [PubMed: 21488814]
516. Huys R, Braeken D, Jans D, Stassen A, Collaert N, Wouters J, Loo J, Severi S, Vleugels F, Callewaert G. Single-cell recording and stimulation with a 16k micro-nail electrode array integrated on a 0.18  $\mu\text{m}$  CMOS chip. *Lab Chip*. 2012; 12:1274–1280. [PubMed: 22337001]
517. Hochberg LR, Serruya MD, Friehs GM, Mukand JA, Saleh M, Caplan AH, Branner A, Chen D, Penn RD, Donoghue JP. Neuronal ensemble control of prosthetic devices by a human with tetraplegia. *Nature*. 2006; 442:164–171. [PubMed: 16838014]
518. Berényi A, Somogyvari Z, Nagy AJ, Roux L, Long JD, Fujisawa S, Stark E, Leonardo A, Harris TD, Buzsáki G. Large-Scale, High-Density (up to 512 Channels) Recording of Local Circuits in Behaving Animals. *J Neurophysiol*. 2014; 111:1132–1149. [PubMed: 24353300]
519. Gross GW, Rhoades BK, Reust DL, Schwalm FU. Stimulation of monolayer networks in culture through thin-film indium-tin oxide recording electrodes. *J Neurosci Methods*. 1993; 50:131–143. [PubMed: 8107494]
520. Spira ME, Hai A. Multi-electrode array technologies for neuroscience and cardiology. *Nat Nanotechnol*. 2013; 8:83–94. [PubMed: 23380931]
521. Nelson MJ, Pouget P, Nilsen EA, Patten CD, Schall JD. Review of signal distortion through metal microelectrode recording circuits and filters. *J Neurosci Methods*. 2008; 169:141–157. [PubMed: 18242715]
522. Pine J. Recording action potentials from cultured neurons with extracellular microcircuit electrodes. *J Neurosci Methods*. 1980; 2:19–31. [PubMed: 7329089]
523. Kim JH, Kang G, Nam Y, Choi YK. Surface-modified microelectrode array with flake nanostructure for neural recording and stimulation. *Nanotechnology*. 2010; 21:085303.
524. Keefer EW, Botterman BR, Romero MI, Rossi AF, Gross GW. Carbon nanotube coating improves neuronal recordings. *Nat Nanotechnol*. 2008; 3:434–439. [PubMed: 18654569]
525. Bareket-Keren L, Hanein Y. Carbon Nanotube-Based Multi Electrode Arrays for Neuronal Interfacing: Progress and Prospects. *Front Neural Circuits*. 2012; 6:122. [PubMed: 23316141]

526. Fromherz P, Offenhausser A, Vetter T, Weis J. A neuron-silicon junction: a Retzius cell of the leech on an insulated-gate field-effect transistor. *Science*. 1991; 252:1290–1293. [PubMed: 1925540]
527. Voelker M, Fromherz P. Signal transmission from individual mammalian nerve cell to field-effect transistor. *Small*. 2005; 1:206–210. [PubMed: 17193431]
528. Wrobel G, Höller M, Ingebrandt S, Dieluweit S, Sommerhage F, Bochem HP, Offenhausser A. Transmission electron microscopy study of the cell–sensor interface. *J R Soc Interface*. 2008; 5:213–222. [PubMed: 17609177]
529. Santoro F, Dasgupta S, Schnitker J, Auth T, Neumann E, Panaitov G, Gompper G, Offenhausser A. Interfacing electrogenic cells with 3d nanoelectrodes: position, shape, and size matter. *ACS Nano*. 2014; 8:6713–6723. [PubMed: 24963873]
530. Toma K, Kano H, Offenhausser A. Label-Free Measurement of Cell–Electrode Cleft Gap Distance with High Spatial Resolution Surface Plasmon Microscopy. *ACS Nano*. 2014; 8:12612–12619. [PubMed: 25423587]
531. Van Pelt J, Wolters PS, Corner M, Rutten WL, Ramakers GJ. Long-term characterization of firing dynamics of spontaneous bursts in cultured neural networks. *IEEE Trans Biomed Eng*. 2004; 51:2051–2062. [PubMed: 15536907]
532. Morefield S, Keefer E, Chapman K, Gross G. Drug evaluations using neuronal networks cultured on microelectrode arrays. *Biosens Bioelectron*. 2000; 15:383–396. [PubMed: 11219752]
533. Ruaro ME, Bonifazi P, Torre V. Toward the neurocomputer: image processing and pattern recognition with neuronal cultures. *IEEE Trans Biomed Eng*. 2005; 52:371–383. [PubMed: 15759567]
534. Craighead H, Turner S, Davis R, James C, Perez A, John PS, Isaacson M, Kam L, Shain W, Turner J. Chemical and Topographical Surface Modification for Control of Central Nervous System Cell Adhesion. *Biomed Microdevices*. 1998; 1:49–64.
535. Craighead H, James C, Turner A. Chemical and Topographical Patterning for Directed Cell Attachment. *Curr Opin Solid State Mater Sci*. 2001; 5:177–184.
536. Hai A, Shappir J, Spira ME. Long-Term, Multisite, Parallel, In-Cell Recording and Stimulation by an Array of Extracellular Microelectrodes. *J Neurophysiol*. 2010; 104:559–568. [PubMed: 20427620]
537. Patolsky F, Timko BP, Yu G, Fang Y, Greytak AB, Zheng G, Lieber CM. Detection, stimulation, and inhibition of neuronal signals with high-density nanowire transistor arrays. *Science*. 2006; 313:1100–1104. [PubMed: 16931757]
538. Pui TS, Agarwal A, Ye F, Balasubramanian N, Chen P. CMOS-Compatible Nanowire Sensor Arrays for Detection of Cellular Bioelectricity. *Small*. 2009; 5:208–212. [PubMed: 19107889]
539. Cohen-Karni T, Timko BP, Weiss LE, Lieber CM. Flexible Electrical Recording from Cells Using Nanowire Transistor Arrays. *Proc Natl Acad Sci USA*. 2009; 106:7309–7313. [PubMed: 19365078]
540. Eschermann JF, Stockmann R, Hueske M, Vu XT, Ingebrandt S, Offenhausser A. Action potentials of HL-1 cells recorded with silicon nanowire transistors. *Appl Phys Lett*. 2009; 95:083703.
541. Dankerl M, Eick S, Hofmann B, Hauf M, Ingebrandt S, Offenhausser A, Stutzmann M, Garrido JA. Diamond Transistor Array for Extracellular Recording from Electrogenic Cells. *Adv Funct Mater*. 2009; 19:2915–2923.
542. Van Renterghem C, Romey G, Lazdunski M. Vasopressin modulates the spontaneous electrical activity in aortic cells (line A7r5) by acting on three different types of ionic channels. *Proc Natl Acad Sci USA*. 1988; 85:9365–9369. [PubMed: 2461570]
543. Brueggemann LI, Moran CJ, Barakat JA, Yeh JZ, Cribbs LL, Byron KL. Vasopressin stimulates action potential firing by protein kinase C-dependent inhibition of KCNQ5 in A7r5 rat aortic smooth muscle cells. *Am J Physiol Heart Circ Physiol*. 2007; 292:H1352–H1363. [PubMed: 17071736]
544. Cohen-Karni T, Qing Q, Li Q, Fang Y, Lieber CM. Graphene and Nanowire Transistors for Cellular Interfaces and Electrical Recording. *Nano Lett*. 2010; 10:1098–1102. [PubMed: 20136098]

545. Hess LH, Jansen M, Maybeck V, Hauf MV, Seifert M, Stutzmann M, Sharp ID, Offenhäusser A, Garrido JA. Graphene Transistor Arrays for Recording Action Potentials from Electrogenic Cells. *Adv Mater.* 2011; 23:5045–5049. [PubMed: 21953832]
546. Cheng Z, Hou J, Zhou Q, Li T, Li H, Yang L, Jiang K, Wang C, Li Y, Fang Y. Sensitivity Limits and Scaling of Bioelectronic Graphene Transducers. *Nano Lett.* 2013; 13:2902–2907. [PubMed: 23638876]
547. Chorev E, Epsztein J, Houweling AR, Lee AK, Brecht M. Electrophysiological Recordings from Behaving Animals—Going Beyond Spikes. *Curr Opin Neurobiol.* 2009; 19:513–519. [PubMed: 19735997]
548. Hodgkin AL, Huxley AF. Action potentials recorded from inside a nerve fibre. *Nature.* 1939; 144:710–711.
549. Molleman, A. Patch clamping: an introductory guide to patch clamp electrophysiology. John Wiley & Sons; Chichester, England: 2003.
550. Duan X, Fu TM, Liu J, Lieber CM. Nanoelectronics-biology frontier: From nanoscopic probes for action potential recording in live cells to three-dimensional cyborg tissues. *Nano Today.* 2013; 8:351–373. [PubMed: 24073014]
551. Hai A, Dormann A, Shappir J, Yitzchaik S, Bartic C, Borghs G, Langedijk J, Spira ME. Spine-shaped gold protrusions improve the adherence and electrical coupling of neurons with the surface of micro-electronic devices. *J R Soc Interface.* 2009; 6:1153–1165. [PubMed: 19474080]
552. Hai A, Kamber D, Malkinson G, Erez H, Mazurski N, Shappir J, Spira ME. Changing gears from chemical adhesion of cells to flat substrata toward engulfment of micro-protrusions by active mechanisms. *J Neural Eng.* 2009; 6:066009. [PubMed: 19918108]
553. Hai A, Shappir J, Spira ME. In-cell recordings by extracellular microelectrodes. *Nat Methods.* 2010; 7:200–202. [PubMed: 20118930]
554. Santoro F, Schnitker J, Panaitov G, Offenhäusser A. On chip guidance and recording of cardiomyocytes with 3D mushroom-shaped electrodes. *Nano Lett.* 2013; 13:5379–5384. [PubMed: 24088026]
555. Jiang Z, Qing Q, Xie P, Gao R, Lieber CM. Kinked p–n junction nanowire probes for high spatial resolution sensing and intracellular recording. *Nano Lett.* 2012; 12:1711–1716. [PubMed: 22309132]
556. Duan X, Gao R, Xie P, Cohen-Karni T, Qing Q, Choe HS, Tian B, Jiang X, Lieber CM. Intracellular recordings of action potentials by an extracellular nanoscale field-effect transistor. *Nat Nanotechnol.* 2012; 7:174–179. [PubMed: 22179566]
557. Gao R, Strehle S, Tian B, Cohen-Karni T, Xie P, Duan X, Qing Q, Lieber CM. Outside Looking In: Nanotube Transistor Intracellular Sensors. *Nano Lett.* 2012; 12:3329–3333. [PubMed: 22583370]
558. Qing Q, Jiang Z, Xu L, Gao R, Mai L, Lieber CM. Free-standing kinked nanowire transistor probes for targeted intracellular recording in three dimensions. *Nat Nanotechnol.* 2014; 9:142–147. [PubMed: 24336402]
559. Fu TM, Duan X, Jiang Z, Dai X, Xie P, Cheng Z, Lieber CM. Sub-10-nm intracellular bioelectronic probes from nanowire–nanotube heterostructures. *Proc Natl Acad Sci USA.* 2014; 111:1259–1264. [PubMed: 24474745]
560. Robinson JT, Jorgolli M, Shalek AK, Yoon MH, Gertner RS, Park H. Vertical nanowire electrode arrays as a scalable platform for intracellular interfacing to neuronal circuits. *Nat Nanotechnol.* 2012; 7:180–184. [PubMed: 22231664]
561. Xie C, Lin Z, Hanson L, Cui Y, Cui B. Intracellular recording of action potentials by nanopillar electroporation. *Nat Nanotechnol.* 2012; 7:185–190. [PubMed: 22327876]
562. Almquist BD, Melosh NA. Fusion of Biomimetic Stealth Probes into Lipid Bilayer Cores. *Proc Natl Acad Sci USA.* 2010; 107:5815–5820. [PubMed: 20212151]
563. Almquist BD, Melosh NA. Molecular Structure Influences the Stability of Membrane Penetrating Biointerfaces. *Nano Lett.* 2011; 11:2066–2070. [PubMed: 21469728]
564. Almquist BD, Verma P, Cai W, Melosh NA. Nanoscale Patterning Controls Inorganic–Membrane Interface Structure. *Nanoscale.* 2011; 3:391–400. [PubMed: 20931126]

565. Xie X, Xu AM, Angle MR, Tayebi N, Verma P, Melosh NA. Mechanical model of vertical nanowire cell penetration. *Nano Lett.* 2013; 13:6002–6008. [PubMed: 24237230]
566. Lin ZC, Xie C, Osakada Y, Cui Y, Cui B. Iridium oxide nanotube electrodes for sensitive and prolonged intracellular measurement of action potentials. *Nat Commun.* 2014; 5:3206. [PubMed: 24487777]
567. Sun Y, Rogers JA. Inorganic semiconductors for flexible electronics. *Adv Mater.* 2007; 19:1897–1916.
568. Yu Z, Graudejus O, Tsay C, Lacour SP, Wagner S, Morrison B III. Monitoring Hippocampus Electrical Activity In Vitro on an Elastically Deformable Microelectrode Array. *J Neurotrauma.* 2009; 26:1135–1145. [PubMed: 19594385]
569. Lacour SP, Benmerah S, Tarte E, FitzGerald J, Serra J, McMahon S, Fawcett J, Graudejus O, Yu Z, Morrison B III. Flexible and stretchable micro-electrodes for in vitro and in vivo neural interfaces. *Med Biol Eng Comput.* 2010; 48:945–954. [PubMed: 20535574]
570. Chen YC, Hsu HL, Lee YT, Su HC, Yen SJ, Chen CH, Hsu WL, Yew TR, Yeh SR, Yao DJ. An Active, Flexible Carbon Nanotube Microelectrode Array for Recording Electroencephalograms. *J Neural Eng.* 2011; 8:034001. [PubMed: 21474876]
571. Timko BP, Cohen-Karni T, Yu G, Qing Q, Tian B, Lieber CM. Electrical Recording from Hearts with Flexible Nanowire Device Arrays. *Nano Lett.* 2009; 9:914–918. [PubMed: 19170614]
572. Dvir T, Timko BP, Kohane DS, Langer R. Nanotechnological strategies for engineering complex tissues. *Nat Nanotechnol.* 2011; 6:13–22. [PubMed: 21151110]
573. Fakhruddin RF, Zamaleeva AI, Minullina RT, Konnova SA, Paunov VN. Cyborg cells: functionalisation of living cells with polymers and nanomaterials. *Chem Soc Rev.* 2012; 41:4189–4206. [PubMed: 22509497]
574. Polikov VS, Tresco PA, Reichert WM. Response of brain tissue to chronically implanted neural electrodes. *J Neurosci Methods.* 2005; 148:1–18. [PubMed: 16198003]
575. Seymour JP, Kipke DR. Neural probe design for reduced tissue encapsulation in CNS. *Biomaterials.* 2007; 28:3594–3607. [PubMed: 17517431]
576. HajjHassan M, Chodavarapu V, Musallam S. NeuroMEMS: neural probe microtechnologies. *Sensors.* 2008; 8:6704–6726.
577. Kozai TDY, Kipke DR. Insertion shuttle with carboxyl terminated self-assembled monolayer coatings for implanting flexible polymer neural probes in the brain. *J Neurosci Methods.* 2009; 184:199–205. [PubMed: 19666051]
578. Biran R, Martin DC, Tresco PA. Neuronal cell loss accompanies the brain tissue response to chronically implanted silicon microelectrode arrays. *Exp Neurol.* 2005; 195:115–126. [PubMed: 16045910]

## Biographies



Anqi Zhang received her bachelor's degree in materials chemistry from Fudan University in China in 2014. She is currently a Ph.D. student under the supervision of Prof. Charles M. Lieber in the Department of Chemistry and Chemical Biology at Harvard University. Her research interests include development of novel nano-bioelectronic tools and their applications in neuron electrophysiology.



Charles M. Lieber is the Mark Hyman Professor of Chemistry and Chair of the Department of Chemistry and Chemical Biology at Harvard University. He received his Ph.D. from Stanford University (1985) and completed postdoctoral studies at the California Institute of Technology (1987). His research is focused on the chemistry and physics of nanoscale materials with a current emphasis on synthesis of novel nanowire structures and the development of novel nanoelectronic platforms for probing and interfacing with biological systems. His work has been recognized by numerous awards, including the Wolf Prize in Chemistry (2012), the Gibbs Medal (2013), and the IEEE Nanotechnology Pioneer Award and his published papers have been cited more than 85,000 times. He is an elected member of the National Academy of Sciences and National Academy of Inventors.

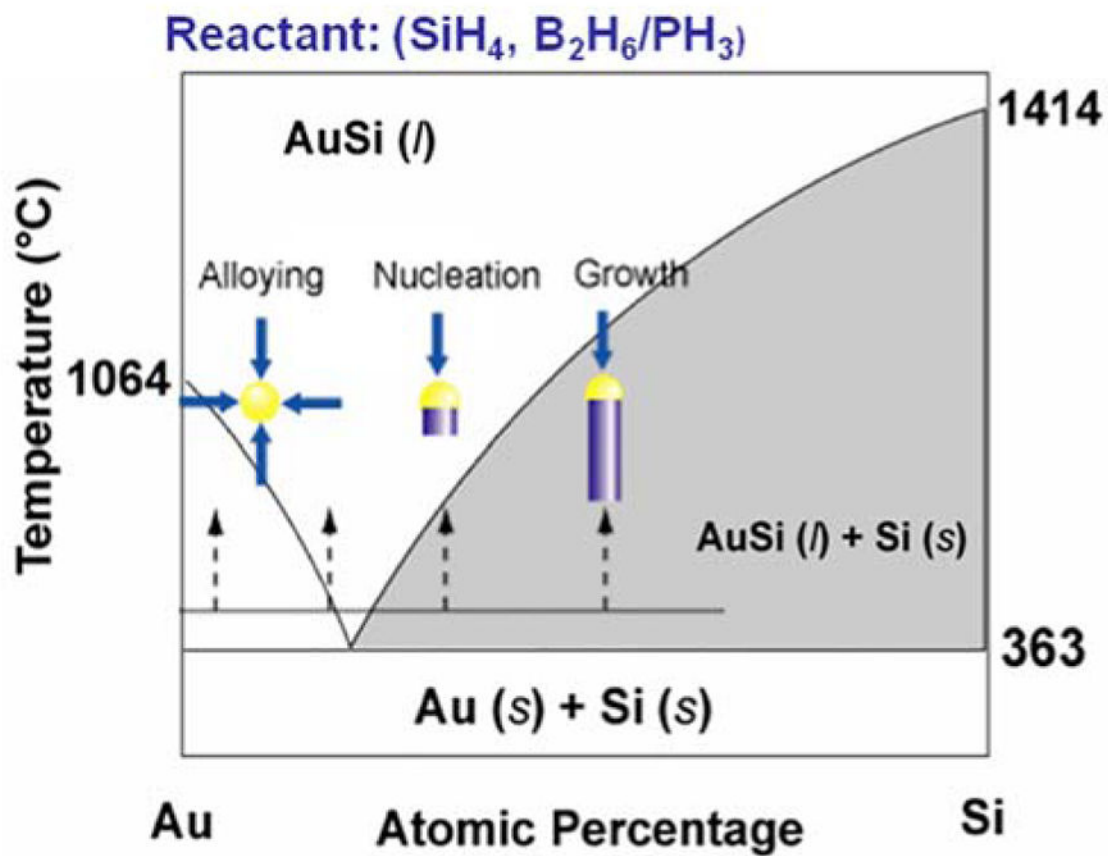


**Figure 1.**  
VLS growth mechanism of SiNWs.

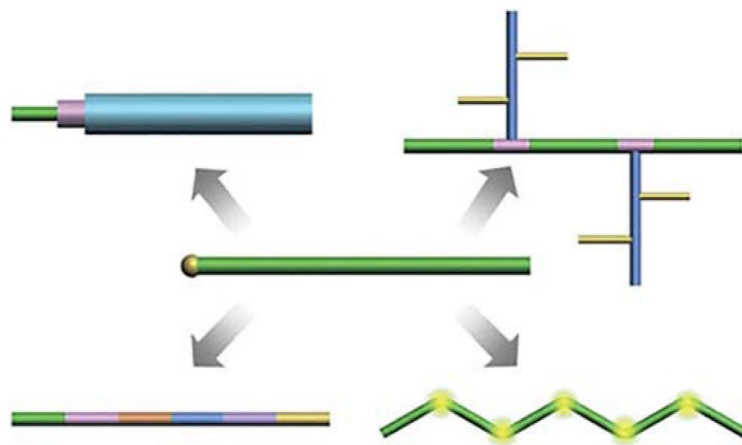


**Figure 2.** Five classes of NW structures available today: basic (center), axial, core/shell, branched and kinked structures, clockwise from lower left. Reprinted with permission from Ref. 6. Copyright 2011 Materials Research Society.

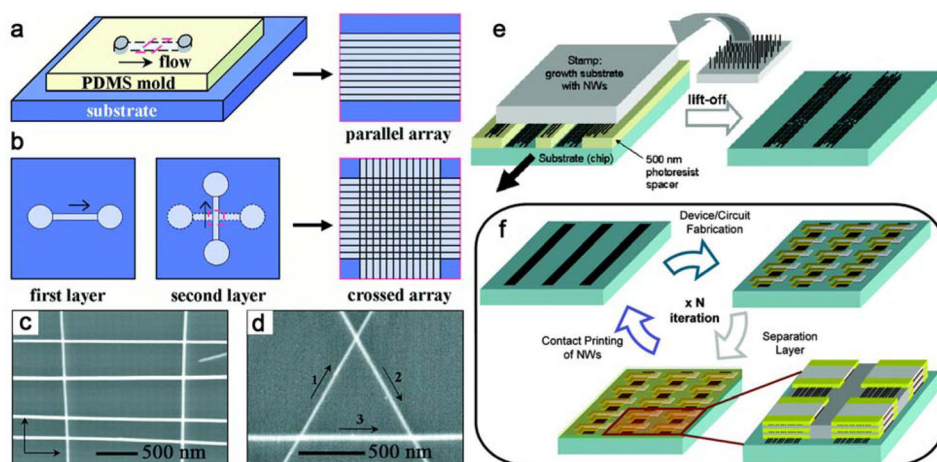


**Figure 3.** (a) Schematic for flow-assisted alignment of parallel NW arrays. (b, c) Schematic and SEM images of crossed NW matrix obtained by changing the flow direction sequentially. (d) A triangle of NWs obtained in a three-step assembly process. Reprinted with permission from Ref. 122. Copyright 2001 American Association for the Advancement of Science. (e) Contact printing of NWs. (f) 3D NW circuit fabricated by multiple contact printing steps. Reprinted with permission from Ref. 160. Copyright 2007 American Chemical Society.

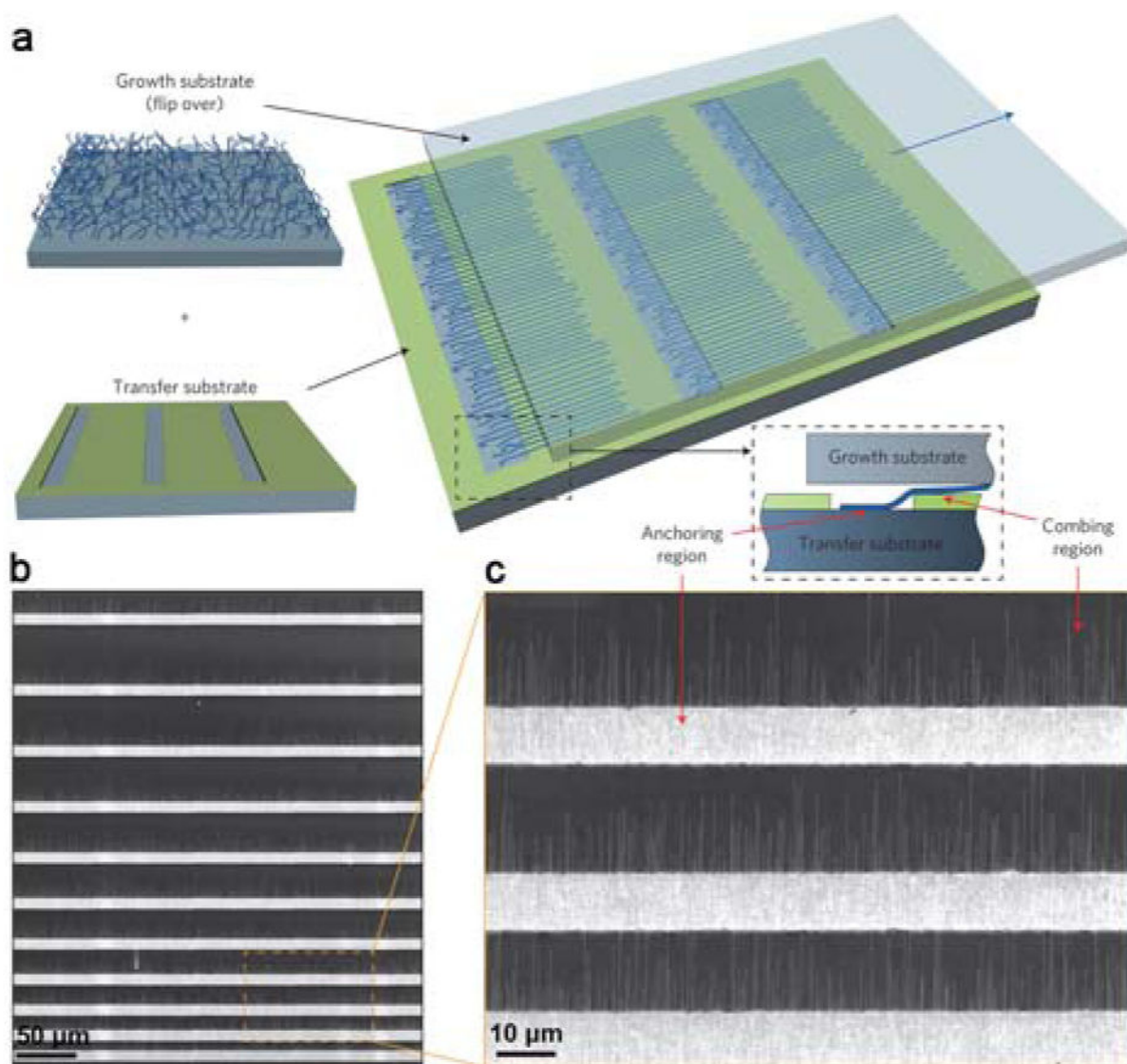


**Figure 4.** (a) Schematics of the nanocombing process. (b, c) SEM images of SiNWs on the combing surface. Reprinted with permission from Ref. 167. Copyright 2013 Nature Publishing Group.

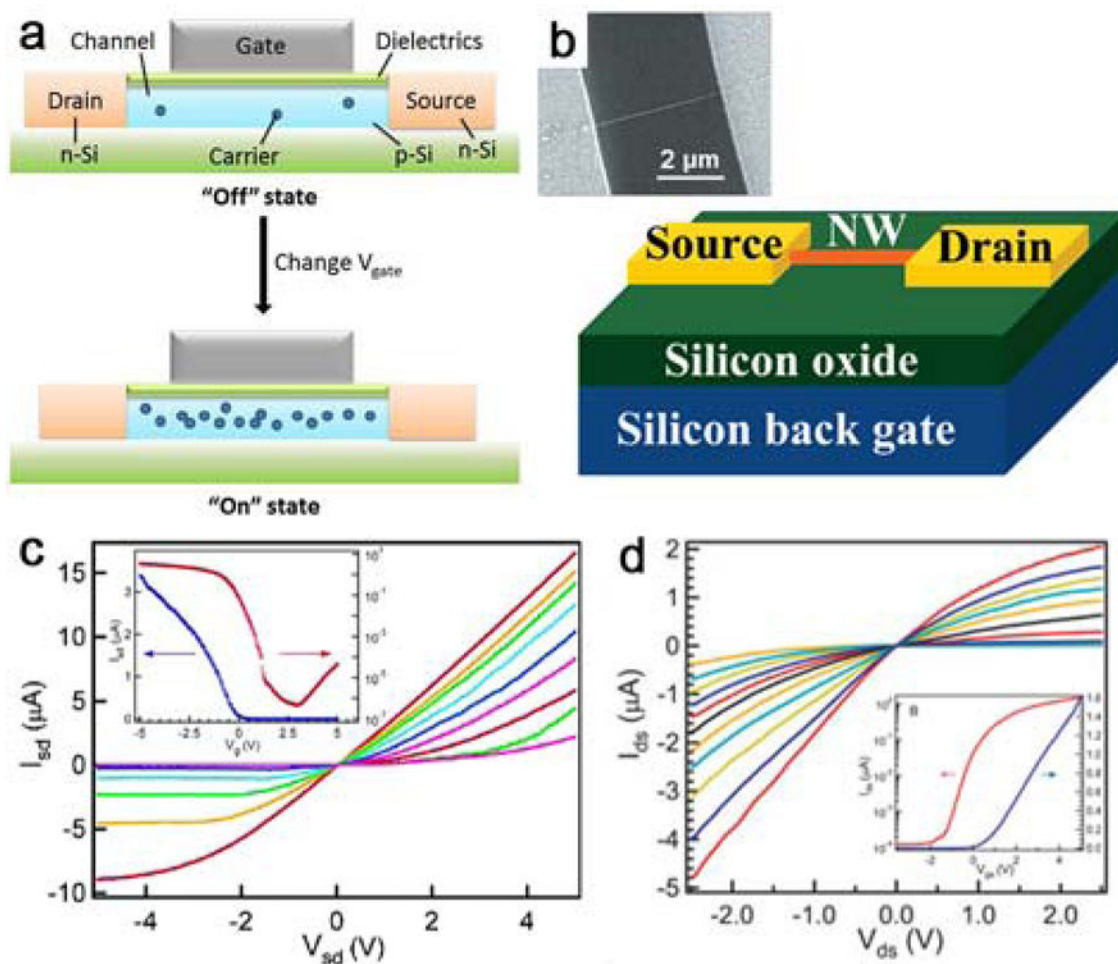


**Figure 5.**

(a) A typical planar FET. The semiconductor substrate (e.g.,  $p$ -Si) is connected to gate (G), source (S) and drain (D) electrodes, and can be switches between the "off" and "on" states by applying the  $V_g$ . (b) Schematic and SEM image of a NW-FET. Reprinted with permission from Ref. 175. Copyright 2002 American Chemical Society. (c, d) Transistor characteristics of  $p$ - and  $n$ -type NWs. Insets show transfer characteristics of the back-gated devices. (c) Reprinted with permission from Ref. 135. Copyright 2004 American Chemical Society. (d) Reprinted with permission from Ref. 179. Copyright 2004 John Wiley & Sons, Inc.

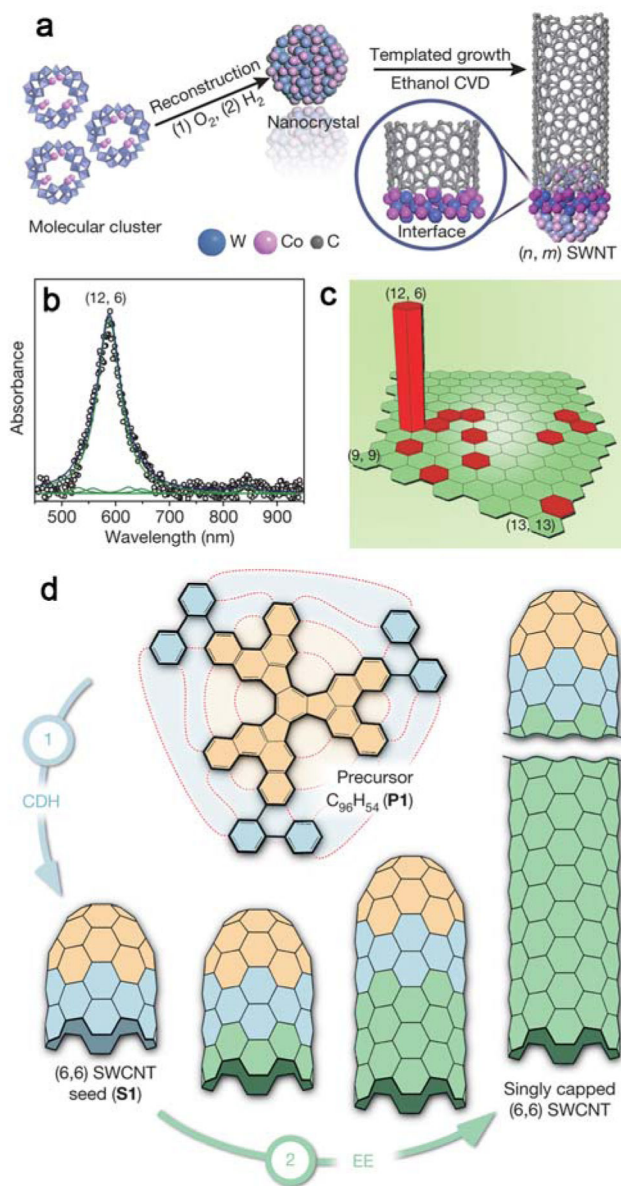


**Figure 6.** Schemes for synthesis of SWNTs with single chirality. (a) Preparation of the W–Co catalyst and the growth of a SWNT. (b) UV–Vis–NIR spectrum from 42 samples. (c) Relative abundances of various chiralities from ~3,300 nanotubes. Reprinted with permission from Ref. 248. Copyright 2014 Nature Publishing Group. (d) Formation of singly capped ultrashort (6,6) seed and subsequent elongation of SWNT. Reprinted with permission from Ref. 253. Copyright 2014 Nature Publishing Group.

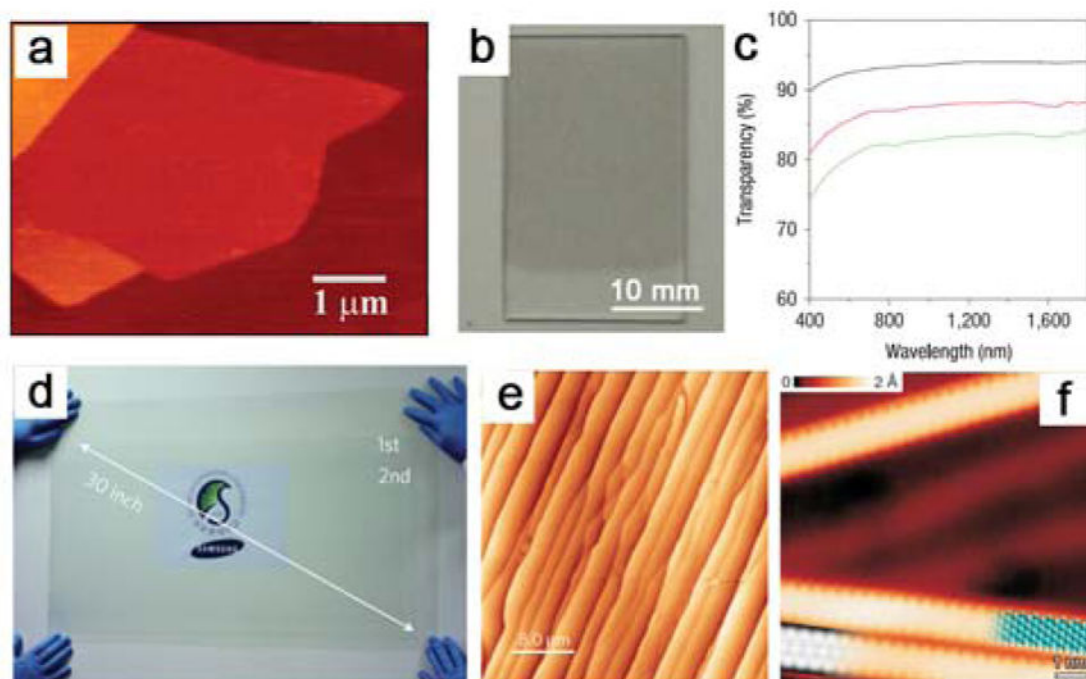


**Figure 7.**

(a) Mechanically exfoliated single-layer graphene sheet. Reprinted with permission from Ref. 318. Copyright 2004 American Association for the Advancement of Science. (b) Liquid-phase exfoliated two-layer graphene LB film on quartz. (c) Transparency spectra of one- (black), two- (red) and three-layer (green) LB films. Reprinted with permission from Ref. 333. Copyright 2008 Nature Publishing Group. (d) Large-area graphene grown by CVD on copper substrate spanning 30 inches diagonally. Reprinted with permission from Ref. 365. Copyright 2010 Nature Publishing Group. (e) AFM image of epitaxial graphene grown on SiC. Reprinted with permission from Ref. 370. Copyright 2009 Nature Publishing Group. (f) STM image of synthesized graphene nanoribbons. Reprinted with permission from Ref. 373. Copyright 2010 Nature Publishing Group.

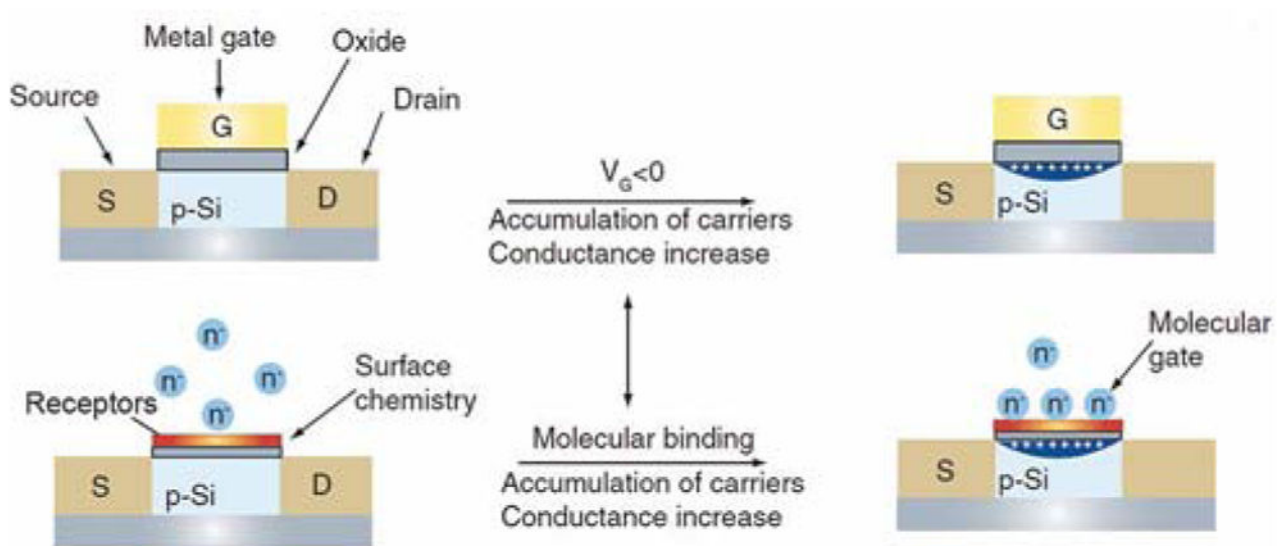


**Figure 8.** Schematic comparison of (top) a standard FET device and (bottom) a SiNW FET sensor. The NW surface is functionalized with a receptor layer to recognize target biomolecules in a solution, which are charged and provide a molecular gating effect on SiNWs. Reprinted with permission from Ref. 397. Copyright 2006 Future Medicine Ltd.

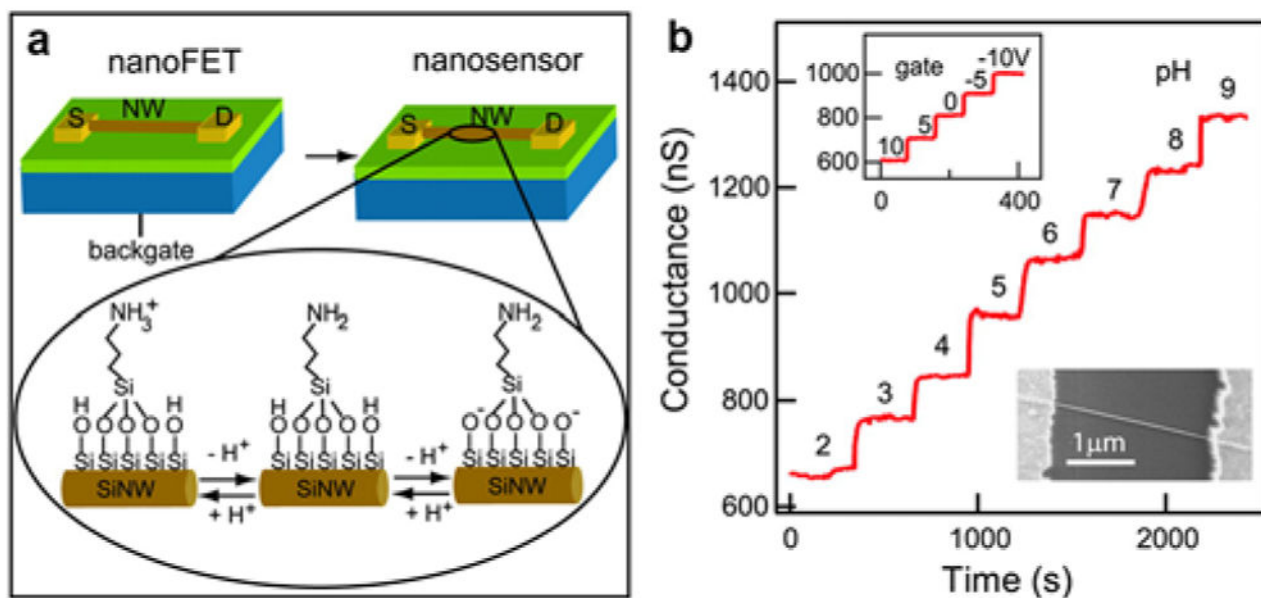


**Figure 9.**

(a) Schematic of a functionalized NW device and the protonation/deprotonation process that changes the surface charge state. (b) Changes in NW conductance versus pH. Reprinted with permission from Ref. 388. Copyright 2001 American Association for the Advancement of Science.

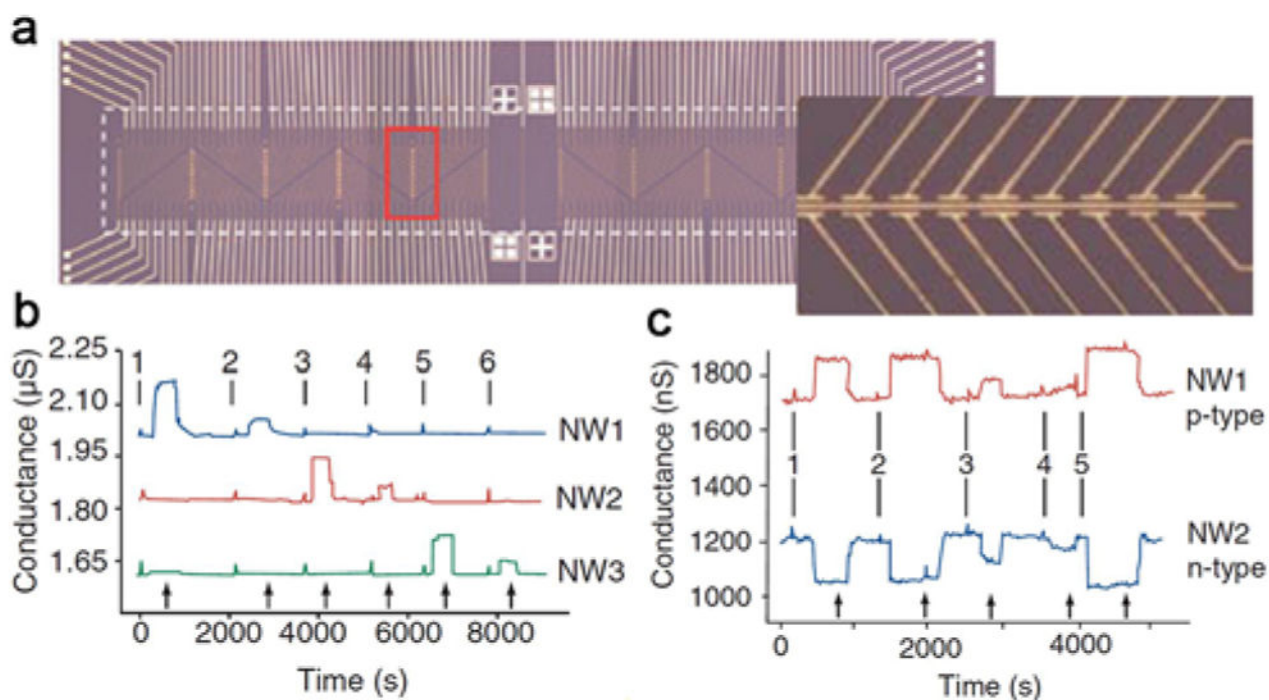


**Figure 10.**

(a) Optical image of a NW array. (b) Sequential detection of PSA, CEA and mucin-1 solutions using three SiNW FET sensors. (c) Complementary sensing of PSA using *p*-type (NW1) and *n*-type (NW2) SiNW FET sensors. Reprinted with permission from Ref. 389. Copyright 2005 Nature Publishing Group.

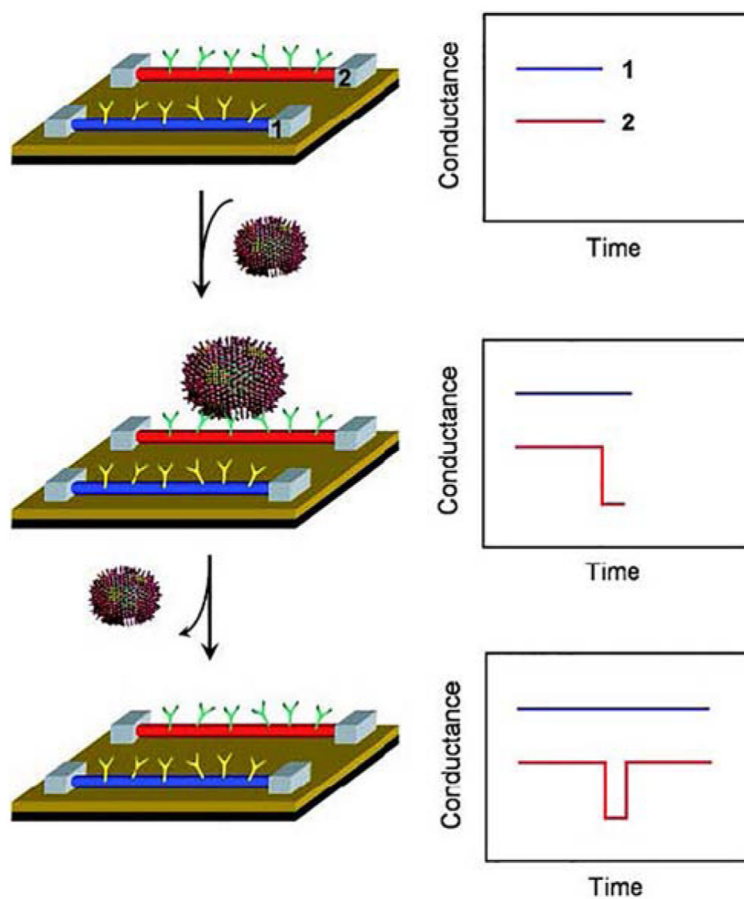


**Figure 11.** Schematic of virus binding/unbinding to a SiNW FET and the corresponding time-dependent conductance change. Reprinted with permission from Ref. 395. Copyright 2004 National Academy of Sciences of the United States of America.

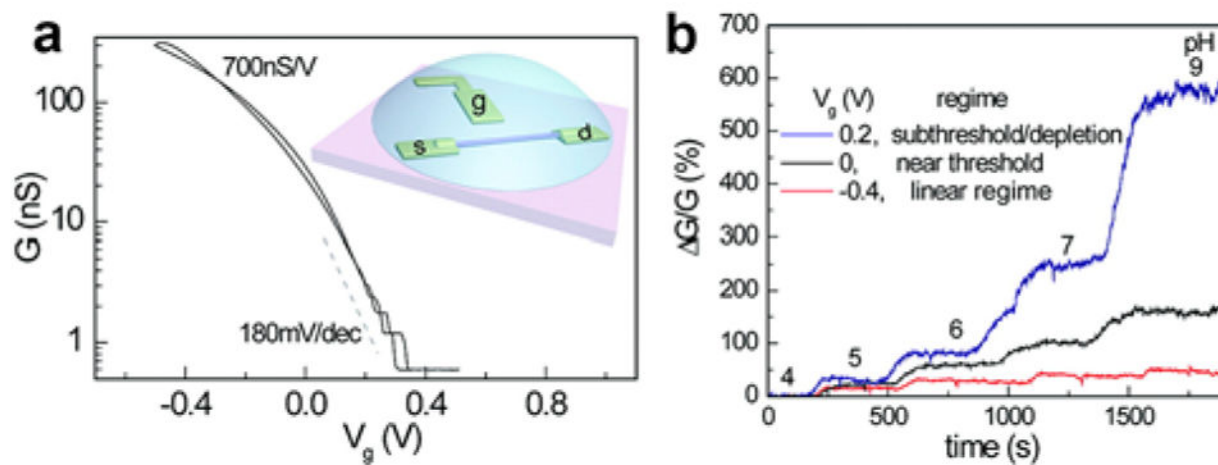


**Figure 12.**

(a) Conductance,  $G$ , vs  $V_g$  for a  $p$ -type SiNW FET. Inset: scheme for electrolyte gating. (b) Real time pH sensing. The device in the subthreshold regime shows much larger  $\Delta G/G$  change versus pH. Reprinted with permission from Ref. 422. Copyright 2010 American Chemical Society.

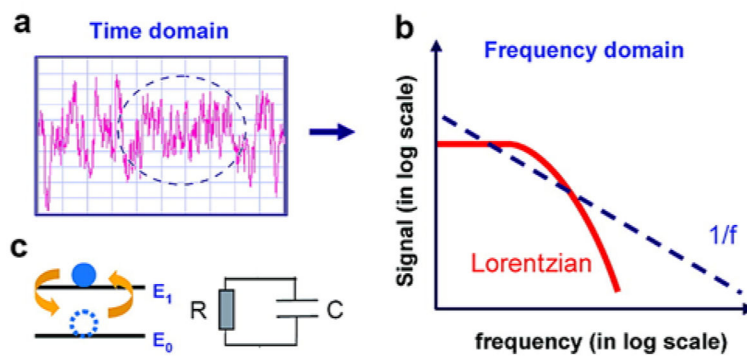


**Figure 13.** (a) Electrical noise in a time-domain measurement. (b) Lorentzian and  $1/f$  functions in the frequency domain. (c) Models of a two-level system (left) and  $RC$  circuit (right). Reprinted with permission from Ref. 429. Copyright 2010 American Chemical Society.

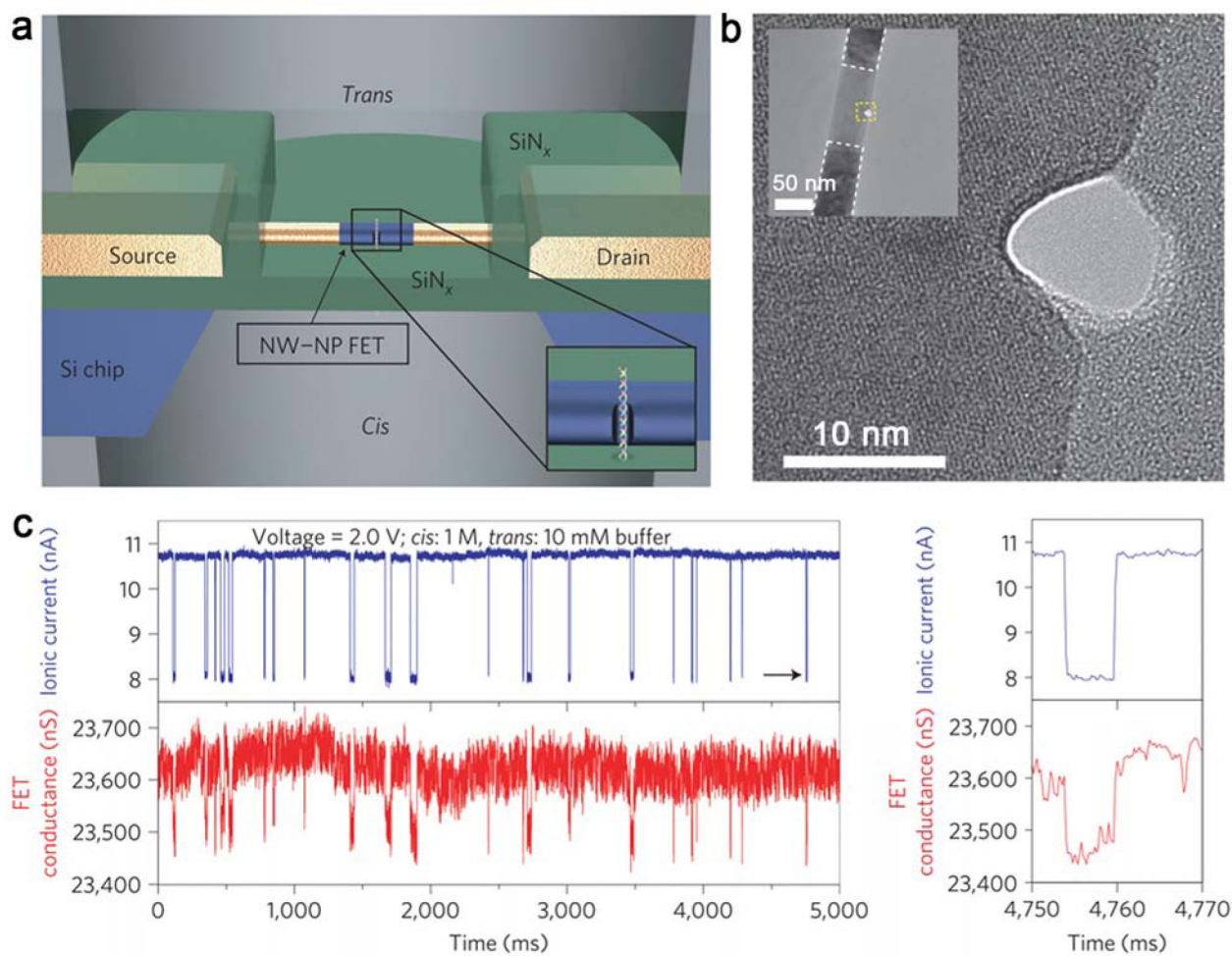


**Figure 14.**

(a, b) Schematic and TEM image of a SiNW-nanopore sensor. (c) Recording of SiNW-nanopore FET conductance and ionic current during DNA translocation. Reprinted with permission from Ref. 432. Copyright 2012 Nature Publishing Group.

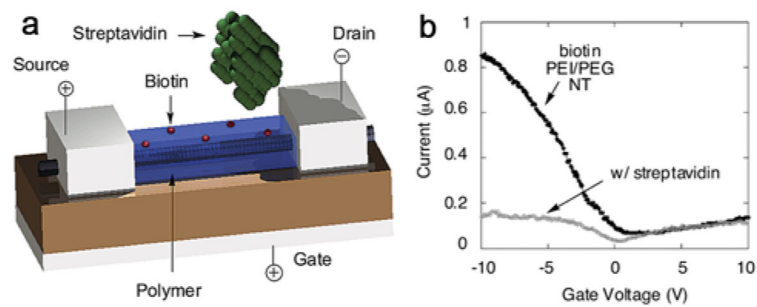


**Figure 15.**

(a) Schematic of a polymer-biotin functionalized SWNT-FET for streptavidin recognition.

(b)  $I-V_g$  relationship before and after adding streptavidin. Reprinted with permission from Ref. 454. Copyright 2003 American Chemical Society.

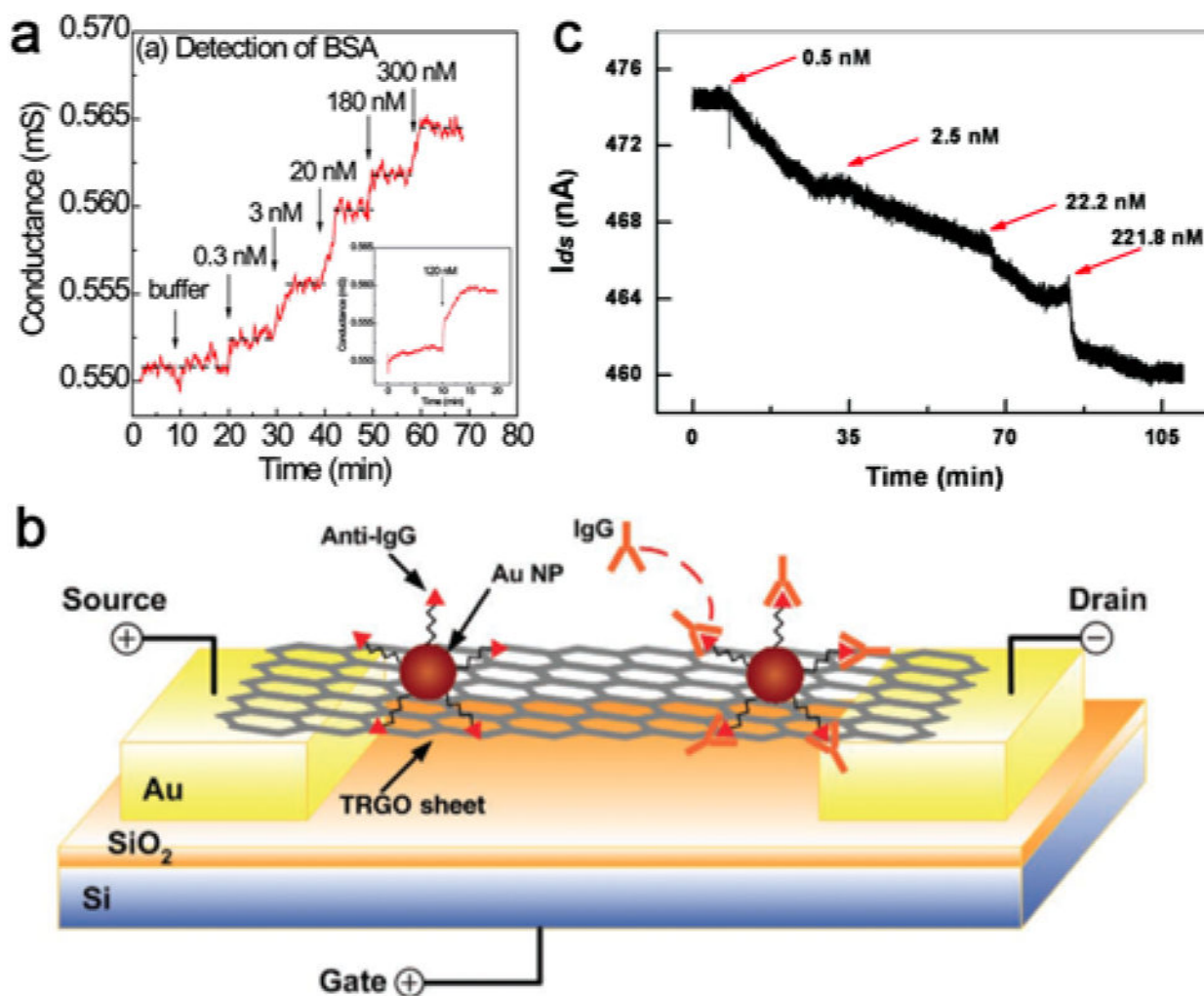


**Figure 16.**

(a) Conductance versus time monitoring various BSA concentrations. Reprinted with permission from Ref. 486. Copyright 2009 American Chemical Society. (b) Schematic of a graphene FET device based on rGO for detection of IgG. IgG antibodies are anchored on AuNPs. Reprinted with permission from Ref. 488. Copyright 2010 John Wiley & Sons, Inc. (c) Real-time detection of fibronectin using the all-rGO sensor. Reprinted with permission from Ref. 489. Copyright 2011 American Chemical Society.

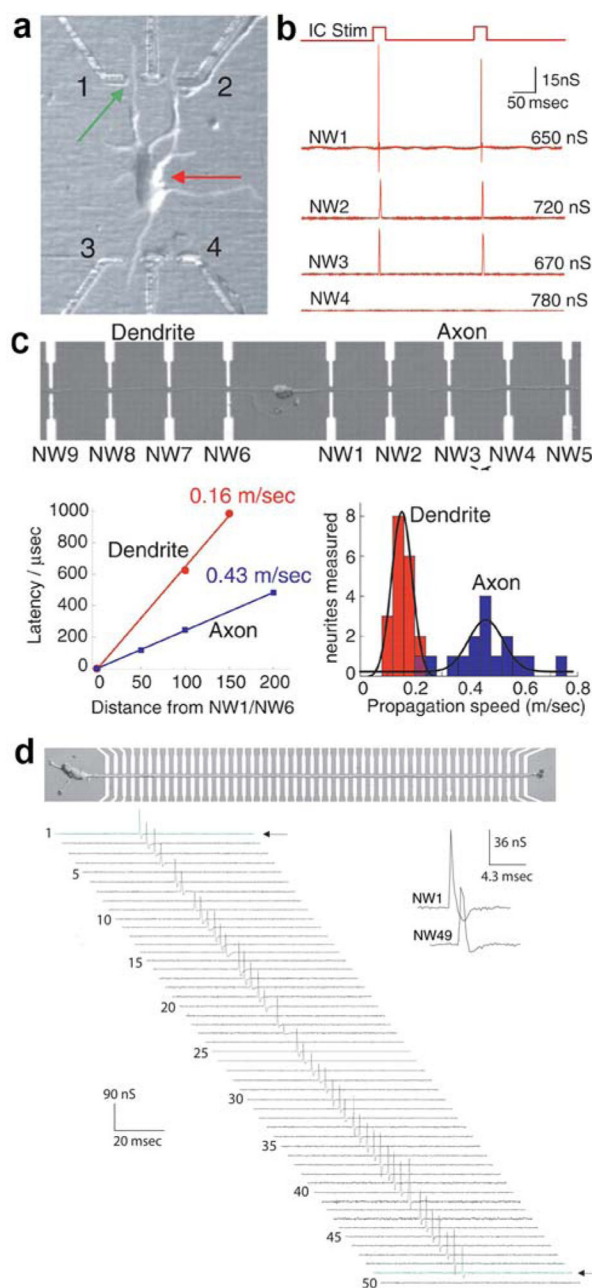


**Figure 17.**

(a) Optical image of a NW-neuron interface. (b) Neuron stimulation and resulting NW electrical responses. NW4 is not in contact with any neurites. (c) Propagation studies using the multi-NW–neurite structures. Top: Optical image of the settings. Bottom: Relation of latency time with distance and histogram of propagation speed. (d) Aligned axon crossing a 50-NW device array and corresponding signal propagation data. Reprinted with permission from Ref. 537. Copyright 2006 American Association for the Advancement of Science.

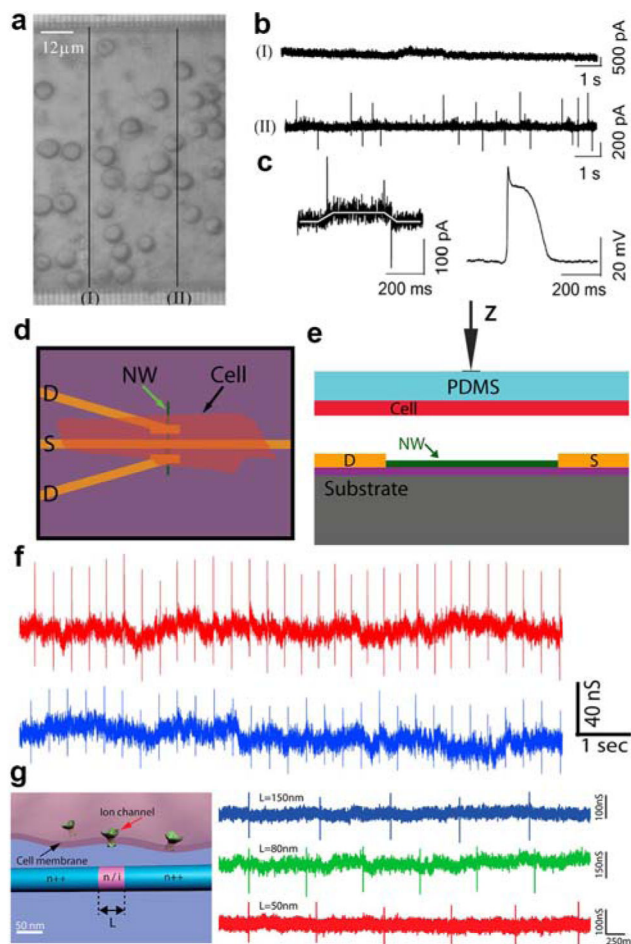


**Figure 18.**

Interfacing SiNW FETs with cardiomyocytes for extracellular recording. (a) Long NWs fabricated by top-down paradigm. Isolated cardiomyocytes are cultured on the NW chip, where the dark lines denoted two NWs, I and II. (b) Currents measured by NW I and II. A series of transient current events are observed for NW II because it is covered by a contracting myocyte. (c) Typical results from NW II (left) compared to the intracellular action potential recorded with a nanopipette (Right). Reprinted with permission from Ref. 538. Copyright 2009 John Wiley & Sons, Inc. (d, e) Schematic of a cardiomyocyte on a NW-FET device and the displacement ( $Z$ ) of the PDMS/cell substrate. (f) Two traces recorded with different  $Z$  values. Reprinted with permission from Ref. 539. Copyright 2009 National Academy of Sciences of the United States of America. (g) Point-like recording using a short-channel NW fabricated by bottom-up paradigm. Left: Schematic of the short-channel FET-cell interface, where the active channel size is comparable to that of a few ion channels. Right: Typical signals of beating cardiomyocytes from devices with channel lengths of 150 (blue), 80 (green) and 50 nm (red). Reprinted with permission from Ref. 84. Copyright 2012 American Chemical Society.

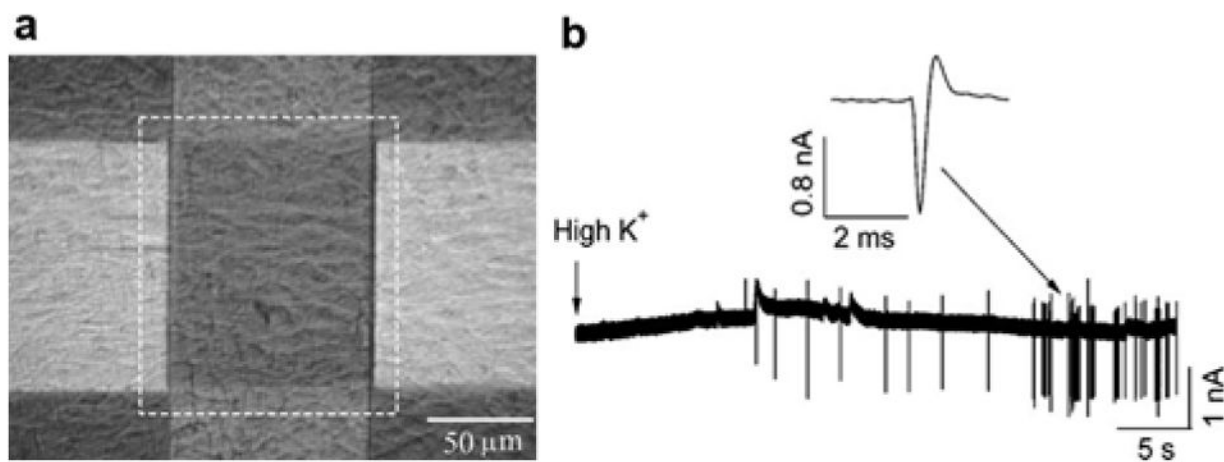


**Figure 19.** SiNW interfaced to aortic smooth muscle cells. (a) Rat aortic smooth muscle cells (A7r5) on the NW chip, in which the dashed square depicts the sensing area. (b) NW recorded current signals induced by membrane depolarizing in high concentration  $K^+$  solution. Reprinted with permission from Ref. 538. Copyright 2009 John Wiley & Sons, Inc.

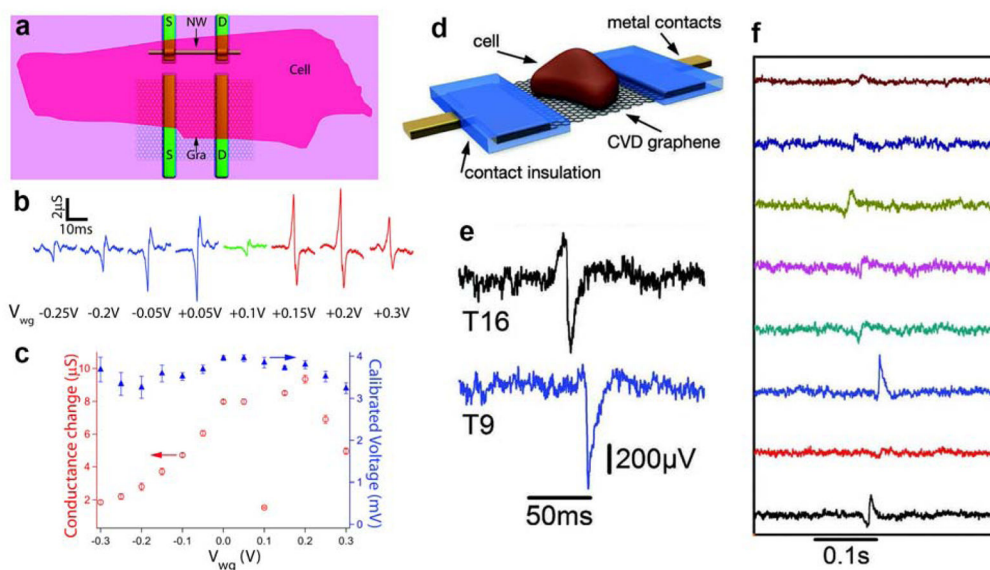


**Figure 20.** Extracellular recording using graphene FETs. (a) Schematic illustrating cardiomyocyte cell interfaced to graphene- and SiNW-FET devices. (b) Recorded extracellular spikes versus gate potential. (c) Summary of the gate potential versus conductance change and calibrated voltage. Reprinted with permission from Ref. 544. Copyright 2010 American Chemical Society. (d) Schematic of a cell on a graphene-FET. (e) Typical two- and one-side peaks observed for different transistors. (f) Simultaneous current recordings from eight transistors in one FET array over hundreds of milliseconds. Reprinted with permission from Ref. 545. Copyright 2011 John Wiley & Sons, Inc.

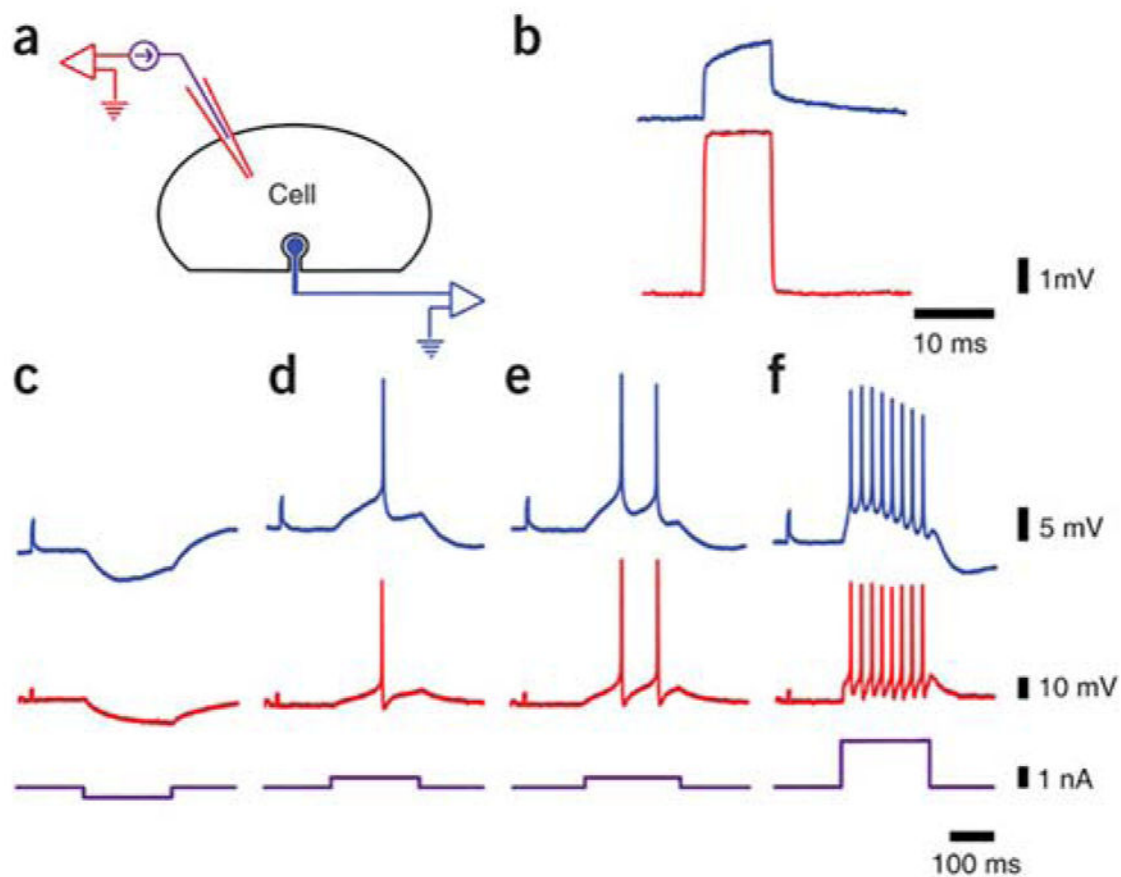


**Figure 21.**

Intracellular-like recordings with FGSEs. (a) Experimental setup with one cell interfaced to a single glass microelectrode (red) and FGSE (blue). (b) Calibrated recording from the intracellular microelectrode (red) and FGSE (blue) for a pulse of 5 mV, 20 ms. (c) A hyperpolarizing current pulse (purple) induced hyperpolarization recorded by the intracellular microelectrode (red) and the FGSE (blue). (d–f) Depolarizing currents generated action potentials with amplitudes of ~50 mV (intracellular microelectrode, red) and ~25 mV (FGSE, blue). Reprinted with permission from Ref. 553. Copyright 2010 Nature Publishing Group.

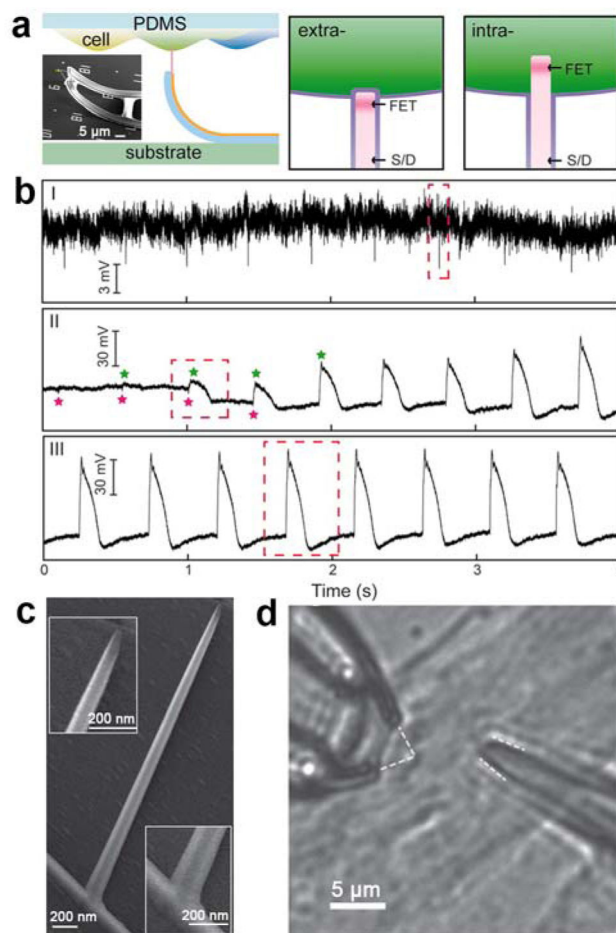


**Figure 22.**

Intracellular recordings with SiNW FETs. (a) Schematics of cellular recording from a cardiomyocyte monolayer on PDMS support (left) and extracellular (middle) and intracellular (right) NW/cell interfaces. Inset is an SEM image of the kinked nanowire device. Purple lines denote the cell membrane and NW lipid coating. (b) Plots corresponding to (i) extracellular, (ii) extracellular to intracellular transition, and (iii) steady-state intracellular recording. Reprinted with permission from Ref. 54. Copyright 2010 American Association for the Advancement of Science. (c) A branched SiO<sub>2</sub> nanotube integrated on top of a SiNW transistor. Reprinted with permission from Ref. 556. Copyright 2012 Nature Publishing Group. (d) Optical image of a kinked NW probe (left) and patch-clamp pipette (right) recording from the same cell. Reprinted with permission from Ref. 558. Copyright 2014 Nature Publishing Group.

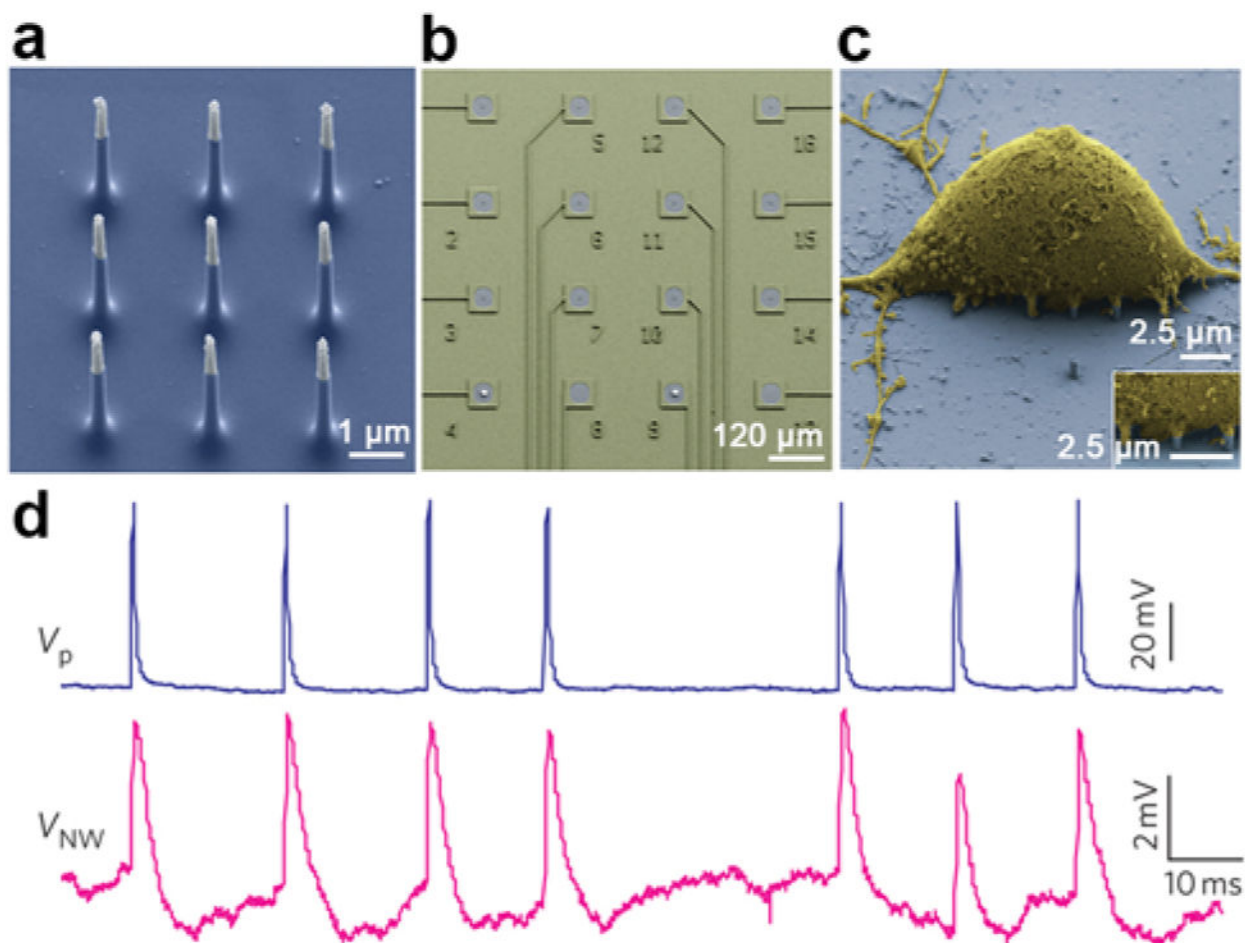


**Figure 23.**

(a) SEM image of a vertical NW electrode array. (b) Stimulation/recording pads for multi-site interrogation of neuronal circuits. (c) A rat cortical cell on the NW array. (d) Action potentials stimulated using a patch pipette (blue) and recorded by the NW array (magenta). Reprinted with permission from Ref. 560. Copyright 2012 Nature Publishing Group.

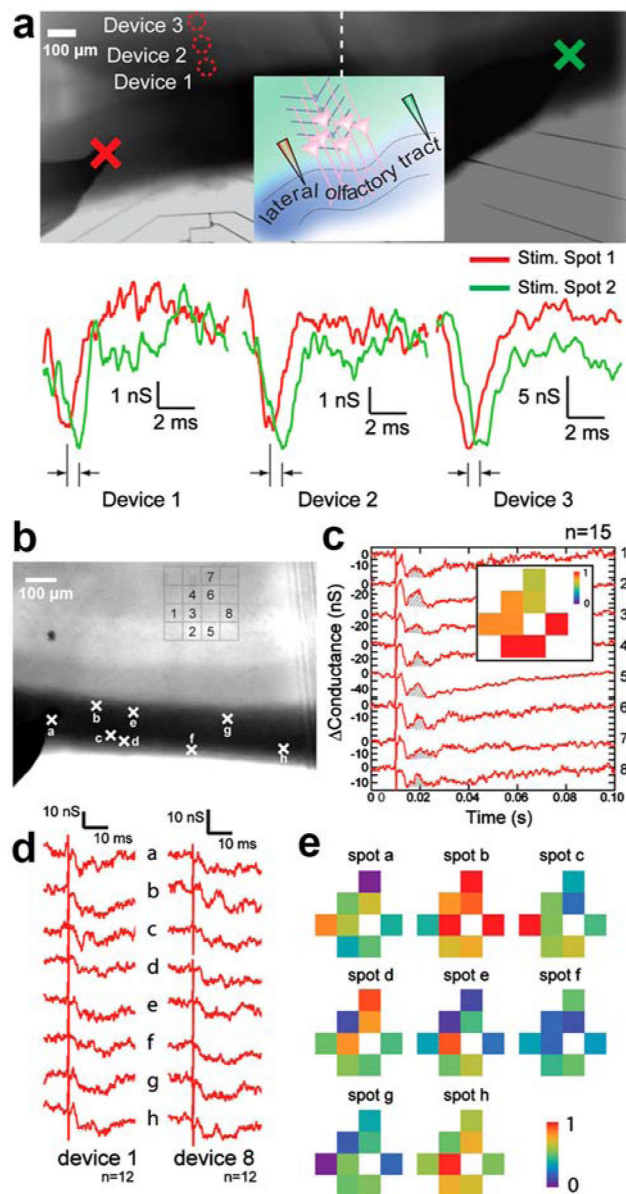


**Figure 24.**

(a) Top: Optical image of an acute brain slice covering a linear array of NW FETs with the array perpendicular to the lateral olfactory tract fiber. *Red* circles denote three devices for recording while the crosses denote the positions of two stimulation electrodes, corresponding to distances *ca.* 400 (red) and 1200  $\mu\text{m}$  (green) from the NW array. Inset is a schematic of the experimental configuration. Bottom: Conductance versus time traces from devices 1–3 following stimulation at red and green crosses, respectively; the curves correspond to averages of 8 recordings. (b) Optical image of an acute slice covering a  $4 \times 4$  NW FET array. Numbers 1–8 denote the device positions while the crosses denote the eight stimulation spots. (c) Averaged signals from 15 recordings following stimulation (200  $\mu\text{s}/400 \mu\text{A}$  pulses). Inset is the normalized map of the signal intensity from the 8 devices deduced from the shaded area in each trace. (d) Representative recordings (averaged from

12) from devices 1 and 8 for stimulations at spots a–h (200  $\mu$ s/100  $\mu$ A pulses). (e) Maps of the relative signal intensity for devices 1–8. Reprinted with permission from Ref. 173. Copyright 2010 National Academy of Sciences of the United States of America.

Author Manuscript

Author Manuscript

Author Manuscript

Author Manuscript

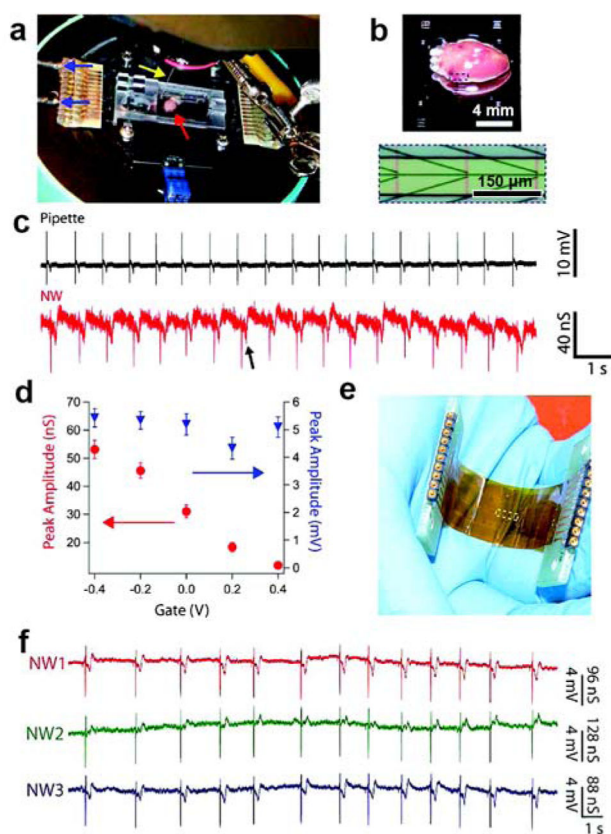


**Figure 25.**

(a) Image of experimental setup for NW FET/heart interface and recording. Arrows denote the positions of heart (red), Ag/AgCl reference electrode (yellow), and source/drain interconnect wires (blue), respectively. (b) Top: Magnified image of heart on the device. Bottom: Zoom-in view of the dotted region in upper image, showing three pairs of NWs with the orientation along the vertical red lines. (c) Parallel recordings made using a glass pipette (black) and NW FET (red). (d) Peak conductance amplitude (red) and calibrated peak voltage amplitude (blue) as a function of gate voltage. (e) Image of a complete chip on a flexible Kapton substrate, where the central dashed box denotes the position of NW FETs. (f) Measured signals at gate of  $-0.2$  V. Reprinted with permission from Ref. 571. Copyright 2009 American Chemical Society.

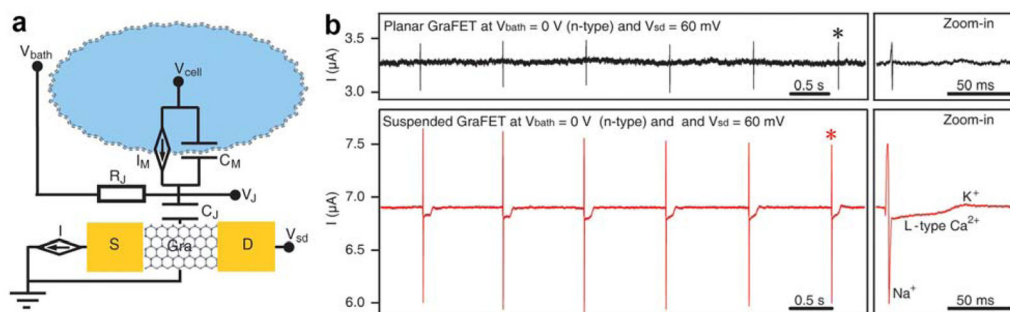


**Figure 26.**

(a) Circuit schematic for graphene-cell interface. (b) Signals from a beating heart recorded by a graphene FET before (black) and after the device was suspended (red). Right panels correspond to zoom-in views denoted by the stars in the left panels. Reprinted with permission from Ref. 546. Copyright 2013 American Chemical Society.

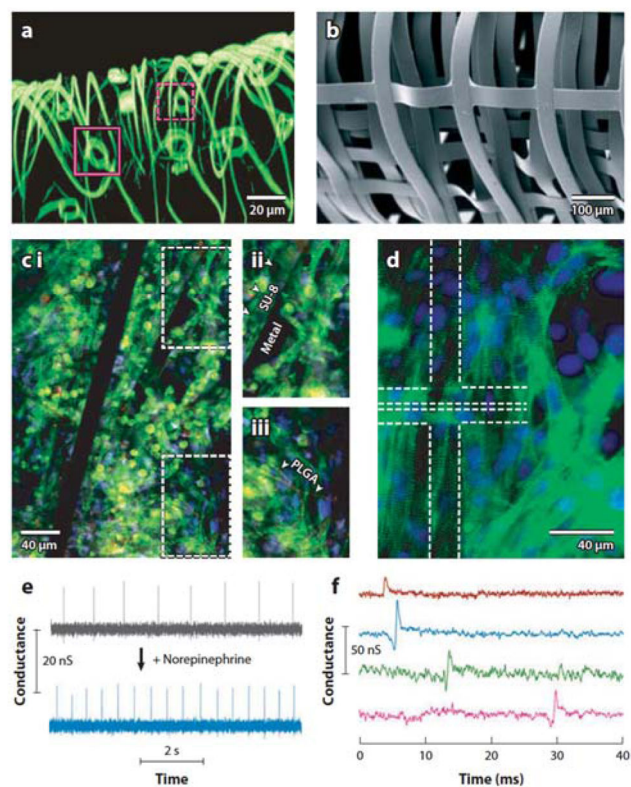


**Figure 27.**

Nanoelectronic scaffolds (nanoES) and synthetic tissues. (a, b) Confocal fluorescence microscopy and SEM images, respectively, of two nanoES. (c) Confocal fluorescence micrographs of a hybrid nanoES/cardiac synthetic tissue patch. (d) Epifluorescence micrograph of the surface from the same hybrid with the posing of a NW FET source-drain electrodes highlighted by the white dashed lines. (e) Time-evolution of periodic conductance spikes recorded by a NW FET device in the nanoES/cardiac hybrid before and after addition of noradrenaline. (f) Multiplex recordings from four NW FETs in a nanoES/cardiac hybrid. Reprinted with permission from Ref. 21. Copyright 2012 Nature Publishing Group.

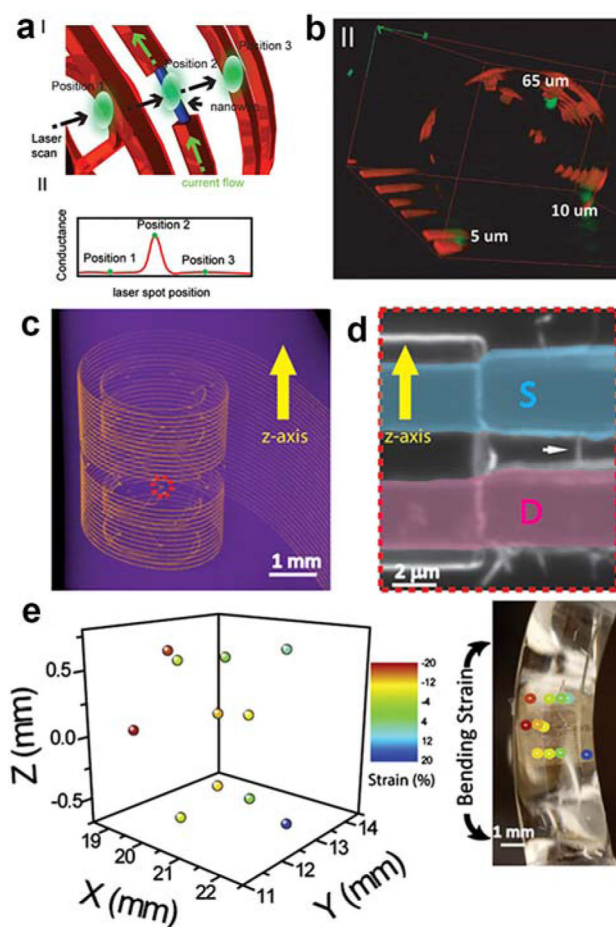


**Figure 28.**

(a) Schematic of 3D macroporous NW structure highlighting simultaneous confocal fluorescence and photocurrent imaging to localize the positions of NW FET devices: blue cylinder, NW; orange-red, polymer mesh network; green dot, laser spot. (b) 3D reconstructed confocal fluorescence/photocurrent microscopy image of a 3D mesh structure. The polymer mesh structure is red-orange and NW FET positions are green. (c) 3D micro-CT image of a strain sensor array embedded in an elastomer, where metal interconnects are visible as yellow-orange lines. (d) Optical image of a typical NW device. The white arrow points to the NW, and source (S) and drain (D) highlighted with blue and pink coloring, respectively. (e) 3D strain field mapped by the NW strain sensors, left; and image of elastomer with embedded macroporous NW network, right. Reprinted with permission from Ref. 22. Copyright 2013 National Academy of Sciences of the United States of America.

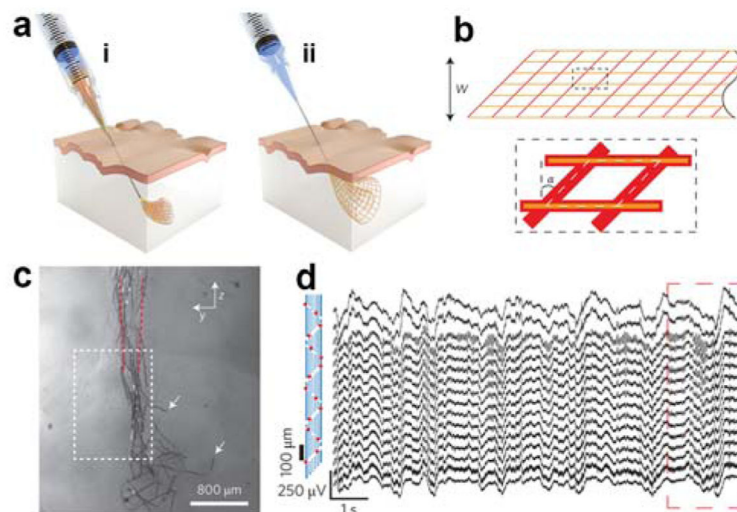


**Figure 29.**

(a) Schematics for injectable electronics. The needle is inserted (i) and retracted (ii) to leave the mesh electronics in the cavity. (b) Schematic of the mesh design, where  $\alpha$  is the angle with respect to a rectangular configuration. (c) Optical image of a longitudinal brain slice taken five weeks after injection into the hippocampus. The mesh is fully extended. (d) 16-channel recording with the mesh electronics following injection into the brain of a live mouse. Reprinted with permission from Ref. 23. Copyright 2015 Nature Publishing Group.